

Cracking the Case of Antarctic Ice Shelf Rifting

A DISSERTATION PRESENTED

BY

STEPHANIE OLINGER

TO

THE DEPARTMENT OF EARTH AND PLANETARY SCIENCES

IN PARTIAL FULFILLMENT OF THE REQUIREMENTS

FOR THE DEGREE OF

DOCTOR OF PHILOSOPHY

IN THE SUBJECT OF

GEOPHYSICS

HARVARD UNIVERSITY

CAMBRIDGE, MASSACHUSETTS

MAY 2023

©2023 – STEPHANIE OLINGER
ALL RIGHTS RESERVED.

Cracking the Case of Antarctic Ice Shelf Rifting

ABSTRACT

The stability of the ice shelves that float at the fringes of Antarctica may be the key to determining the future of the Antarctic Ice Sheet (AIS) and its contribution to sea level rise. Fracture exerts a fundamental control on the geometry of ice shelves and their ability to buttress the AIS. Yet our understanding of rifts, the largest fractures in Earth's ice, is limited by a lack of observations. We explore the diverse range of fracture processes at ice shelf rifts by using seismic recordings, environmental data, remotely-sensed measurements, and mechanical models to characterize the physics of the rifting process. We first examine icequakes generated by fracture at a rift in the Ross Ice Shelf and relate their timing to stresses imposed by changing air temperature and ocean tides. We then shift our focus to the rapidly-accelerating Pine Island Glacier. We characterize dynamic flexure generated by fracture in the shear margin and at a gradually-propagating rift, and we find that rift propagation is related to changes in ocean forcing and ice dynamics. Using seismic recordings and synthetic aperture radar, we observe the fastest recorded episode of rift propagation, and we use a coupled model of the fracture mechanics and hydrodynamics active during rifting to precisely explain the observed rate of propagation. Finally, we present the results of an ongoing project that uses distributed acoustic sensing to characterize the dynamics of a fast-flowing glacier in West Greenland. The work in this thesis provides a new level of detail in our observation of ice shelf rifts and represents a significant step towards better understanding their behavior and influence.

Contents

o	INTRODUCTION	i
1	TIDAL AND THERMAL STRESSES DRIVE SEISMICITY ALONG A MAJOR ROSS ICE SHELF RIFT	10
1.1	Data	11
1.2	Methods	12
1.3	Characteristics and Locations of Rift Seismicity	16
1.4	Ocean Tides Controls Diurnal Patterns in Seismicity	19
1.5	Temperature Controls Multi-day and Seasonal Patterns in Seismicity	21
1.6	Rift Seismicity is Insensitive to Ocean Swell and Infragravity Waves	23
1.7	Conclusions	25
2	HOLISTIC ANALYSIS OF ICE SHELF FRACTURE AT PINE ISLAND GLACIER ICE SHELF	27
2.1	Analysis of Satellite Imagery and Positioning	29
2.2	Analysis of Seismograms	32
2.3	Relationships Between Icequakes and Ice Shelf Behavior	39
2.4	Flexural Gravity Wave Modeling	43
2.5	Discussion of Icequake Source Physics	50
2.6	Conclusions	53
3	OCEAN COUPLING CONTROLS THE FASTEST OBSERVED ICE SHELF RIFT PROPAGATION EVENT	54
3.1	Near-rift observations	55
3.2	Model of Flexural Gravity Waves on a Viscoelastic Ice Shelf	63
3.3	Model of Ocean Coupled Rift Propagation	69
3.4	Results of Mechanical Modeling	79
3.5	Discussion	82
4	NEW FRONTIERS IN GLACIER BOREHOLE DISTRIBUTED ACOUSTIC SENSING	84
4.1	Observations	88
4.2	Ice Structure and Dynamics using Ambient Noise Cross Correlation	93

4.3	Conclusions	101
5	CONCLUSION	102
	APPENDIX A SENSITIVITY OF ICEQUAKE DECONVOLUTION	105
	APPENDIX B SENSITIVITY OF OCEAN COUPLED FRACTURE	110
	REFERENCES	126

Listing of figures

1.1	Study site and icequake locations. (a) Locations of rift WR ₄ , the seismograph array, and weather station Gill on the Ross Ice Shelf. Data from stations DR ₀₇ and DR ₀₆ (not shown) was additionally used to locate icequakes. (b) Locations of 2500 icequakes at WR ₄ . East of about 180°, icequake locations fall along central axis of rift; west of 180°, icequake locations fall within en echelon features containing rift-filling melange. Arrows indicate suture zone fabric.	16
1.2	Rift imagery. (a) Imagery of rift's eastern end showing en echelon features in rift filling melange. To offer a clear view of rift morphology, icequake locations are not plotted. (b) Imagery of entire rift showing widening at its center. Arrows indicate suture zone fabric.	17
1.3	Icequake waveforms. HHE (horizontal east-west) component seismogram, HHN (horizontal north-south) component seismogram, and HHZ (vertical) component seismogram filtered on 1-3 Hz for icequake on 2015:011:21:59:40.	18
1.4	Seasonal changes in noise floor. (a) Determination of 0.01 μm summer detection threshold. (b) Histogram of all events with average amplitude (DR ₁₃ and DR ₁₄) greater than 0.01 μm . Despite changes in event detectability due to retreating sea ice, seasonal patterns in event timing still correlate well with temperature.	18
1.5	Tidal slope and rift seismicity. (a) Histogram of event timing as a function of tidal phase plotted with ocean surface slope (blue lines) for each tidal cycle during the duration of the deployment. (b) Modeled tidal heights at 81.75°S, -175°W, the center of the ice shelf (top), and in map view across the RIS (bottom) demonstrating the ocean surface slope relationships shown in (a). Red dots in the top figures identify the timing of the ice shelf height maps. Tidal heights were obtained using the CATS2008 tidal model ⁵¹	20

1.6	<p>Ocean swell, infragravity waves, temperature and rift seismicity. (a) Surface temperatures from AWS station Gill (blue) plotted with the histogram of rift seismicity (orange) as a function of time during the deployment. (b) Spectrogram showing swell and infragravity wave band power. Black bars indicate data gaps. (c) Ocean swell power (purple line) in the frequency band 0.03 - 0.15 Hz plotted with the histogram of rift seismicity. (d) Infragravity wave power (green line) in the frequency band 0.015 - 0.03 Hz, plotted with the histogram of rift seismicity. Spectral analysis used long period north-south component data from station DR10. The Illapel, Chile tsunami arrival is indicated in pink on each panel of the figure. The seasonal trend in seismicity corresponds to seasonal temperature variation, and wintertime swarms coincide with periods of extreme cold and not with swell or infragravity waves.</p>	22
1.7	<p>Density plot of number of events as a function of tidal phase and temperature. Temperature data is from weather station Gill (Figure 1.1). Peak levels of seismicity are observed when temperature is low and when the shelf is most highly sloped downward toward the ice front during falling tide.</p>	24
2.1	<p>TerraSAR-X images showing an overview of fracture development at PIG from 2012 to 2014. Large arrow in panels c. and d. show sense of motion of the iceberg. See text for full discussion.</p>	31
2.2	<p>Back-azimuthal histogram showing locations of cataloged icequake. Rift-tip event back-azimuths are plotted as orange rays. Rift/margin event back-azimuths are plotted as green rays. Shear-margin event back-azimuths are plotted as purple rays. Likely source regions are shown by colored polygons. PIG array seismic and GPS stations are plotted as black triangles. Approximate grounding line position is shown by the red dashed line¹⁰³. Background LANDSAT imagery is from October 2013 (courtesy of the United States Geological Survey).</p>	40
2.3	<p>Timing and waveforms of cataloged icequake. (a) GPS-derived ice velocity is shown by the black line, and average seismic noise is shown by blue bars. Noise is highest in the Antarctic summer, when minimal sea ice is present to attenuate ocean-generated noise, reducing detectability in January, February, and March. (b) Rift-tip events. Weekly timeseries of rift tip event times is shown by orange bars. Daily vertical (HHZ) waveform stacks of detected rift tip events are plotted beneath. Overall rift-tip event stack is shown to the right. (c) Same as (b) for rift/margin events, color-coded in green. (d) Same as (b) for shear-margin events, color-coded in purple.</p>	41

2.4	<p>Green’s functions and source time functions for rift tip events. (a) Theoretical Green’s function for a point moment source located at a distance of 25 km, which is approximately the distance from PIG seismic array to the rift tip. (b) Source time function retrieved by deconvolving the point moment Green’s function from the stack of rift tip vertical displacement waveforms. (c) Theoretical Green’s function for a point load source located at a distance of 25 km. (d) Source time function retrieved by deconvolving the point load Green’s function from the stack of rift tip vertical displacement waveforms. (e) Stack of rift tip vertical displacement waveforms obtained by aligning waveforms to a master event and taking the mean waveform on the frequency band 0.01-1 Hz.</p>	50
2.5	<p>Green’s functions and source time functions for rift/margin events. (a) Theoretical Green’s function for a bending moment source located at a distance of 30 km, which is approximately the distance from PIG seismic array to the rift/margin area. (b) Source time function retrieved by deconvolving the moment Green’s function from the stack of rift/margin vertical displacement waveforms. (c) Theoretical Green’s function for a point load source located at a distance of 30 km, which is approximately the distance from PIG seismic array to the rift/margin area. (d) Source time function retrieved by deconvolving the point load Green’s function from the stack of rift/margin vertical displacement waveforms. (e) Stack of rift/margin vertical displacement waveforms obtained by aligning waveforms to a master event and taking the mean waveform on the frequency band 0.01-1 Hz.</p>	51
2.6	<p>Green’s functions and source time functions for shear margin events. (a) Theoretical Green’s function for a bending moment source located at a distance of 17.5 km, which is approximately the distance from PIG seismic array to the northeast shear margin near Evans Knoll. (b) Source time function retrieved by deconvolving the moment Green’s function from the stack of shear margin vertical displacement waveforms. (c) Theoretical Green’s function for a point load source located at a distance of 17.5 km, which is approximately the distance from PIG seismic array to the shear margin. (d) Source time function retrieved by deconvolving the point load Green’s function from the stack of shear margin vertical displacement waveforms. (e) Stack of shear margin vertical displacement waveforms obtained by aligning waveforms to a master event and taking the mean waveform on the frequency band 0.01-1 Hz.</p>	51

- 3.1 **Comparison of May 9, 2012 rift event and November 17, 2013 Mw 7.7 Scotia Sea earthquake.** All displayed data are vertical velocity seismograms recorded by station PIG2, and all displayed spectra were computed using these data. **(a)** Comparison of power spectral density (PSD) of May 9 rift event, Scotia Sea earthquake, and noise. PSD of May 9 rift event is shown in orange, and PSD of one hour of noise prior to the May 9 rift event is shown in light orange. PSD of Scotia Sea earthquake is shown in purple, and PSD of one hour of noise prior to the Scotia sea event is shown in light purple. The May 9 event had a dominant period of 600.0 s, while the Scotia Sea earthquake had a dominant period of 17.1 s. **(b).** Seismic recording of May 9 rift event. The rift signal is clearly dispersive, and characteristic 600.0 s period waves are clearly visible after T18:30. **(c).** Seismic recording of Scotia Sea earthquake. Scotia Sea signal is not clearly dispersive, and does not contain significant power at periods below 100 s. 59
- 3.2 **TSX and seismic data surrounding 10.5 km of rift propagation.** All seismic data are vertical velocity seismograms recorded by station PIG2. **(a)** TSX data from May 8, 2012 04:04 (t_1) before propagation of R2012. Black triangles show on-ice seismic stations. Inset shows location of PIG within Antarctica. **(b)** TSX data from May 11, 2012 03:13 (t_2) after propagation of R2012. Contours show the logarithm of root mean squared error (RMSE) in arrival time residuals from a gridsearch of possible locations of the May 9 signal computed using on-ice seismic stations and regionally-deployed seismic stations (not shown). Arrow denoted by θ shows backazimuth computed using the polarization of seismic waves recorded by on-ice seismic stations. **(c)** Seismogram spanning the time window between TSX data. Rift event signal is highlighted in pink. **(d)** Seismogram of rift event filtered between 0.001 Hz and 1 Hz. In this frequency band, signal is dominated by flexural gravity (FG) waves. Resonance of ice shelf modes results in an event duration on the order of hours. **(e)** Seismogram of rift event filtered above 1 Hz. In this frequency band, signal is dominated by P waves and surface waves. The abrupt decay of the rift event signal 302 s after the onset of the event indicates the conclusion of rift propagation. 62

3.3	<p>Model of fluid-coupled fracture. In all panels, the black curves show model results for a rift coupled to hydrodynamics, and the orange curves show model results for a rift uncoupled to hydrodynamics. (a) Illustration of the proposed mechanism for rift propagation at a small fraction of the Rayleigh wave speed (c_r). As the rift propagates, the increase in total volume within the rift drives the fluid to flow into the rift from below. (b) Modeled perturbation from hydrostatic water level induced by rift propagation. In the coupled case, the water level initially decreases because fluid cannot flow into the rift fast enough to maintain the hydrostatic water level. Once the rift propagation concludes, fluid flow overshoots the hydrostatic water level and oscillates at the sloshing period T_{slosh}. In the uncoupled case, the water level in the rift does not change. (c) Modeled rift propagation rate through time. In the coupled case, propagation occurs at a small fraction of c_r, because the decreasing water line reduces the water pressure acting to open the rift. In the uncoupled case, propagation approaches c_r rapidly and remains constant once c_r is reached. (d) Modeled rift length through time for 500 s of rift propagation. (e) Modeled rift length through time for 302 s of rift propagation. In the coupled case, the rift length increases by 10.5 km at an average rate of 34.8 m/s, corresponding closely to the observed propagation rate of R2012.</p>	81
4.1	<p>Study site and distributed acoustic sensing (DAS) deployment. (a) Surface of Store Glacier and the location of the borehole used to deploy fiber optic cable for DAS. Note the surface water flow that drains through a moulin near the borehole. Red dots show active source shot locations in a previous study¹³⁹. The inset shows the location of Store Glacier within West Greenland. (b) On-site interrogator and data analysis station. (c) Machinery used to drill borehole BH19c and carry out active source seismic analysis in Booth et al., 2020¹³⁹. (d) Geometry of fiber optic cable, including lateral distance on the surface, vertical extent, and channel spacing. Figure used with permission</p>	87
4.2	<p>RMS of noise recorded by DAS deployment as a function of channel depth. The RMS was computed for each 30 s time window in the dataset at each channel along the cable on the frequency band 1-100 Hz. The orange dotted line shows the inferred location of the borehole freezing front. The blue dotted circles show periods of elevated near-surface noise generated by surface water flow and percolation due to diurnal surface melt.</p>	89

4.3	Correlation of surface noise, basal water pressure, and surface ice flow velocity. Red dotted line shows basal water pressure recorded at a nearby borehole (BH19e). The gold line shows diurnal fluctuation in ice flow velocity. Note the correspondence in phase between basal water pressure and ice flow velocity. Absolute flow velocities are not shown for simplicity. Purple, crimson, and orange lines show the average noise RMS recorded by channels in the depth bins in the legend. Peak amplitudes in seismic noise are recorded each day in the mid-afternoon when the diurnal surface melt is highest. Maximum basal water pressure and fastest flow velocities are recorded about 4 hours after each maximum in seismic noise. Note that surface flow velocity and basal pressure at BH19e were not recorded during the DAS deployment. The data displayed here, recorded 24 days later, are properly aligned in reference to time-of-day and are emblematic of typical diurnal patterns in basal water pressure and flow velocity.	92
4.4	Spectrogram of data recorded by basal DAS channels. The spectrogram was computed using the average trace of data recorded between 1025 m and 1035 m depth. Note the presence of gliding lines between 0.01 and 0.5 Hz and elevated signal power below 0.01 Hz.	93
4.5	Schematic of cross-correlation function stacking algorithm. To improve the signal-to-noise ratio, correlation functions computed using corresponding pairs of stations from each portion of the cable were summed. Leg 1 correlation functions were computed using each pair of stations on the downgoing portion of the cable. Leg 2 correlation functions were computed using each pair of stations on the upgoing portion of the cable. Leg 3 and leg 4 correlation functions were computed using pairs of stations from the downgoing and upgoing portions of the cable. The overall stack is retrieved by summing the corresponding correlation functions from each leg.	97
4.6	Stacked correlation functions for a virtual source near the glacier surface. Displayed correlation functions computed in reference to a channel at the top of the borehole and filtered between 1 and 50 Hz. P and S wave are shown by the purple and orange lines respectively. Anomalous slow phase, inferred to be a borehole tube wave, is shown in blue. The dotted line shows the depth of the transition between Holocene and Wisconsin ice.	98
4.7	Stacked correlation functions for virtual sources at depth. (a) Same as Figure 4.6 but displayed correlation functions were computed in reference to channel at 300 m depth. (b) Correlation functions computed in reference to channel at 600 m depth. (c) Correlation functions computed in reference to a channel at 800 m depth. (d) Correlation functions computed in reference to channel at glacier base (1043 m depth). Note the conjugate symmetry between correlation functions computed in reference to surface and basal channels.	100

A.1	Sensitivity of rift tip source time function deconvolution to modeled ice thickness. (a) Sensitivity of point moment source time functions. (b) Sensitivity of point load source time functions. Modeled beam thicknesses are shown in the legend. Source time functions generally have larger amplitude and longer duration for thicker beams, because larger forcing is required to induce a given displacement for a more rigid beam. Flexural rigidity, the parameter that governs flexure, is a function of thickness. . . .	106
A.2	Sensitivity of rift/margin source time function deconvolution to modeled ice thickness. (a) Sensitivity of point moment source time functions. (b) Sensitivity of point load source time functions. Modeled beam thicknesses are shown in the legend. Source time functions generally have larger amplitude and longer duration for thicker beams, because larger forcing is required to induce a given displacement for a more rigid beam. Flexural rigidity, the parameter that governs flexure, is a function of thickness. . . .	107
A.3	Sensitivity of margin source time function deconvolution to modeled ice thickness. (a) Sensitivity of point moment source time functions. (b) Sensitivity of point load source time functions. Modeled beam thicknesses are shown in the legend. Source time functions generally have larger amplitude and longer duration for thicker beams, because larger forcing is required to induce a given displacement for a more rigid beam. Flexural rigidity, the parameter that governs flexure, is a function of thickness. . . .	108
A.4	Modeled rift tip Green’s function convolved with step source time function. The resulting modeled displacements, shown in black, have a longer decay and larger amplitude low-frequency displacements than the rift tip stack, shown in orange, for both bending moment and point load sources.	108
A.5	Modeled rift/margin Green’s function convolved with step source time function. The resulting modeled displacements, shown in black, have a longer decay and larger amplitude low-frequency displacements than the rift/margin stack, shown in green, for both bending moment and point load sources.	109
A.6	Modeled shear margin Green’s function convolved with step source time function. The resulting modeled displacements, shown in black, have a longer decay and larger amplitude low-frequency displacements than the shear margin stack, shown in purple, for both bending moment and point load sources. The modeled displacements arising from an applied bending moment are relatively similar to the shear margin stack, but the results of deconvolution do not support the hypothesis that the observations were generated by a step forcing in bending moment.	109
B.1	Sensitivity of ocean-coupled fracture model to magnitude of stress. Increasing the magnitude of applied stress strongly increases the average propagation rate and causes propagation to reach the Rayleigh wave speed c_r more quickly. Baseline stress R_{xx}^0 is computed by finding the magnitude of stress required to initiate rift propagation for the observed initial rift geometry. In each simulation, the R_{xx}^0 is perturbed by the additional stress shown in the legend. All other parameters are held fixed across simulations.	111

B.2	Sensitivity of ocean-coupled fracture model to ice thickness. Increasing the ice thickness decreases the average propagation rate and causes propagation to reach the Rayleigh wave speed c_r more slowly. All other parameters are held fixed across simulations.	111
B.3	Sensitivity of ocean-coupled fracture model to water depth. Increasing the total water depth H_c+H_w increases the average propagation rate and causes propagation to reach the Rayleigh wave speed c_r more quickly. All other parameters are held fixed across simulations.	112

I DEDICATE THIS WORK TO MY PAST AND FUTURE INCARNATIONS. WITHOUT YOU, I WOULD NOT HAVE REACHED SUCH HEIGHTS. WITHOUT YOU, I WOULD NOT KNOW WHO I STRIVE TO BECOME.

Acknowledgments

BEFORE ALL OTHERS, I must express my most sincere gratitude to Brad Lipovsky. I could not be more honored to complete this dissertation as your first student. Your guidance has profoundly shaped the way I see the world. The challenge of describing natural systems, once a source of great anxiety and confusion, has transformed into an adventure. Thank you.

My mentorship would not have been complete without Marine Denolle. You taught me to be hopeful in the face of discouragement, to always give ideas a try, and to trust my gut. You showed me what it means to be a powerful female scientist, and inspire me every day to follow in your footsteps. Thank you.

Without the unconditional support Brad and Marine offered, I would not be the person I am today. Your non-judgemental acceptance of my transition will always mean the world to me.

My time at Harvard was interspersed with thought-provoking conversations with Jerry Mitrovica. Never have I met someone who maintains such a high degree of interest and knowledge about so many topics, while cultivating a sense of humor and a knack for storytelling. Thank you for challenging me to grow, and for being there during the unexpected.

For reminding me that science can truly do good in the world, I offer my gratitude to Brent Minchew.

For helping me embrace brightness, lightness, and commiseration whenever needed, and for defining the first two years of my PhD, I thank Makoto, Marisa, Ben, and Ben.

I thank Bryan and Jack for friendship, companionship, and for being there with me in the darkest times. Your graciousness will never be forgotten.

For showing me sisterhood for the first time, I gratefully extend my love to Dani, Liv, Erin, Nicole, Jensen, Alysa, and Marcy.

The journey of self discovery I embarked on during my PhD was encouraged by Fen. Thanks for helping me set myself free.

My move to Seattle was unexpected, and it would have been much harder without the welcoming embrace of friendship by the members of the Earth and Space Sciences Department at the University of Washington.

For the sweet embrace of music and community, I will always fondly remember countless hours playing guitar on stage at MoJam every Monday. To the MoFamily- keep rocking!

Thank you Mom, Dad, and Ben. You keep me grounded and remind me to come back home.

0

Introduction

AS EARTH'S CLIMATE CHANGES, complex interactions between the ocean, atmosphere, solid Earth, and cryosphere will determine the future of human habitability across the planet. Warming of the ocean and atmosphere induces melting across large portions of Earth's ice, including floating ice in the Arctic, glaciers in alpine mountain ranges, and the large ice sheets in Greenland and Antarctica, with varied impacts that include elevated flooding hazard, reduced access to water resources, and sea

level rise. The reduction in habitable coastal area generated by sea level rise is expected to cause loss of human life, population displacement, economic crises, and geopolitical destabilization. Coastal communities, which in total contain about 40% of Earth's population, will bear the brunt of the hazard generated by sea level rise, with impacts disproportionately distributed to low-income, disenfranchised, and indigenous communities.

The distribution and magnitude of sea level rise depends on the total quantity and location of ice loss, ocean bathymetry, and the viscoelastic response of the Earth's crust and mantle. While the physics of sea level are relatively well-understood, significant uncertainties exist in the response of Earth's cryosphere to warming¹, contributing a high degree of uncertainty to predicted sea level rise under various warming scenarios². The majority of potential sea level rise is contained in Greenland and Antarctica, which both host large ice sheets that directly contact the ocean at their margins. As ocean and atmospheric warming progress, these ice sheets lose ice mass into the ocean through melting and ice discharge into the ocean at marine terminating glaciers. While Greenland currently makes the largest contribution to present sea level rise, the majority of potential sea level rise is overwhelmingly contained within Antarctic ice.

In the Antarctic Ice Sheet (AIS) and a small portion of the Greenland Ice Sheet (GIS), many coastal glaciers extend onto the ocean surface to form ice shelves. Ice flow across the grounding line – the flotation point of the ice sheet – makes an immediate contribution to sea level rise, referred to as ice dynamical loss, by displacing ocean water equivalent to the water mass stored in the newly-floating ice. In equilibrium, meltwater runoff and ice dynamical loss from the AIS are balanced by the inland accumulation of snow, keeping the mass of the AIS constant. However, the AIS has been in a negative mass balance regime since at least the 1980s³, and continued warming of Earth's atmosphere and oceans is will only further drive the AIS into disequilibrium.

Because ice that flows across the grounding line makes an immediate contribution to sea level rise by displacing an equivalent mass of ocean water, it follows that the melting of floating ice does not

contribute to sea level rise. In actuality, the melting of floating ice makes a very modest contribution to sea level rise due to the difference in densities of saline ocean water and fresh water stored in floating ice, equivalent to $\sim 2.6\%$ of the water volume displaced by floating ice⁴. If the mass associated with melting ice shelves only minimally contributes to sea level rise, can ice shelves be ignored when studying the response of the Antarctic ice sheet to climate warming? Can attempts to understand the future of sea level focus entirely on the flow and melt of grounded ice?

It has long been theorized that ice shelves resist the flow of grounded Antarctic ice^{5,6,7}. Ice shelves experience a drag force along their entire contact surface with land, significant considering that ice shelves exist predominantly within embayments. This includes ice shelf lateral margins, any bathymetric high points that contact the ice shelf base, and any islands that obstruct the forward flow of ice. The drag force exerted along these contact surfaces resists the gravitational stress driving glacier flow across the grounding line. In this way, ice shelves provide a backstress that buttresses the AIS and limit the rate of ice dynamical loss. When ice shelves shrink in thickness or lateral extent, the total backstress that regulates upstream flow speed is reduced. Simply put, ice shelf mass loss and disintegration enhance upstream ice flow and dynamical ice loss. This was definitively observed when the 2002 collapse of the Larsen B ice shelf led to acceleration of the glaciers it once buttressed^{8,9}.

Antarctic ice mass loss is dominated by West Antarctica Ice Sheet (WAIS), a sector of the AIS containing a potential 3.26-4.78 m contribution to global mean sea level^{10,11}. Presently, ice loss from WAIS is concentrated in the Amundsen Sea Embayment, and the majority of ice loss within the Amundsen sector comprises ice dynamical loss from Pine Island Glacier and Thwaites Glacier, a pair of large glaciers that have been rapidly accelerating and thinning since first measured in the 1990s. In total, the Amundsen drainage basin contains a potential 1.2 m contribution to global mean sea level¹², and the rapid pace of mass loss suggests that the region may play a critical role in determining Earth's sea level in the next 500 years. The ice shelves that buttress Pine Island Glacier (PIG) and Thwaites Glacier therefore regulate the dynamic mass loss and sea level contribution

of the WAIS. As these ice shelves continue to shrink, ice loss from WAIS is expected to continue accelerating.

Furthermore, the proposed instability of marine ice sheets presents a possible mechanism for collapse of the entire WAIS. Because the ice sheet is grounded below sea level, ice at the grounding line is exposed to ocean water, which drives melting and thinning. Once ice at the grounding line thins sufficiently, it begins to float, causing the position of the grounding line to retreat toward the ice sheet's interior. If the bed slopes upward toward the ice sheet's interior, a retreating grounding line will stabilize where the bed height exceeds the local sea level. If, however, the bed deepens toward the ice sheet's interior, a retreating grounding line will invariably expose deeper ice to ocean water that drives melting, thinning, and successive grounding line retreat. This positive feedback may then progress until the entire ice sheet collapses. Because WAIS is grounded below sea level on a progressively deepening bed, scientists have theorized since the 1970s that WAIS may be in the early stages of collapse induced by marine ice sheet instability^{13,14,6,15}. However, the apparent unconditional instability of the marine ice sheets with deepening beds is mitigated by ice shelf buttressing^{16,17}, which can prevent the unstable grounding line retreat predicted by simple models of marine ice sheet dynamics. For rapid collapse of the WAIS to progress as predicted in the most dire scenarios, then, the disintegration of ice shelves that buttress large outlet glaciers like Pine Island Glacier and Thwaites Glacier is a necessary precondition.

Because ice shelf buttressing modulates ice dynamical losses and mitigates the potential for marine ice sheet instability, accurately predicting the future behavior of the AIS requires understanding the mechanisms of ice shelf mass loss. Ice shelves lose mass through basal melting and iceberg calving, which both reduce the total area of the contact surface between shelf ice and bedrock, thereby reducing buttressing.

Along the bases of floating ice shelves, cold ice contacts ocean water. The ocean water beneath the ice shelf base can range in temperature from a few degrees above 0°C or below 0°C, possible

due to the freezing point depression induced by salinity. The exact distribution of water temperature beneath ice shelves remains largely unconstrained due to the extreme difficulty of direct distributed temperature measurements beneath ice shelves, but are likely determined by the complex interplay of regional ocean currents, local thermohaline circulation, basal melt, and tidal mixing. In the Amundsen Sea Embayment (ASE), ice shelf melt is primarily driven by the incursion of warm Circumpolar Deep Water into the cavities beneath ice shelves. Circumpolar Deep Water is a mixture of water from the Atlantic, Indian, and Pacific oceans, transported around the Earth between 40°S and 60°S by the strong wind-driven Antarctic Circumpolar Current^{18,19}. Circumpolar Deep Water is funneled towards the ASE by a series of glacially-carved bathymetric troughs and canyons that transport warm water along the sea floor and into the cavities beneath the ASE's ice shelves. The resulting strong temperature stratification in the subshelf cavity is thought to drive circulation that brings warm water to the grounding line and along the ice shelf base, generating basal melting that thins the ice shelf and retreats the grounding line.

While the relative contribution of basal melt and calving in buttressing loss are approximately equal²⁰, basal melt is unlikely to cause rapid changes in ice shelf extent and buttressing. Calving and fracture, on the other hand, can cause significant ice front retreat, buttressing loss, and ice shelf disintegration at a rapid pace. Understanding ice shelf stability therefore requires a robust understanding of the fracture mechanisms that underlie calving. Emphasis has been placed on hydrofracture due its implication in the retreat and collapse of ice shelves on the Antarctic Peninsula, including the rapid disintegration of the Larsen B ice shelf, leading some authors to propose hydrofracture as the primary mechanism of ice shelf retreat^{21,8,22}. Yet virtually no observations of ice shelf retreat due to hydrofracture exist beyond the Antarctic Peninsula, whose total volume of ice corresponds to only 0.24 m of global mean sea level rise²³, an order of magnitude less than the total contribution of the WAIS.

The largest icebergs are shed when through-cutting fractures called rifts propagate across ice

shelves to create icebergs with areal extents of $O\{1 - 10 \times 10^3\}$ sq km²⁰, referred to as tabular icebergs. Rifts often initiate in regions of concentrated shear stress and advect downstream on timescales of years to decades before eventually propagating and calving tabular icebergs. Because of the cyclic nature of rift initiation, propagation, and calving, rifting has typically been treated as a steady, background calving process that maintains an equilibrium ice front position^{24,25,20} with little bearing on the future of Antarctica's ice shelves. Yet climate warming continues to push the AIS into a state of disequilibrium with sweeping impacts on the behavior of the coupled cryospheric, oceanic, atmospheric systems that act in concert to determine the future of the AIS. Recent observations suggest that the dynamics of rifting at Pine Island Glacier, long heralded as the Achilles heel of the WAIS¹⁵, are responding to changes in ocean forcing, ice dynamics, and ice shelf geometry by opening more frequently at new orientations that reduce buttressing and drive further acceleration^{26,27}.

Rifting remains a challenging physical process to observe. Many rifts in Antarctica's largest ice shelves, like Ross Ice Shelf, appear to be stable on decadal timescales with little or no extension since their observation began. In contrast, rifts on highly dynamic ice shelves like Pine Island Glacier initiate, propagate, and calve icebergs every few years. While remotely-sensed instruments can accurately measure the large-scale flow of the AIS, the wide range of timescales over which rifts grow make remote observation inherently challenging. Gradual rift propagation is readily measured by remote sensing, but propagation on timescales less than the multi-day revisit interval of most satellite instruments is inherently aliased in remotely sensed observations. Because the response of ice to stress is dominantly elastic on timescales less than about 11 hours²⁸, remotely sensed observations are unable to constrain whether rift propagation is an elastic or a plastic deformational process due to their limited temporal resolution.

As a consequence, no consensus exists on the proper rheological treatment of rifts in models of ice shelf evolution. Methods that employ linear elastic fracture mechanics (LEFM), continuum

damage mechanics, and flow-derived rift widening rates have all been used to model ice shelf rifts, with individual models typically designed to simulate specific observed instance of rifting or to understand the general behavior of rifts. Despite years of progress, no unified method exists for modeling the diverse range of rift behavior, due in large part to the challenges of observing rifting with remote sensing and the extremely limited quantity of in-situ data that capture rift propagation.

Seismological instrumentation has successfully been employed to continuously monitor the elastic wave emissions from rifts and observe their behavior on short timescales. Seismic records of gradual and episodic rift propagation on a few of ice shelves show that large-scale rift growth is a result of the accumulation of many individual brittle fracture events. Despite the promising results of rift seismology, the demanding field campaigns and logistical complexity of instrument deployment and data retrieval have limited the total number of ice shelf seismic studies. Indeed, the actively-deforming and highly dynamic areas that seismic studies seek to target are the least accessible and most hazardous. As a result, the geometry of ice shelf seismic arrays is invariably far from ideal. Instruments are often clustered in only a small portion of the region of interest and are never deployed frontward of a major rift because iceberg calving will render the data irretrievable. Because of the unpredictable timing of major rifting events and the logistical complexity of ice shelf seismic deployments, no seismic studies have recorded the entire rifting and calving sequence of a major tabular iceberg to date. Furthermore, seismic studies have been unable to capture any instances of truly rapid rifting despite evidence that such events do occur.

Critical questions about the physics of rifting remain unanswered. Are rifts sensitive to environmental stresses, or are they controlled solely by the background ice flow dynamics that drive ice shelf extension? How do the ice shelves move and flex in response to rifting? Do rifts propagate through brittle fracture? How quickly can rifts propagate? Do rifts present a mechanism of rapid ice shelf collapse and loss of buttressing?

In this thesis, I present the results of my work using seismic data to characterize a diverse range of

fracture process at ice shelf rifts to answer the questions posed above. I augment analyses of seismic data using a diverse range of data types including weather station data, GPS data, satellite optical imagery, and satellite synthetic aperture radar (SAR) data. By synthesizing all available data recorded near each study site during the time periods of interest, I relate the seismically-observed rift processes to environmental phenomena and ice dynamics. Whenever possible, I develop simple mechanical models to test hypotheses about rift processes and aid in drawing inference from observations. In this way, I seek to advance human understanding of the interconnected web of processes that control Antarctic ice shelf rifting and the tenuous balance of the Antarctic Ice Sheet.

In the first chapter, I monitor fracturing at a stagnant rift in the Ross Ice Shelf. I show that even stagnant rifts are subject to considerable fracture that manifests in thousands of tiny icequakes that radiate seismic energy across the ice shelf. I show that the rift at the focus of the study is sensitively coupled to environmental stresses arising from seasonal temperature change and ocean tides, but not from ocean wave activity.

In the second chapter, I analyze the seismic signatures of fracture on Pine Island Glacier ice shelf. I find that fracture at the shear margin and a gradually-propagating rift excites flexural gravity waves, a type of wave that propagates due to interactions between ocean surface displacement and ice shelf bending. I present the first record of the icequake sequence leading up to a major tabular calving event, finding that elevated rift fracture beginning months prior to calving corresponds to a phase of increasing ice speed and basal melt. These results suggest that rift seismicity may be a precursor to calving and highlight the coupled nature of rifting, ice dynamics, and ocean forcing. Finally, I use a model of flexural gravity wave propagation to infer the source characteristics of the forces that generate the recorded seismicity, offering constraints on the size and speed of the individual brittle fracture events that cumulatively result in large-scale propagation of the rift.

In the third chapter, I present observations of the fastest known episode of rift propagation. Using seismic and SAR data, I identify 10.5 km of rift propagation that occur in a matter of minutes

at an average rate of approximately 35 m/s, showing conclusively that rifts can open through rapid brittle fracture. Then, I derive a novel coupled model of rift fracture and ocean water flow, finding that the speed of rapid rifting is hydrodynamically limited. In this work, I characterize a new class of rift propagation behavior, representing a significant advancement in understanding of rifting and suggesting that rifting may be capable of causing rapid loss of ice shelf buttressing.

In the fourth chapter, I extend the scope of my work to the dynamics of a tidewater glacier in West Greenland. Using data from the first distributed acoustic sensing deployment in a glacier borehole, I characterize meltwater transport and relate seismic noise generated by water flow to basal water pressure and ice flow speed. I also develop and apply an efficient cross correlation algorithm that reveals information about the material properties and structure of the glacier.

While the work here is motivated by a sincere desire to do my part in understanding our changing planet, I nonetheless found great beauty in the five years I spent listening to Earth's ice. As ice slides, stretches, and cracks, it plays such delicate and crystalline music, heard only by those who listen. As climate warming continues to push Earth's ice into flux, I take some solace in the wonder of bearing witness to the symphony of dynamics that unfolds with each passing day. In science as in life, the most marvelous mysteries can be unraveled simply by listening.

*Although I thought my roots were deep
I sank them into hillsides steep
And riverbanks that soon erode
And canyons that have overflowed*

Phish

1

Tidal and Thermal Stresses Drive Seismicity along a Major Ross Ice Shelf Rift

This work was first published in part as the author's senior thesis at Washington University in St. Louis:

Olinger, S. D., & Wiens, D. A. (2018). Microseismicity along major ross ice shelf rift resulting from thermal contraction of the near-surface firn layer. *Washington University Spring 2018 Senior Honor Theses*, 95.

The complete work was published in *Geophysical Research Letters*:

Olinger, S. D., Lipovsky, B. P., Wiens, D. A., Aster, R. C., Bromirski, P. D., Chen, Z., Gerstoft, P., Nyblade, A. A., & Stephen, R. A. (2019). Tidal and thermal stresses drive seismicity along a major ross ice shelf rift. *Geophysical Research Letters*, 46(12), 6644–6652.

UNDERSTANDING MARINE ICE SHEET STABILITY under various climate scenarios motivates ongoing discourse about the nature and forcing of fracturing processes in floating ice shelves. Brittle deformation of large ice shelves is dominated by the propagation of large, through-cutting fracture-propagated rifts²⁵. Debate has largely focused on the relative importance and interactions of ocean wave-induced stresses^{29,30,31,32,33,34,35,36,37}, glacial stresses^{38,39,40}, and rift-filling melange^{41,42,43,44}. Seismic observations have the ability to quantify small scale brittle deformation in the form of icequakes, and thus provide an efficient means to investigate the spatial and temporal extent of ice shelf fracture processes^{45,46,47,48}.

As part of two coupled projects to study the dynamics of the Ross Ice Shelf (RIS) and the solid Earth structure beneath³⁵, 9 broadband seismographs were deployed spanning both sides of a large rift located about 150 km south of the RIS front (Figures 1.1 and 1.2), denoted as WR₄⁴⁹. This deployment provides an important opportunity to investigate the role of various processes that drive ice shelf fracture. LeDoux et al.⁴⁰ found that rift WR₄'s eastern tip currently is located adjacent to a suture zone, a region of deformed ice that arrests rift propagation, and multi-year imagery has confirmed that WR₄ is not actively propagating⁴⁹. Despite WR₄'s apparent inactivity, the RIS array detected numerous icequakes in the vicinity of the rift, which we use to determine whether the rift is undergoing active brittle deformation and to provide constraints on the forces influencing rift propagation.

1.1 DATA

1.1.1 SEISMIC DATA

This study uses data collected by two simultaneous collaborative seismograph deployments on the Ross Ice Shelf. We use 9 seismic stations deployed along two lines that intersect near 78.96°S, 179.88°W (Figure 1.1). These stations are a subset of the 34 seismic stations that were deployed

across a much larger region (Figure 1.1). Each station consisted of a Nanometrics T120 PHQ broadband seismometer buried about 1 meter into the firn recording at 200 samples per second and a Quanterra Q330 datalogger. The equipment was powered by solar panels in the austral summer and by lithium batteries in the winter. The instruments were deployed in November 2014 and the first year of data was retrieved November - December of 2015. The instruments were recovered, and the final year of data was retrieved in November - December of 2016.

1.1.2 WEATHER AND ENVIRONMENTAL DATA

Temperature data from the Automatic Weather Station (AWS) project was used to investigate whether seismicity is correlated with meteorological phenomena. The AWS weather stations are deployed across Antarctica and record temperature, pressure, wind speed, and humidity⁵⁰. Because of its proximity to the array and the completeness of its records, we use data from station Gill, located at 79.823°S, 178.536°W at a distance of 80 km from the center of the array.

1.2 METHODS

1.2.1 DETECTION AND LOCATION

We utilized an automated short-term average/long-term average (STA/LTA) event detection routine to form a catalog of any local activity recorded on stations with a high signal-to-noise ratio. We detected 5948 unique events throughout both years of data after manually removing all detections of non-local seismicity (Figure 1.3). To generate arrival times and to analyze the similarity of the detected events, we applied a cross-correlation and clustering algorithm to the entire dataset. However, the events did not exhibit high correlation values, and the clusters generated were not consistent across different stations and components, indicating that, unlike many icequakes, the events are not true repeating events.

We initially located a subset of the largest events from 2015 using manually-picked P and S wave arrival times. However, direct P and S wave arrivals were often small and emergent, making it difficult to pick arrival times consistently. Because vertical component Rayleigh wave arrivals were much easier to identify, we located the entire dataset using Rayleigh wave arrival times. We calculated envelope functions for each event waveform on DR₁₄, DR₁₃, DR₁₂, DR₁₁, DR₁₀, DR₀₉, DR₀₈, DR₀₇, and RSo₄. Because these icequake waveforms are dominated by surface waves, the maximum value of each envelope function corresponds to the arrival of Rayleigh waves. A STA/LTA threshold was also applied to prevent incorrect identification of arrivals. Using this process, Rayleigh arrival times were automatically generated for all 5948 events.

We located the events that had Rayleigh phase arrivals on more than five stations. We first used a simple grid-search algorithm that minimized the misfit between observed and predicted Rayleigh arrivals by calculating a summed squared error for each potential location in the grid and selecting the lowest error point. In order to calculate misfit, we back-propagated the arrivals and took the mean time as the origin time. Once satisfactory locations were obtained from the grid-search, we removed arrivals from stations with travel time residuals greater than 1 second for each event. Events now with less than five arrivals were removed, and the remaining events were relocated using a standard iterative least-squares inversion. From the resulting locations, those with location and origin time standard deviations greater than 2 km and 2 seconds were removed, and the remaining 2515 events were relocated using a double-difference relative location method.

To determine an accurate Rayleigh phase velocity for use in event relocation, grid-search locations were calculated using an initial velocity of 1.5 km/s. We then selected all events aligned with DR₁₃, DR₁₂, and DR₁₀ and calculated the time difference between arrivals on DR₁₃ and DR₁₂, DR₁₃ and DR₁₀, and DR₁₂ and DR₁₀ to obtain estimates of Rayleigh velocity largely independent of source locations. A least-squares inversion was then used to determine the velocity that minimized the misfit between the observed and predicted arrival time differences calculated us-

ing the known distances between stations. This calculation resulted in a Rayleigh velocity of 1.55 km/s, which was then used in the grid-search, linearized inversion, and double-difference location methods. This Rayleigh wave velocity is similar to that predicted for a structure of slow velocity firm overlying ice.

1.2.2 MAGNITUDE CALCULATION

To constrain the size of the icequakes and to allow for better physical interpretation of the events, we calculated the local magnitude of events using the local magnitude formula (Stein and Wysession, 2003):

$$M_L = \log \frac{A}{T} + 2.76 \log D - 2.48 \quad (1.1)$$

where A is the maximum amplitude of the event waveform in microns, T is the period, and D is the distance from the event to the receiver in kilometers. We used a script to automatically retrieve the maximum amplitude of each located event on DR14, DR13, DR12, DR10, and DR09. Because many of the events were too small to be located, magnitudes were only calculated for located events.

1.2.3 COMPARISON WITH ENVIRONMENTAL AND WEATHER PHENOMENA

To investigate the relationship between rift seismicity and the atmosphere, we compare the timing of seismicity with Automatic Weather Station air temperature data from 2015 and 2016⁵⁰. We also compare the timing of events with tidal phase and tidal slope. Tidal heights were obtained by running the CATS2008 model, an update to the model described by Padman et al.⁵¹, for the duration of the deployment at the center of the array (DR10). To find the time of each high tide, local maxima were calculated for the dataset. We then calculated the difference in time between each event and the most recent high tide. The resulting times were binned by hour, yielding the number of events that occur in each hour after high tide. Finally, we divided by the total length of the corre-

sponding tidal cycle to yield a measure of event timing binned by tidal phase. We calculated the slope at the ice shelf by running the CATS2008 model at both the grounding line (82°S, 164°E) and the front (78.5°S, 179°E), finding their difference, and dividing by the distance between the two points.

To investigate swell and infragravity waves, we made a spectrogram of the long period horizontal north-south component data from DR10. Previous work by Bromirski et al.⁵² found that IG waves generate greater horizontal displacements than vertical displacements on RIS, so we used the horizontal component data for our analysis of ocean swell and IG waves. Before generating a spectrogram, we first removed the instrument response to displacement on the frequency band 0.015 Hz - 0.2 Hz. To find swell band power, we integrated the spectrogram over the frequency band 0.03 Hz - 0.15 Hz for each window used to produce the spectrogram. To find IG band power, we integrated the spectrogram over the frequency band 0.015 Hz - 0.03 Hz for each window used to produce the spectrogram. These frequency limits were selected based on the ocean wave classification presented in Toffoli & Bitner-Gregersen⁵³.

1.2.4 SEASONAL VARIATION IN NOISE FLOOR

In the Antarctic winter, sea ice extends for many kilometers beyond the edge of the Ross Ice Shelf and causes a significant decrease in seismic background noise by damping out ocean and wave-generated signals. In the summer, however, the ocean-ice interface is far closer to the array of seismometers, introducing a large amount of noise (Anthony et al., 2015; Wiens et al., 2017). To investigate whether the observed trend in event timing is biased by seasonal noise, we determined a summer detection threshold and examined the timing of events only detectable in summer. We found the summer detection threshold by first calculating average amplitudes on DR14 and DR13 for all summer events and then constructing a plot of event count and amplitude. This analysis revealed that events with average amplitudes greater than 0.01 μm are reliably detectable in the summer. We

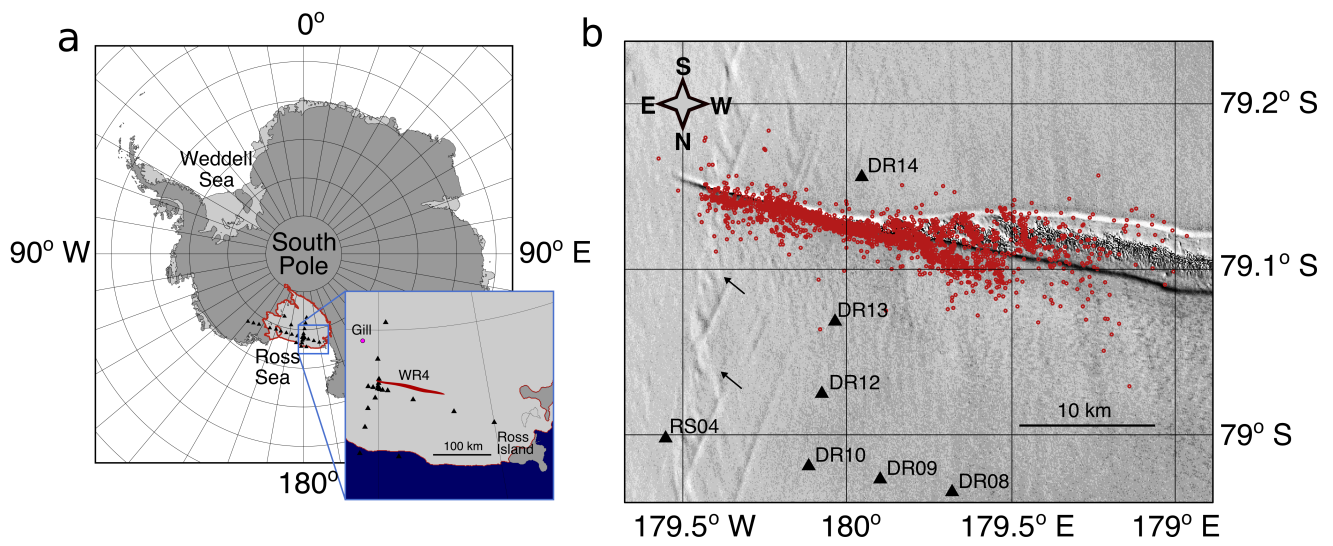


Figure 1.1: Study site and icequake locations. (a) Locations of rift WR4, the seismograph array, and weather station Gill on the Ross Ice Shelf. Data from stations DR07 and DR06 (not shown) was additionally used to locate icequakes. (b) Locations of 2500 icequakes at WR4. East of about 180°, icequake locations fall along central axis of rift; west of 180°, icequake locations fall within en echelon features containing rift-filling melange. Arrows indicate suture zone fabric.

then made a plot of event timing and seismicity that included only events with amplitudes exceeding $0.01 \mu\text{m}$ in both winter and summer. The result shows the same seasonal pattern in seismicity and swarm occurrence, suggesting that the observed seasonal variations in seismicity are real and not a factor of reduced detectability (Figure 1.4).

1.3 CHARACTERISTICS AND LOCATIONS OF RIFT SEISMICITY

Icequakes with high signal-to-noise exhibit distinct P, S, surface wave, and longitudinal plate wave arrivals⁵⁴. Icequake events are lower frequency than similarly-sized tectonic earthquakes⁵⁵ with peak amplitudes between 1-4 Hz. In all cases, the icequake-associated surface waves have the largest amplitudes. We find that the icequakes range in size from $M_L = -2.5$ to $M_L = 0$ (Equation 1), and there is evidence for a b-value greater than 1 based on the statistics of larger magnitude events, indicating that this sequence of icequakes has a higher ratio of small to large events than predicted by a

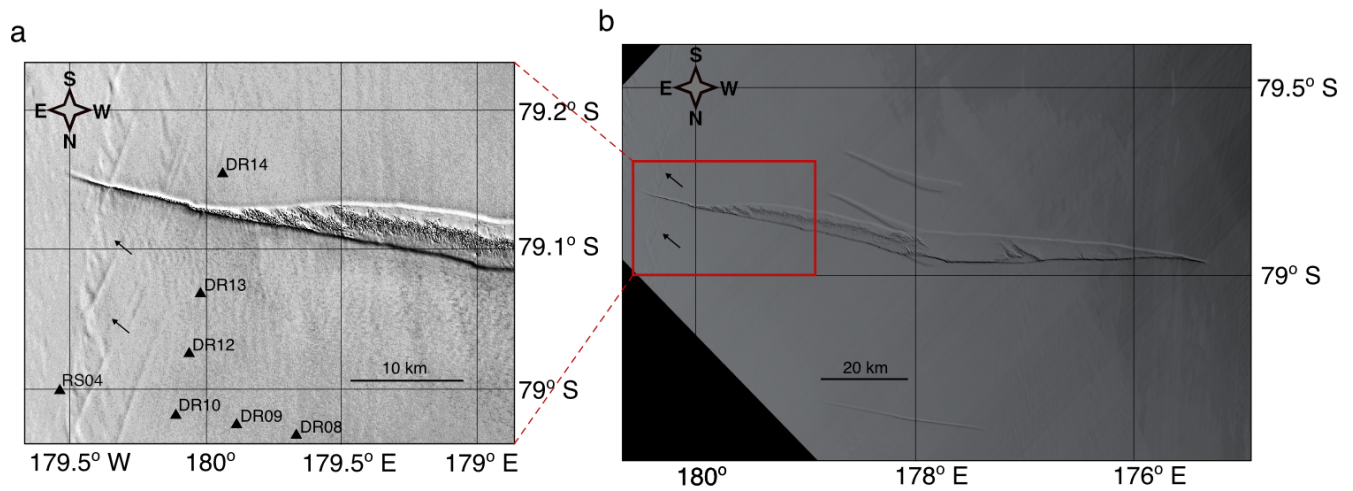


Figure 1.2: Rift imagery. (a) Imagery of rift's eastern end showing en echelon features in rift filling melange. To offer a clear view of rift morphology, icequake locations are not plotted. (b) Imagery of entire rift showing widening at its center. Arrows indicate suture zone fabric.

standard Gutenberg-Richter distribution. Typical waveforms are shown in Supplementary Figure I.3.

The icequake epicenters were located using a double difference method and automated picks of peak Rayleigh wave arrival times on the vertical component seismogram. The icequakes are located along a 30 km segment of the rift (Figure I.1), associated with three broad regional patterns of icequake activity. First, icequakes located east of about 180°E are aligned with the central axis of the rift. Because the observed icequakes have high amplitude surface waves relative to body waves, it is likely that the icequakes occur near the ice shelf surface⁵⁶. Possible sources include fracture along the upper edges of the rift walls and collision, settling, or fracture of the blocks of ice within the melange.

Second, many of the icequakes west of about 180°E occur along a series of en echelon features within the wider region of rift-filling melange. Because the standard deviations of relative icequake locations are typically around 100 m and because of the strong spatial association of the events with

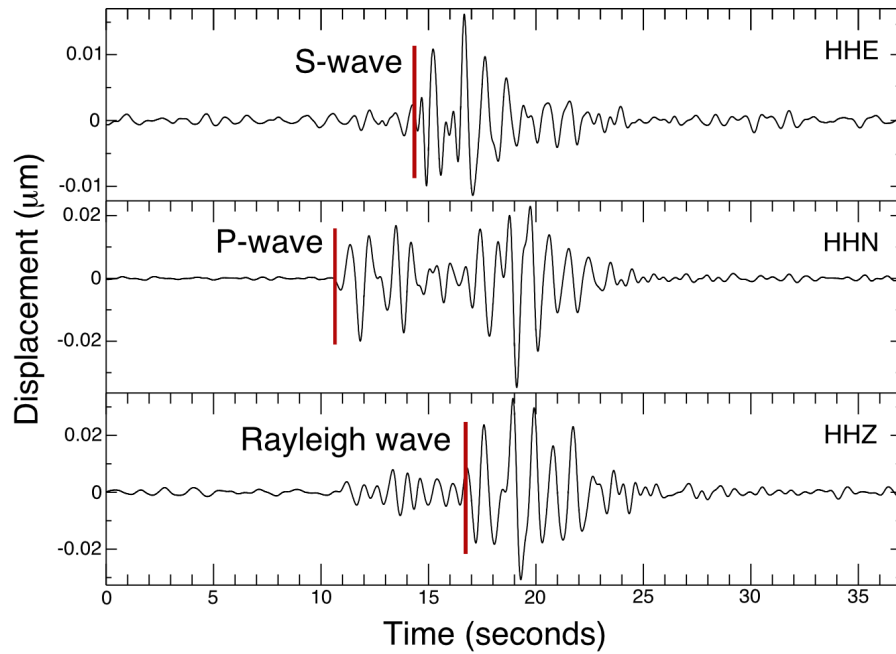


Figure 1.3: Icequake waveforms. HHE (horizontal east-west) component seismogram, HHN (horizontal north-south) component seismogram, and HHZ (vertical) component seismogram filtered on 1-3 Hz for icequake on 2015:011:21:59:40.

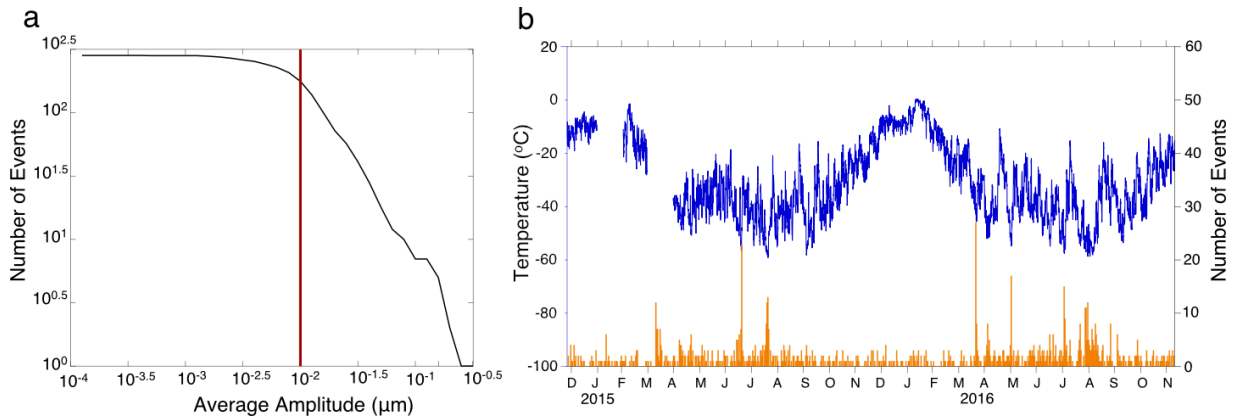


Figure 1.4: Seasonal changes in noise floor. (a) Determination of $0.01 \mu m$ summer detection threshold. (b) Histogram of all events with average amplitude (DR13 and DR14) greater than $0.01 \mu m$. Despite changes in event detectability due to retreating sea ice, seasonal patterns in event timing still correlate well with temperature.

the en echelon shear zone features, we are confident that these events originated within the melange and were not incorrectly located events occurring along the rift walls. We therefore interpret this second group of icequakes to be caused by deformation of the rift-filling melange. Because events in the melange begin to occur where the rift widens, we speculate that the type of brittle ice shelf deformation recorded here may cause widening at the middle of the rift. Figure 1.2 shows a detailed view of rift morphology.

Third, events decrease in number west of about 179.5°E and distant events are typically less precisely located. To determine whether the apparent concentration of icequakes is an artifact of our network geometry, we examined the magnitude of the events at various positions along the rift. We find that the prevalence of low magnitude events decreases with distance from the intersection of the array and the rift, suggesting that the apparent decrease in seismicity away from the network may be the result of attenuation of similar-sized signals from more distant icequakes. It is therefore possible that relatively uniform levels of seismicity occur along the entire rift.

Icequakes are not clustered in front of the rift tip as was previously observed at the actively-propagating Loose Tooth Rift in the Amery Ice Shelf^{57,46} but instead cease abruptly where the rift reaches the adjacent suture zone at around 179.5°W . This decrease in seismicity is not due to reduced array detection capability to the west, as very small events are detected in the rift near the rift tip. We interpret the lack of icequakes at the rift tip to indicate a lack of brittle deformation in this region. Since westward propagation of the WR₄ rift tip has currently stagnated^{49,40}, our inferred lack of brittle deformation is therefore consistent with rift stagnation in suture zones^{39,58,59,60}.

1.4 OCEAN TIDES CONTROLS DIURNAL PATTERNS IN SEISMICITY

We observe tidal modulation of the icequake activity (Figure 1.5a). As tides rise, the level of seismicity increases until about 5 hours after high tide, when the level of seismicity begins to fall. The

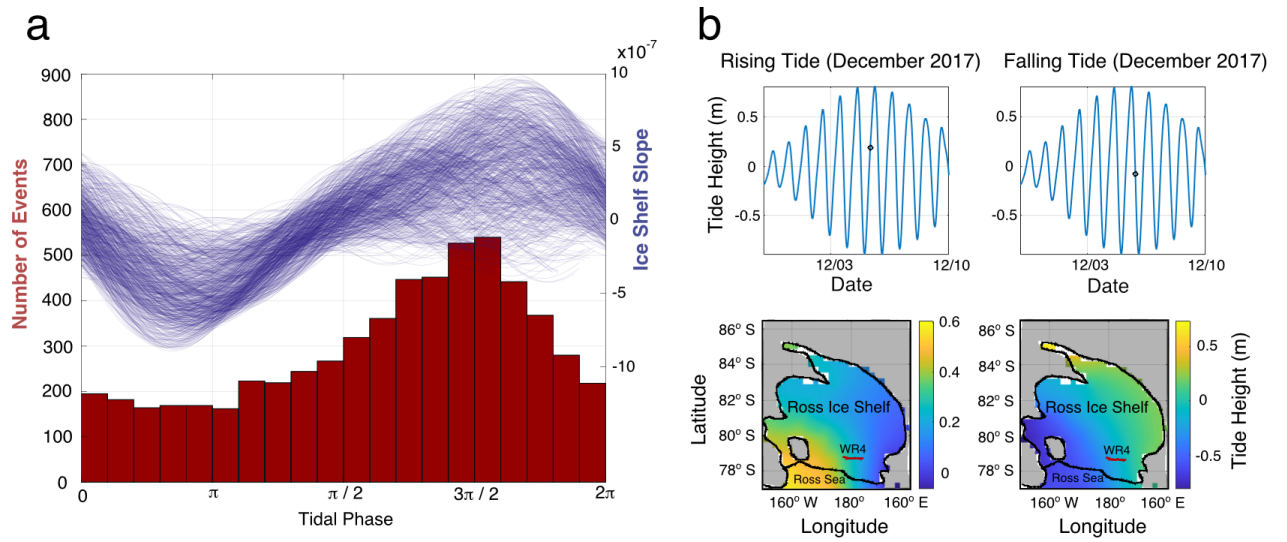


Figure 1.5: Tidal slope and rift seismicity. (a) Histogram of event timing as a function of tidal phase plotted with ocean surface slope (blue lines) for each tidal cycle during the duration of the deployment. (b) Modeled tidal heights at 81.75°S , -175°W , the center of the ice shelf (top), and in map view across the RIS (bottom) demonstrating the ocean surface slope relationships shown in (a). Red dots in the top figures identify the timing of the ice shelf height maps. Tidal heights were obtained using the CATS2008 tidal model⁵¹.

timing of events within a day is well-correlated with the tidally-modulated slope of the ice shelf, with the highest seismicity rates when the entire Ross Ice Shelf slopes downwards toward the ocean (Figure 1.5b). When the shelf tilts, a horizontal component of gravitational force arises in the plane of the ice shelf. If the shelf is tilted towards the continent, the rift is under compression and we see low levels of seismicity; if the shelf is tilted seawards, the rift is subjected to additional extensional stress and we see high levels of seismicity. Using the CATS2008 tide model⁵¹, we find that this 5-hour delay corresponds to a maximum tidally-induced tilt of the entire Ross Ice Shelf (Figure 1.5). We calculate the maximum stretching stress that could affect the rift associated with this tilt to be $\rho_i g \alpha L$ where ρ_i is the ice density, g is the acceleration due to gravity, L is the distance from the rift to the ice front, and α is the tidally-induced tilt angle. For $\alpha = 10 * 10^{-7}$, this suggests maximum stretching stresses on the order of 1 kPa, in agreement with stress due to sea surface tilt calculated by Bassis et al.⁵⁷. Our findings are consistent with previous observations of tidally-modulated glacial seismicity^{61,62} and tidally-modulated ice shelf flow^{63,64}. Furthermore, they suggest that stretching stresses from tidal cycles are preferentially released at rifts and may be associated with the processes that widen rifts after formation.

1.5 TEMPERATURE CONTROLS MULTI-DAY AND SEASONAL PATTERNS IN SEISMICITY

The detected icequakes exhibit a distinct seasonality that correlates with surface temperature data (Figure 1.6a). Temperature data was recorded by station Gill (Figure 1.1) of the Antarctic Weather Stations project⁵⁰, at a distance of 80 km from the center of the array. In the Antarctic summer (Dec/Jan/Feb), very low levels of seismicity are observed. However, as soon as temperatures begin to decline rapidly at the beginning of winter in both 2015 and 2016, the average number of events per day increases dramatically, with days containing over 20 events becoming common. Furthermore, large and rapid decreases in temperature appear to be associated with days of particularly high

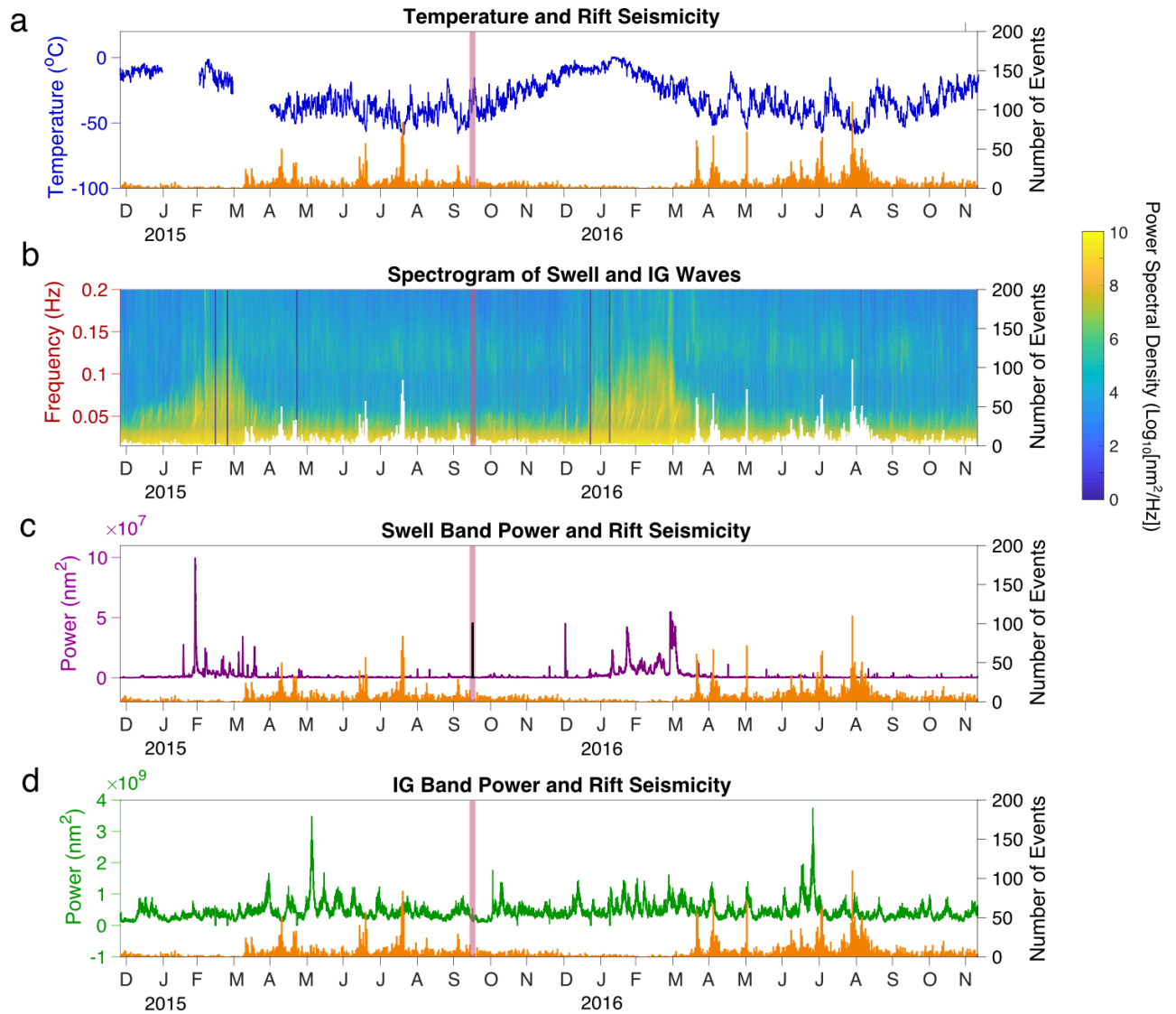


Figure 1.6: Ocean swell, infragravity waves, temperature and rift seismicity. (a) Surface temperatures from AWS station Gill (blue) plotted with the histogram of rift seismicity (orange) as a function of time during the deployment. (b) Spectrogram showing swell and infragravity wave band power. Black bars indicate data gaps. (c) Ocean swell power (purple line) in the frequency band 0.03 - 0.15 Hz plotted with the histogram of rift seismicity. (d) Infragravity wave power (green line) in the frequency band 0.015 - 0.03 Hz, plotted with the histogram of rift seismicity. Spectral analysis used long period north-south component data from station DR10. The Illapel, Chile tsunami arrival is indicated in pink on each panel of the figure. The seasonal trend in seismicity corresponds to seasonal temperature variation, and wintertime swarms coincide with periods of extreme cold and not with swell or infragravity waves.

activity. The coldest periods of 2015 and 2016 both correspond to days with the largest number of icequakes. Although seismic noise levels are highest in the summer, examination of the temporal pattern of the larger events shows that the seasonal pattern of seismicity is not due to the seasonality of the seismic noise floor (Figure 1.4).

There are two potential mechanisms that could account for the correlation between icequake activity and temperature. First, ice experiences low temperature embrittlement when loaded in compression⁶⁵. It is therefore plausible that tidal stresses result in ductile deformation at high temperatures but brittle icequake-related deformation at lower temperatures. This explanation is consistent with studies that find seasonal variability of ice shelf material properties³⁴.

Second, the uppermost portion of the ice experiences thermal contraction in response to rapid temperature drops, and would thus be under tensional stress, as is observed for sea ice during cold weather^{66,67,68}. Similar behavior has been observed in some alpine glaciers, which exhibit thermal fracturing in response to cold night-time temperatures^{69,70}. Although we have not obtained source parameters for these events, the association between the icequakes and tensional tidal stress, and their location in a rift zone, suggest that the events are dominantly tensional. Since both the tidal and the thermal mechanisms produce horizontal tensional stress, it is likely that they act in concert. Because short-period temperature fluctuations only propagate to a depth of several meters in glacial ice⁷¹, shallow icequake locations are consistent with the correlation between icequake activity and surface air temperatures. However, we note the possibility that enhanced cold air circulation within the rift may cause thermal contraction deeper in the ice than would otherwise be possible.

1.6 RIFT SEISMICITY IS INSENSITIVE TO OCEAN SWELL AND INFRAGRAVITY WAVES

Both ocean swell and infragravity (IG) waves are poorly correlated with seismicity at WR4. We analyze the contribution of swell and IG waves by spectral analysis of the horizontal north-south

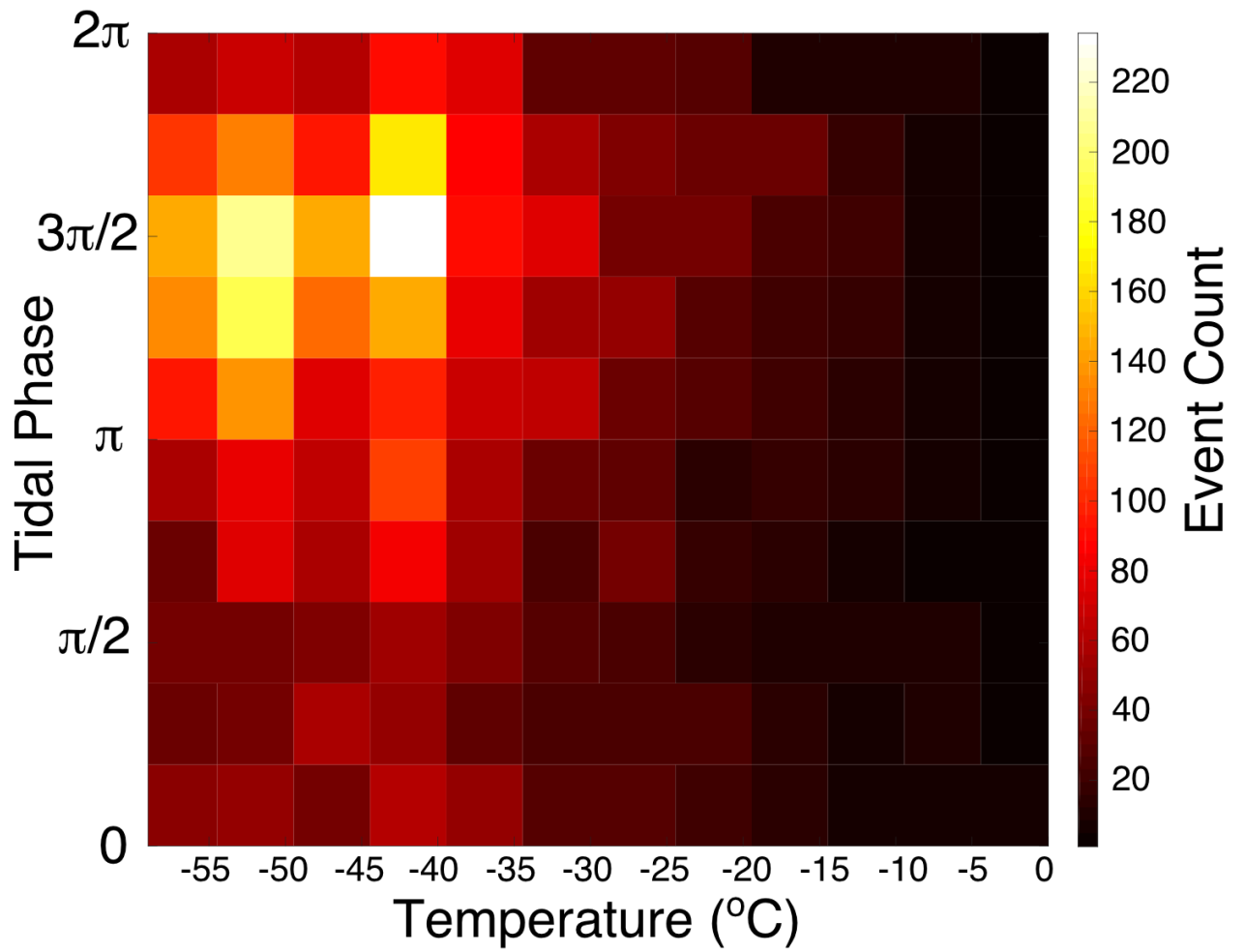


Figure 1.7: Density plot of number of events as a function of tidal phase and temperature. Temperature data is from weather station Gill (Figure 1.1). Peak levels of seismicity are observed when temperature is low and when the shelf is most highly sloped downward toward the ice front during falling tide.

component data from station DR10, since ocean waves generate large horizontal displacements on RIS⁵². Because sea ice attenuates ocean waves³⁷, swell energy only reaches the array during the austral summer, when seasonal sea ice is minimal in extent. Rift seismicity is far less frequent in the austral summer than in the winter, and periods that contain significant swell energy correspond to very low levels of seismicity at the rift (Figure 1.6b, 1.6c). Furthermore, when peak levels of seismicity are observed during wintertime icequake swarms, minimal power is observed in the swell band.

Infragravity waves are damped less effectively than swell by winter sea ice³⁴, and IG wave excitation of the RIS is detected by the array year-round (Figure 1.6b). We find that IG band power is poorly correlated with seismicity (Figure 1.6d). Most swarms occur on days that lack significant IG band power, and the largest IG events recorded at the array do not correspond to swarms of seismicity. Finally, the baseline level of IG power is nearly constant throughout the year and does not explain the seasonality observed in rift seismicity. On September 17, 2015, a tsunami generated by the M_w 8.3 Illapel, Chile earthquake reached the ice shelf, exciting horizontal displacements of about 7 cm at DR10⁵². The tsunami arrival is marked in Figure 1.6 and is particularly visible in the swell power time-series. However, the tsunami does not correspond to an increase in seismicity at WR4. This is consistent with previous findings that only rifts open to the ocean at the calving front propagate when a tsunami arrives⁴⁹, further suggesting that WR4 is not subject to significant wave-induced fracture.

1.7 CONCLUSIONS

Two primary environmental factors control rift seismicity at WR4. Diurnally, the timing of events is well-correlated with tidally-driven changes in ice shelf slope. Over longer time periods, the timing of events is well-correlated with air temperature, with peak levels of activity in the winter and swarms of events on particularly cold days. The combination of these two factors explains the tem-

poral patterns in seismicity that we observe here and demonstrates the high environmental sensitivity of rift deformation. Figure 1.7 illustrates that maximal icequake activity occurs during cold periods when the ice shelf is sloping downward toward the ice front. We note that while low levels of icequake activity are observed at low tide, no rift seismicity is observed above -10°C . From this analysis, we conclude that although thermal and tidal stresses are both important in generating shallow icequake activity, temperature exerts the most significant control on brittle deformation at WR₄.

The sequence of WR₄ icequakes differs from patterns of seismicity seen in propagating rifts, and the correspondence of the locations to an echelon shear zone features suggests that fracture may occur within the melange filling the rift. Swell and IG waves were not correlated with rift seismicity, though they may still exert some influence on rift behavior at RIS and at other ice shelves. The timing of rift activity at WR₄ appears to be primarily modulated by thermal and tidal stresses arising from fluctuations in air temperature and changes in ice shelf slope, and this work represents a novel demonstration of tidal influence on ice shelf processes far from the grounding line. On the Ross Ice Shelf, thermal and tidal stresses act in concert with ice shelf stresses, but not wave-induced stresses, to drive brittle deformation that may widen a major rift.

You got something to say?

Why don't you speak it out loud

Instead of living in your head?

The 1975

2

Holistic Analysis of Ice Shelf Fracture at Pine Island Glacier Ice Shelf

This work was first published in *Geophysical Research Letters*:

Olinger, S. D., Lipovsky, B. P., Denolle, M. A., & Crowell, B. W. (2022). Tracking the cracking: A holistic analysis of rapid ice shelf fracture using seismology, geodesy, and satellite imagery on the pine island glacier ice shelf, west antarctica. *Geophysical Research Letters*, 49(10), e2021GL097604.

ICE SHELF FRACTURE EXERTS a fundamental control on the stability of marine ice sheets and associated sea level fluctuations⁷². In particular, understanding the past, present, and future stability of the West Antarctic Ice Sheet (WAIS) remains one of the great challenges of modern glaciological research and is itself closely related to ice shelf fracturing processes⁷³. Fractures on ice shelves take on many forms including through-cutting rifts^{42,39,74}, smaller-scale basal and surface crevasses^{75,76}, hydraulic fracturing^{77,78}, and cliff failure⁷⁹. Despite decades of progress, understanding of ice shelf fracture remains significantly hindered by a lack of direct observation²⁵. A number of basic questions remain or have only partially been addressed: What forces are involved in ice shelf fracture? Is ice shelf fracture a fast and brittle or slow and ductile process? To what degree is water involved in fracture propagation? Does ice shelf fracture growth happen at a constant rate or in bursts, and what controls its timing?

All of these questions can be addressed using seismology. Because seismic waves carry information about the dynamics of fracture, numerous previous studies have leveraged such signals, referred to as icequakes, for this purpose^{80,81,82,83}. Seismic studies on ice shelves have shown that crevasse propagation is intermittent^{45,46} and have highlighted environmental forcings that would be difficult to ascertain using only remotely sensed observations^{57,84,85}.

Here, we use seismic recordings to quantify fracturing of Pine Island Glacier (PIG) Ice Shelf. PIG, part of the larger WAIS, contributes more to present day global sea level rise than any other glacier⁸⁶. Current ice mass loss at PIG is thought to be due to the retreat of the floating ice shelf²⁷ being caused by interactions between ocean forcing^{87,88} and fracturing processes⁸⁹.

We focus on icequakes that travel as flexural gravity waves to quantify fracturing of PIG Ice Shelf. Flexural gravity waves are a type of hybrid seismic-water wave⁹⁰ unique to floating structures such as ice shelves since both elasticity and buoyancy act as their restoring force⁹⁰. Flexural gravity waves are strongly dispersive⁹⁰, which can make waveform analysis difficult and necessitates careful modelling^{91,92,48}. Despite this challenge, flexural gravity waves are useful tools to study ice shelf processes

because, while direct body waves in ice shelves are often not observed at distances greater than a few ice thickness⁹³, flexural gravity waves are often observed to travel long distances from their exciting source⁹⁴.

Many sources generate flexural gravity waves on ice shelves including ocean swell⁹⁴, tsunamis⁵², and airplane landings⁹⁵.⁹⁵ appears to have been the first to propose that fracturing processes in ice shelves may act as seismic sources that generate flexural gravity waves.⁹⁵ considered water motion in a deforming rift and motion of detaching blocks from the ice front as two such sources. Here, we hypothesize that crevasse growth generates flexural gravity waves.

We begin our fracture analysis by describing a timeline of events with the use of satellite imagery. Next, we catalog flexural gravity waves on PIG to examine the relationship between crack growth, large-scale rift propagation, shear margin processes, and ice shelf acceleration. We then interrogate icequake source physics by modeling the ice shelf as a buoyantly supported beam, the simplest model that captures flexural gravity wave propagation^{91,92}. In our analysis, we model flexural gravity wave generation by a point load or bending moment applied during ice shelf crevasse growth to infer key source parameters of the recorded icequakes.

2.1 ANALYSIS OF SATELLITE IMAGERY AND POSITIONING

We track visible fracturing on PIG using images collected by the TerraSAR-X satellite⁹⁶ from 2012 to 2014. At the start of our study period in January 2012, the primary visible fractures are the rift, ~ 20 large cracks extending into the ice shelf from northern shear margin, and ~ 10 cracks extending into the ice shelf at the southern edge of the nascent iceberg (Figure 2.1a, left). By January 2013, the rift had propagated a few kilometers without significant widening, and two wing cracks⁹⁷ opened at the rift tip (Figure 2.1a, right). One of the cracks at the northern shear margin extended 7 km and connected to the rift between May 8 and May 11, 2012. The other northern shear margin cracks

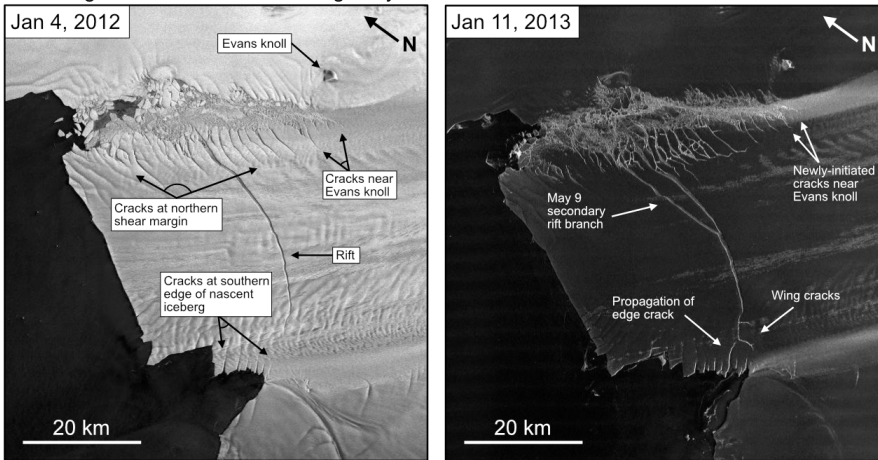
extended and widened, at least two new cracks initiated near Evans Knoll, and one of cracks at the southern edge of the nascent iceberg extended to within a kilometer of the rift tip.

During the first four months of 2013, the wing cracks near the rift tip extended and widened. In early July 2013, a block of ice calved along a wing crack at the southern edge of the nascent iceberg near the rift tip (Figure 2.1b). After this preliminary calving event, the only connection between the nascent iceberg and the ice shelf was a 2 km wide strip of ice between the ocean and a wing crack. Over the next few months, we observe significant widening of the rift, likely due to the iceberg beginning to drift away from the ice shelf. Iceberg B-31 calved in November 2013 (Figure 2.1c) when left lateral motion of the iceberg pried open a large wing crack near the rift tip until a strip of ice stabilizing the iceberg broke off, allowing Iceberg B-31 to drift into the sea. By the end of 2013, many fractures in the northern shear margin had extended and calved smaller icebergs, and several new fractures had initiated near Evans Knoll.

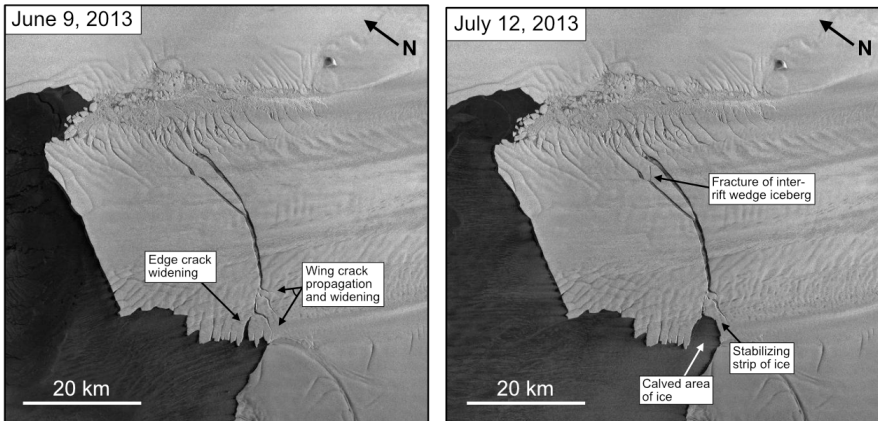
We processed Global Positioning System (GPS) speed timeseries derived from five continuous GPS stations in the region, BOAR and SOW₁₋₄ from 2012 to 2014. Each station was positioned kinematically in the International Terrestrial Reference Frame (ITRF) at a 30 s sample rate with GipsyX, using final Jet Propulsion Laboratory orbits. Ocean tidal loading and solid Earth tides were not removed from the derived displacement time series as these terms are needed to obtain the full glacial dynamics. After obtaining the 30 s ITRF solutions, we performed a 5 min weighted average using the inverse of the individual epoch uncertainties for data weights, and then rotated the XYZ displacements into local North, East, and up displacements.

We obtain ice speed from the processed GPS positions at the GPS station SOW₃ by calculating the total distance moved in each day of the deployment and differentiating with respect to time. The resulting ice speed curve contains some spike artifacts that arise from numerical differentiation, which we remove by linearly interpolating between the ice speed before and after the affected time period. Finally, we low pass filter the data to remove trends on time periods shorter than a week.

a. Changes in fracture extent during the year 2012



b. Preliminary calving along a wing crack near the rift tip



c. Calving of iceberg B-31

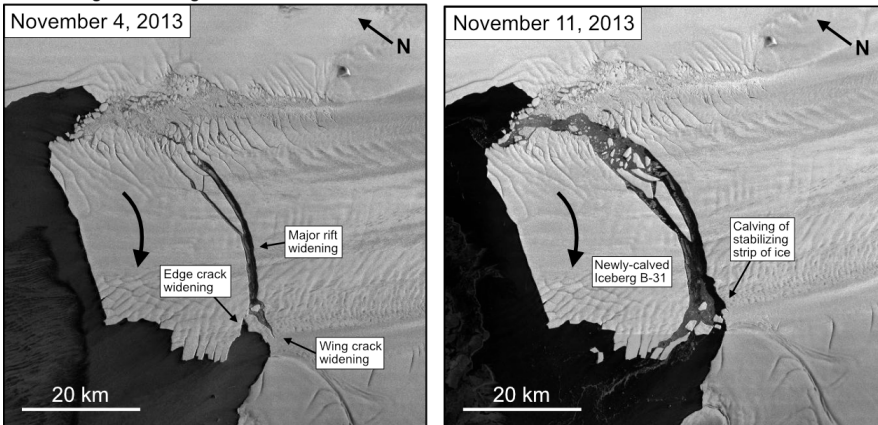


Figure 2.1: TerraSAR-X images showing an overview of fracture development at PIG from 2012 to 2014. Large arrow in panels c. and d. show sense of motion of the iceberg. See text for full discussion.

The GPS stations were co-located with seismometers (locations shown in Figure 2.2). Figure 2.3a plots the GPS-derived ice shelf speed. We find that ice speed at PIG decreases from 11.1 m/day in January 2012 to 10.8 m/day in April 2013. Then, ice speed drops to below 10.6 m/day for eight days in early May 2013. Following this rapid slowdown, ice speed begins to increase, reaching 10.9 m/day by the end of 2013. The GPS ice speed we compute here is consistent with a previous study utilizing the same dataset⁸⁷.

2.2 ANALYSIS OF SEISMOGRAMS

We examine seismic data from five sites on PIG⁹⁸. The instruments were deployed in January 2012 and retrieved in December 2013, providing two years of continuous data. The seismic stations were deployed in a cross shape with 5 km aperture at the center of the ice shelf (Figure 2.2). Each site consisted of a three component Nanometrics Trillium 120 Broadband seismometer and a Quanterra Q330 digitizer⁹⁹. Seismic data was sampled at 100 Hz, and we removed the instrumental response on the frequency band 0.001 Hz to 45 Hz.

In the seismic dataset, we observe events with an abrupt onset and with high frequencies that arrive before low frequencies. This type of dispersion is characteristic of flexural gravity waves. The observed dispersion (high frequency waves travel faster) is the opposite of typical surface waves in the solid Earth. In the latter case, low frequency waves travel faster because seismic wave speeds generally increase with depth.

2.2.1 ICEQUAKE DETECTION

To detect flexural gravity waves in the dataset, we design a two-stage detection scheme that identifies broadband, dispersive seismic events. First, we employ a short term average/long term average (STA/LTA) impulsivity detector. This method identifies high-amplitude impulsive events by com-

paring the mean amplitude of a short time window with the mean amplitude of a long time window¹⁰⁰. The detector is triggered when STA exceeds LTA by some threshold. STA/LTA threshold values are selected by tuning the algorithm to successfully detect high signal-to-noise ratio manually-identified events (see Table 2.1). We carry out STA/LTA on the vertical component of each station separately in two different frequency bands (0.01-1 Hz and 1-10 Hz). Selected waveforms satisfy the STA/LTA trigger criteria in both frequency bands on at least three out of the five stations. We refine the catalog and generate waveform templates by cross-correlating each preliminary event with a master event waveform and selecting the events with cross correlation coefficients exceeding 0.9. This selection procedure resulted in 57 template events.

Second, we perform a template matching technique based on cross-correlation to identify events that were similar to the events in the preliminary catalog¹⁰¹. To detect new events, each template event is cross correlated with all time windows in the dataset on two frequency bands (0.05-1 Hz and 1-10 Hz). We increase the lower frequency bound from 0.01 Hz to 0.05 Hz since many template events contained uninterpretable noise at frequencies below 0.05 Hz. The detector is triggered when the cross-correlation coefficient between a template event waveform and the given time window exceeds a threshold. The threshold value is selected so that the algorithm successfully detects the other known events of the preliminary catalog (see Table 2.1). Detected waveforms satisfy the trigger criteria on at least three out of the five stations in both frequency bands. We carry out this procedure for each template and removed redundant detections to yield the final catalog.

We detect 22,119 seismic events using the two-band template matching scheme. The detected events have a typical duration of around 50 s and an average peak vertical velocity of approximately $1 \cdot 10^{-5}$ m/s. Event waveforms vary in shape, indicating varied sources and propagation paths. Inspection of the preliminary catalog reveals two main families of events: one with clear high-frequency-first dispersion and one which is dominantly monochromatic.

Table 2.1: Parameters for building the event catalog.

Parameter	Low Frequency Band	High Frequency Band
STA/LTA band	0.01-1 Hz	1-10 Hz
Short window (ST) length	10 s	10 s
Long window (LT) length	300 s	300 s
Trigger STA/LTA threshold	8 s	20 s
Template matching band	0.05-1 Hz	1-10 Hz
Trigger cross correlation threshold	0.3	0.2
Minimum number of stations for a detection	3	3

2.2.2 WAVEFORM CLUSTERING

To isolate flexural gravity waves, we undertake waveform clustering using a K-Shape algorithm¹⁰² modified to operate on multi-component seismic data. K-shape is designed specifically to cluster time series data. Instead of calculating the Euclidean distance between potential cluster centers and observations, K-shape calculates distances using the maximum normalized cross correlation coefficient between two time series. We adapt the K-shape algorithm for three component seismic data by independently computing the cross-correlation time series between the three separate seismic channels (vertical, East, and North). We then sum these three cross-correlation time series and calculate the distance metric as the maximum value of this summed cross correlation time series.

We use the K-shape algorithm to divide the catalog into 2, 3, \dots , 20 clusters. However, beyond two clusters, the differences between waveforms in each cluster become progressively less clear, and an analysis of the average distance from waveforms to their cluster center does not show significant improvement for larger numbers of clusters. We thus use the K-shape algorithm to divide the catalog into two distinct clusters, which differ based on waveform dispersion. The first cluster contains 8,184 dispersive events. The second cluster contains 13,935 monochromatic events that do not exhibit dispersion within the chosen frequency band. This difference suggests that the two types of waveforms may have been generated by different source processes. Since we are specifically inter-

ested in dispersive flexural gravity wave signals, we restrict the remaining analysis to the dispersive cluster. Visual analysis of the clustered catalog demonstrates the efficacy of our approach in isolating flexural gravity waves (Figure 2.3). Our final catalog contains 8,184 likely flexural gravity wave events, which we refer to as icequakes in the rest of the text.

2.2.3 ICEQUAKE LOCATION

We next determine locations for all icequakes in our final catalog. Given the poor distribution of the stations with respect to fracture locations, we employ single-station approaches to locating icequakes. We compute epicentral back-azimuths by analyzing the polarization direction of recorded horizontal waves⁸⁵. We apply principle component analysis (PCA) to the horizontal component seismograms to retrieve polarization directions. The polarization provides a 180 degree ambiguity, so we find the direction of propagation based on which station recorded the first arrival.

We obtain the relative first arrival time of each event through phase lags measurements. We cross-correlate each respective component waveform between each seismic station. We choose a window length of 500 s around the first arrival. The trace that requires the largest shift forward in time to align with the other traces is taken to be the station of first arrival. In most cases, the first arrivals obtained independently using each component are in agreement for at least two components out of three. However, if all three components produce different stations of first arrival, a back-azimuth is not calculated and the event is disregarded.

Next, we ensure that the polarization is extracted over a high signal to noise ratio event as against noise. We slide through the event waveform in 10 s windows with a step size of five seconds. For each 10 s time window, we check if the average amplitude of that window exceeds the average amplitude of the entire 500 s event window. For time windows with sufficiently large amplitude, principal component analysis (PCA) is performed on the HHE (East) and HHN (North) traces from each station to retrieve the PCA components. The PCA first component is a vector whose direction

explains the largest contribution of the data variance. It is equivalent to the eigenvector of the data covariance matrix that has the largest eigenvalue.

For waves polarized in the direction of propagation, the PCA first component vector corresponds to one of the two possible propagation directions separated by 180 degrees. Using the PCA first component vector and the geometry of the array, we compute the predicted stations of first arrival corresponding to both possible propagation directions. If the station of first arrival is in the direction of the PCA back-azimuth, the PCA first component's sign is preserved. If the station of first arrival is in the opposite direction (PCA azimuth+180 degree), we add 180 degrees to the PCA first component azimuth. This ensures that the PCA first component vector points in the direction from which incoming waves arrived.

We try three methods of computing the predicted station of first arrival corresponding to both possible propagation directions. In the first method, we compare both possible phase back-azimuths to the back-azimuths of each station with respect to the mean station location, or array centroid. The stations that are radially closest to each possible back-azimuth are predicted to be the two possible first arrivals. The sign of the PCA first component vector is then adjusted to match the propagation direction whose predicted first arrival agree with the observed first arrival. Phases for which neither predicted first arrival agreed with the observed first arrival are discarded. In the second method, we divide the array into two sectors along a line through the array centroid orthogonal to the PCA first component vector. The sign of the PCA first component vector is then adjusted to match the propagation direction corresponding to the sector containing the observed first arrival. No phases are discarded. In the third method, we compute the distance vector from the array centroid to each station. For incoming plane waves, the station farthest from the array centroid in the direction of propagation records the first arrival. The stations whose distance vectors have the largest component oriented in each possible propagation directions are predicted to be the two possible first arrivals. The sign of the PCA first component vector is then adjusted to match the propagation direction

whose predicted first arrival agree with the observed first arrival. Phases for which neither predicted first arrival agreed with the observed first arrival are discarded. All three methods gave relatively consistent results.

Next, we sum the PCA first component vectors across each station to obtain an average vector whose norm indicates the level of agreement between propagation directions calculated at each station. Finally, we take the arctangent of the quotient of the two elements of the PCA component vector to retrieve a back-azimuth. Because this procedure is repeated for each 10 s time window in the event, the result for each individual event is a distribution of back-azimuths calculated for each time window within that event.

To obtain a single back-azimuth for each event, we take the average of the back-azimuths calculated using each time window in the data. We use the mean of circular quantities, with the back-azimuth from each time window weighted by the norm of the summed PCA components across the array for that window. This means that time windows with poor agreement between stations are downweighted when taking the average back-azimuth. The weighted mean of circular quantities is expressed below for the back-azimuth distribution $\theta_1, \dots, \theta_n$ with PCA norms w_1, \dots, w_n of a single event with n time windows:

$$\bar{\theta} = \text{atan2} \left(\frac{1}{n} \sum_{j=1}^n w_j \sin(\theta_j), \frac{1}{n} \sum_{j=1}^n w_j \cos(\theta_j) \right)$$

Uncertainties for icequake back-azimuths were computed using the weighted standard deviation of circular quantities for each event. The weighted standard deviation of circular quantities is expressed below for the back-azimuth distribution $\theta_1, \dots, \theta_n$ with PCA norms w_1, \dots, w_n of a single event with n time windows:

$$\sigma = \sqrt{\left(\frac{1}{n} \sum_{j=1}^n w_j \sin(\theta_j)\right)^2 + \left(\frac{1}{n} \sum_{j=1}^n w_j \cos(\theta_j)\right)^2}$$

The mean back-azimuthal uncertainty for rift-tip icequakes was 26.16° . The mean back-azimuthal uncertainty for rift/margin icequakes was 17.26° . The mean back-azimuthal uncertainty for shear margin icequakes was 20.13° .

We locate all of the 8,184 icequakes to one of three distinct source regions: the rift tip, the body of the rift and nearby shear margin (“rift/margin”), and the northeast shear margin near Evan’s knoll (“shear margin”), which are depicted in Figure 2.2. These spatial groups correspond to 22%, 29%, and 40% of the catalog, respectively, with 9% of events having indeterminate locations. Figure 2.2 shows the back-azimuthal histograms of the three groups.

The slight mislocation of the rift-tip icequake back-azimuths apparent in Figure 2 is explained in a few ways. First, imagery suggests that much of the rift-tip fracture in 2013 occurred at the large wing extending south of the rift axis. The distribution of rift-tip seismic event back-azimuths points just south of this crack by $\sim 1^\circ$. We note that the LANDSAT image displayed in Figure 2 is from October 12, 2013, about a month before the large swarm of rift-tip seismicity in November 2013. Because the wing crack continued to advance and widen in the month after the LANDSAT image was captured, we expect fracturing and seismicity to have occurred in front of the wing crack tip’s position in Figure 2. Second, the correspondence in time between the large swarm of rift-tip icequakes in November 2013 and visible fracture evolution at the rift-tip wing crack suggests that the recorded icequakes were generated by that fracture. Third, seismicity in front of a rift’s visible extent was observed at the Amery Ice Shelf by Bassis et al. (2007) and may indicate that the wing crack was more advanced at depth than at the surface, explaining events whose back-azimuths point just in front of the crack. Finally, no other areas consistent with distribution of rift-tip icequake back-azimuths contain any visible fracture opening or growth, suggesting that the large amount of

fracture evolution at the rift tip observed in imagery is the most likely source of the recorded icequakes.

2.3 RELATIONSHIPS BETWEEN ICEQUAKES AND ICE SHELF BEHAVIOR

2.3.1 RIFT TIP

The rift-tip icequakes are coincident in space and time with several fracturing processes including rift propagation, wing cracking, small scale calving within the rift, and calving along the southern edge of the nascent iceberg. Rift tip events occurred more frequently in 2013 than in 2012 (Figure 2.3b). The mean seismicity rate was 9.4 icequakes/week in 2012 and 25.6 icequakes/week in 2013. 19 weeks of 2013 equaled or exceeded the maximum 2012 seismicity rate of 29 icequakes/week. Weekly icequake counts increased past the peak level seen in 2012 on May 21, 2013 and remain elevated until the end of the deployment. This period of elevated rift tip seismicity corresponds to the phase of significant wing crack growth and rift widening observed in imagery. Rift tip icequakes appear located ~ 15 degrees south of the rift tip's position in LANDSAT imagery from October 12, 2013 (Figure 2.2). However, when Iceberg B-31 calved in November 2013, the wing crack extending south of the rift had propagated to a location consistent with the peak in the back-azimuthal distribution of rift tip icequakes (Figure 2.1c, left).

Peak levels of rift-tip seismicity were observed during the calving of Iceberg B-31 in the week of November 5, 2013. That week had 115 rift-tip events, the highest event count of any week across all three source regions. Furthermore, elevated rift-tip icequake activity in 2013 corresponds to a period of accelerating ice velocities (Figure 2.3a). While rift-tip fracture may be more directly related to strain rate in a viscous regime and strain in an elastic regime, we simply note that ice speed reflects the underlying stress state of the ice shelf. The correspondence in time between elevated rift-tip seismicity rates and increasing ice velocities therefore suggests that rift propagation is sensitive to the

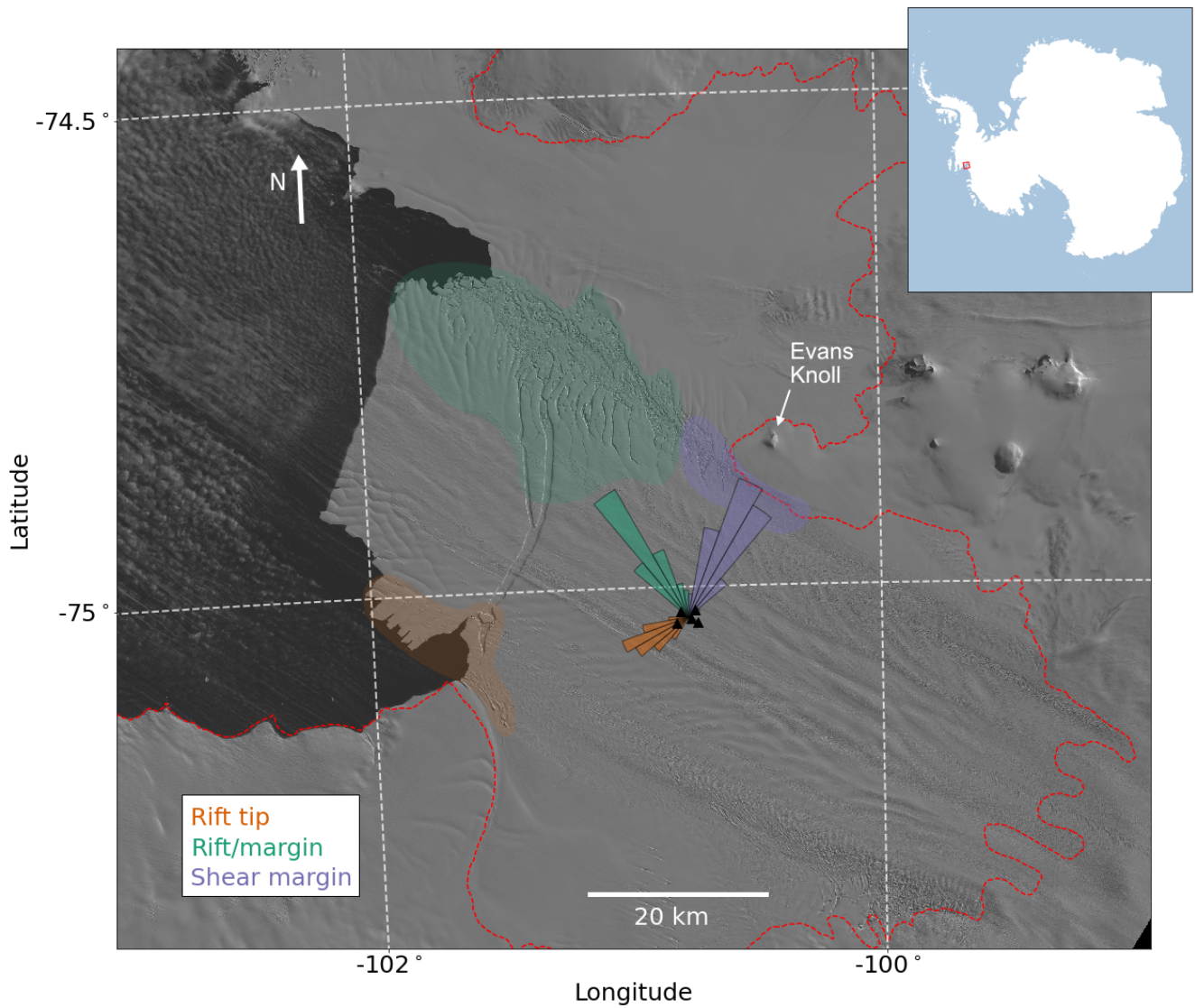


Figure 2.2: Back-azimuthal histogram showing locations of cataloged icequake. Rift-tip event back-azimuths are plotted as orange rays. Rift/margin event back-azimuths are plotted as green rays. Shear-margin event back-azimuths are plotted as purple rays. Likely source regions are shown by colored polygons. PIG array seismic and GPS stations are plotted as black triangles. Approximate grounding line position is shown by the red dashed line¹⁰³. Background LANDSAT imagery is from October 2013 (courtesy of the United States Geological Survey).

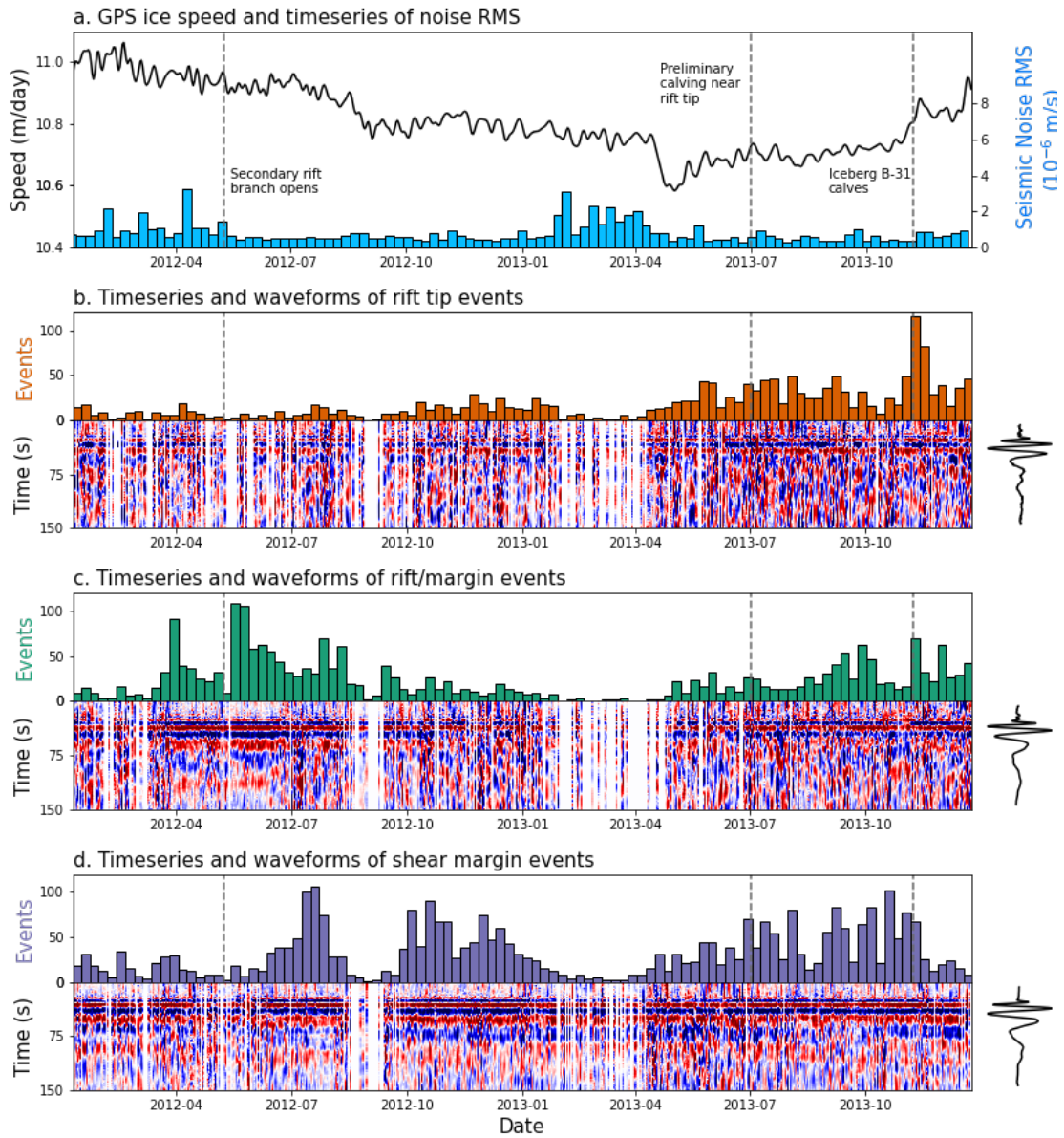


Figure 2.3: Timing and waveforms of cataloged icequake. (a) GPS-derived ice velocity is shown by the black line, and average seismic noise is shown by blue bars. Noise is highest in the Antarctic summer, when minimal sea ice is present to attenuate ocean-generated noise, reducing detectability in January, February, and March. (b) Rift-tip events. Weekly timeseries of rift tip event times is shown by orange bars. Daily vertical (HHZ) waveform stacks of detected rift tip events are plotted beneath. Overall rift-tip event stack is shown to the right. (c) Same as (b) for rift/margin events, color-coded in green. (d) Same as (b) for shear-margin events, color-coded in purple.

underlying stress state of the ice shelf. In addition, rift tip fracture may be enhanced by localized ice shelf thinning and melt within the rift.⁸⁷ hypothesize that the overall pattern of ice velocities at PIG in 2013 tracks a time-lagged response to ocean melting, and localized melt has been proposed as a primary driver of rifting at PIG^{104,105}. The observed connection in time between rift tip fracture and accelerated ice velocities demonstrates that rift growth and PIG is sensitive to changes in ice dynamics, localized melt, or a combination of both. At the present time, however, we are unable to confirm whether local or more distant melt-related feedbacks are responsible for the observed fracturing.

2.3.2 RIFT/MARGIN

The rift/margin icequakes are coincident in space and time with the growth of ~ 20 rifts formed in the northwest shear zone, as well as smaller-scale fractures and widening of the main rift itself. Rift/margin icequakes occurred more frequently in 2012 than in 2013. The mean seismicity rate was 27.7 icequakes/week in 2012 and 19.3 icequakes/week in 2013. Four weeks of 2012 equaled or exceeded the maximum 2013 seismicity rate of 70 icequakes/week. The timing of icequakes in the rift/margin group is independent of ice speed. Peak levels of rift/margin seismicity were observed during the week of May 15, 2012, which contained 109 rift/margin icequakes. Rift/margin icequakes reach peak seismicity rates in the weeks following the opening of the secondary rift branch in May 2012, suggesting that the crack opening caused aftershock-like seismicity and/or destabilized the margin, enhancing the growth of nearby fractures.

2.3.3 SHEAR MARGIN

The shear-margin icequakes are coincident in space and time with the initiation of new cracks and growth of extant cracks near Evans Knoll. This area marks the transition from a primarily intact

shear margin upstream of Evans Knoll to a highly fractured shear margin downstream of Evans Knoll. Imagery shows that multiple fractures longer than 1 km were initiated in this area during 2012 and 2013 (Figure 2.1). Shear-margin icequakes occurred at an approximately equal rate in 2012 and 2013. The mean seismicity rate was 31.9 icequakes/week in 2012 and 32.2 icequakes/week in 2013. Peak levels of shear margin seismicity were observed during the week of July 17, 2012, which contained 107 shear-margin icequakes. Shear-margin icequakes do not exhibit any prominent temporal trends and appear independent of ice velocity. The shear margin experiences the highest overall level of seismic activity, suggesting that the transition point from intact to fractured ice near Evans Knoll experiences higher stress concentrations than either the rift tip or the rift/margin regions, consistent with rift modeling⁷⁴.

2.4 FLEXURAL GRAVITY WAVE MODELING

We next estimate the distribution of forces that gives rise to the observed seismograms. We do this by removing wave propagation effects from the observed seismograms using a numerically computed Green's function. Our catalog was designed to represent icequakes that mostly consist of flexural gravity waves. We therefore model the vertical seismograms using the simplest model that gives rise to flexural gravity waves, the dynamic floating beam equation^{90,106},

$$\rho_i b_i \frac{\partial^2 w}{\partial t^2} + D \frac{\partial^4 w}{\partial x^4} + \rho_w g w + \rho_w \frac{\partial \varphi}{\partial t} = P, \quad (2.1)$$

where $D \equiv EI = Eb_i^3/[12(1 - \nu^2)]$ is the flexural rigidity with second moment of area $I = \int_{-b_i/2}^{b_i/2} z^2 dz$, E is the Young's modulus of ice, ν is the Poisson's ratio of ice, t is time, x is horizontal position, g is gravitational acceleration constant, b_i is the ice thickness, ρ_i is the density of ice, ρ_w is the density of water, w is the vertical displacement of the beam, φ is the ocean surface velocity potential, and P is an applied point load. From left to right, the terms in Equation 2.1 represent inertia,

flexure of the ice shelf, buoyancy, and ocean surface waves generated at the ice-water interface. We initially use a locally-averaged ice thickness of $h_i = 400 \text{ m}$ ¹⁰⁷ and a water depth of $h_w = 590 \text{ m}$ ¹⁰⁸.

We model icequake sources as either an applied point load or point bending moment. When a basal crevasse opens and fills with water, the downward-acting ice overburden stress at the top of the crevasse is greater in magnitude than the upward-acting buoyancy stress exerted by water filling the crevasse. This applies a downward point load to the ice shelf. In addition, the horizontal ice overburden stress along the walls of the crevasse is greater in magnitude than the horizontal buoyancy stress exerted by the water filling the crevasse. The difference in magnitude between these two stresses decreases with depth such that the walls of a crevasse are subject to stress gradient. This applies a bending moment to the ice shelf. These two mechanisms may act in concert and simultaneously apply a moment and point load to the ice shelf. We choose not to pursue such hybrid sources at the present time because the simplicity of our model –specifically the assumptions of uniform ice thickness and two-dimensional geometry– suggests that additional source complexity is not warranted prior to improvements in these other areas.

We obtain the Green’s function of the floating beam equation as the impulse response of the mechanical system to a point load (force per unit length) source. Rewriting Equation 2.1 using the linear operator \mathcal{A} as $\mathcal{A}w = P$, the Green’s function equation can then be written as $\mathcal{A}G = \delta(x)\delta(t)$. Below, we derive a frequency-wavenumber solution for G that we are able to analytically invert in the time domain and numerically invert in the frequency domain. We then derive G_m , the vertical displacement response to a point moment source.

2.4.1 ANALYTIC SOLUTION FOR OCEAN SURFACE WAVES

We examine the water velocity potential function φ and relate it to the vertical ice shelf velocity w . We first solve the ocean surface wave equation for a body of water with infinite length and finite

depth:

$$\frac{\partial^2 \varphi}{\partial x^2} + \frac{\partial^2 \varphi}{\partial y^2} = 0 \quad (2.2)$$

over the interval $-\infty < x < \infty, -b_w < y < 0$. We enforce zero velocity at the ocean floor and couple vertical velocity to the rate of beam deflection at the ocean surface:

$$\frac{\partial \varphi}{\partial y} \Big|_{y=-b_w} = 0 \quad \frac{\partial \varphi}{\partial y} \Big|_{y=0} = \frac{\partial w}{\partial t} \quad (2.3)$$

We enforce the Sommerfeld radiation condition:

$$\varphi \Big|_{x \rightarrow -\infty} = \frac{\partial \varphi}{\partial x} \Big|_{x \rightarrow -\infty} = 0 \quad \varphi \Big|_{x \rightarrow \infty} = \frac{\partial \varphi}{\partial x} \Big|_{x \rightarrow \infty} = 0 \quad (2.4)$$

We employ the Fourier Transform, written for an arbitrary function $f(x)$ as

$$\bar{f}(k) = \int_{-\infty}^{\infty} f(x) e^{-i\xi x} dx$$

Applying the Fourier Transform in x to each term of Equation 2.2 yields:

$$\int_{-\infty}^{\infty} \frac{\partial^2 \varphi}{\partial x^2} e^{-i\xi x} dx + \frac{\partial^2 \bar{\varphi}}{\partial y^2} = 0$$

Evaluating the integral term:

$$e^{-i\xi x} \frac{\partial \varphi}{\partial x} \Big|_{-\infty}^{\infty} + i\xi e^{-i\xi x} \varphi \Big|_{-\infty}^{\infty} - \xi^2 \bar{\varphi} + \frac{\partial^2 \bar{\varphi}}{\partial y^2} = 0$$

We then apply the radiation condition (Equation 2.4) to eliminate the first two terms, resulting in an ordinary differential equation of $\bar{\varphi}$:

$$-\xi^2 \bar{\varphi} + \frac{\partial^2 \bar{\varphi}}{\partial y^2} = 0$$

By applying the vertical boundary conditions (Equation 2.3), we obtain the time-wavenumber domain solution that satisfies the governing equation and boundary conditions:

$$\bar{\varphi} = \frac{\partial \bar{w}}{\partial t} \left(\frac{\cosh(\xi(b_w + y))}{\xi \sinh(b_w \xi)} \right)$$

We note that φ is a linear function of w , therefore permitting us to write the floating beam equation using the linear operator \mathcal{A} .

2.4.2 ANALYTIC SOLUTION FOR BUOYANT ICE SHELF FLEXURE

We write the Green's function formulation of Equation 2.1:

$$\rho_i h_i \frac{\partial^2 G}{\partial t^2} + D \frac{\partial^4 G}{\partial x^4} + \rho_w g G + \rho_w \frac{\partial \varphi}{\partial t} = \delta(x) \delta(t) \quad (2.5)$$

where G is the Green's function, $\delta(x)$ is Dirac delta function in space, and $\delta(t)$ is the Dirac delta function in time. As before, we apply the Fourier Transform in space to each term. Next, we apply the Laplace transform, defined as,

$$g^*(s) = \int_0^{\infty} g(t) e^{-st} dt$$

Applying both the Fourier and Laplace Transforms to Equation 2.5 yields:

$$\rho_i h_i s^2 \bar{G}^* + D \xi^4 \bar{G}^* + \rho_w g \bar{G}^* + \rho_w \gamma s^2 \bar{G}^* = 1$$

We can then solve for \bar{G}^* algebraically:

$$\bar{G}^* = \frac{1}{\frac{\rho_i b_i + \rho_w \gamma}{D_\zeta^k + \rho_w g} + s^2} \quad (2.6)$$

Finally, we analytically compute the inverse Laplace transform of Equation 2.6 to obtain the Fourier-transformed Green's function,

$$\bar{G}(k, t) = \frac{\sin\left(t \sqrt{\frac{D_\zeta^k + \rho_w g}{\rho_i b_i + \rho_w \gamma}}\right)}{\sqrt{\rho_i b_i + \rho_w \gamma} \sqrt{D_\zeta^k + \rho_w g}}$$

In practice, we numerically calculate \bar{G} for a range of times and wavenumbers that define the temporal and spatial domain of the model run. Once \bar{G} is calculated for each element of a vector of times and a vector of wavenumbers, the IFFT (inverse fast Fourier transform) is taken to numerically retrieve the Green's function $G(x, t)$ of the ice shelf for an applied unit point force.

To retrieve the impulse response to a point bending moment source, we note that an applied bending moment is equivalent to a pair of infinitesimally-spaced point loads with opposite signs:

$$G_m(x, t) = [G(x, t) - G(x + \Delta x, t)]_{\Delta x \rightarrow 0}$$

$$G(x, t) = \Delta x \left[\frac{G(x, t) - G(x + \Delta x, t)}{\Delta x} \right]_{\Delta x \rightarrow 0}$$

$$G(x, t) = \frac{dG(x, t)}{dx}$$

To obtain $G_m(x, t)$, we numerically take the spatial derivative of the point load Green's function $G(x, t)$.

2.4.3 DECONVOLUTION PROCEDURE

We deconvolve G and G_m from waveform stacks to estimate the source load or moment distribution of events in each spatial group. We calculate source load through the deconvolution,

$$P_{\text{estimated}}(t) = \mathcal{F}^{-1} \left[\frac{\hat{w}(\omega)_{\text{observed}}}{\hat{G}(x_0, \omega)} \right],$$

where hats denote Fourier-transformed quantities, \mathcal{F}^{-1} is the inverse Fourier transform, $w_{\text{observed}}(t)$ is a linear stack of observed displacement seismograms, $P_{\text{estimated}}(t)$ is an estimated source load distribution, and x_0 is the station epicentral distance. We obtain $w_{\text{observed}}(t)$ for each spatial group by aligning each waveform in the group with respect to a master event using cross correlation and taking the average waveform. Master events were selecting by finding the event from each spatial group that was best-correlated with the overall centroid of the dispersive cluster. We choose x_0 corresponding to the average distance to each spatial group: for the rift tip, $x_0 = 25$ km; for rift/margin, $x_0 = 25$ km; for margin icequakes, $x_0 = 17.5$ km. We alternatively consider a bending moment source through the relationship,

$$M_{\text{estimated}}(t) = \mathcal{F}^{-1} \left[\frac{w(\omega)_{\text{observed}}}{G_m(x_0, \omega)} \right]$$

2.4.4 ESTIMATING VERTICAL FRACTURE EXTENT

We estimate the vertical extent of fracture using the magnitude of source time functions retrieved by deconvolution. The point load applied during vertical crack growth arises from the difference in ice overburden stress above the crack and buoyancy stress exerted by the water that fills the crack.

Therefore, we write the following expression and substitute in the each stress:

$$P = \sigma_{\text{overburden}} - \sigma_{\text{buoyancy}}$$

$$P = \rho_i g (h_i - \Delta z_c) - \rho_w g (z_w - \Delta z_c)$$

where P is the applied point load, ρ_i is the density of ice, ρ_w is the density of water, h_i is the ice shelf thickness, Δz_c is the change in vertical position of the crack tip, and z_w is the position of the water line.

Substituting the expression for the water line position $z_w = \frac{\rho_i}{\rho_w} h_i$ and simplifying gives:

$$P = g \Delta z_c (\rho_i - \rho_w)$$

Finally, we write:

$$\Delta z_c = \frac{P}{g(\rho_i - \rho_w)}$$

2.4.5 RESULTS OF DECONVOLUTION

Figure 2.4 shows our deconvolution result for the rift-tip icequakes, illustrating that a given vertical displacement seismogram may equivalently be represented as a point moment (Figure 2.4a and b) or a point load (Figure 2.4c and d). The equivalent analysis for the other two groups of events are shown in Figure 2.5 and Figure 2.6.

We examine the sensitivity of our deconvolution to the assumed value for the ice thickness by varying the ice thickness between 300 and 500 m (Figures 4.1-4.3). For the rift-tip group, we find source durations ranging from 30.48 to 50.00 s and amplitudes ranging from 2.69 to 6.90 MPa·m (point moment) and 3.83 to 8.62 kPa (point load). For the rift/margin group, we find source durations ranging from 19.52 to 48.57 s and amplitudes ranging from 3.82 to 12.55 MPa·m (point moment) and from 5.05 to 14.02 kPa (point load). Finally, for the shear-margin group, we find source

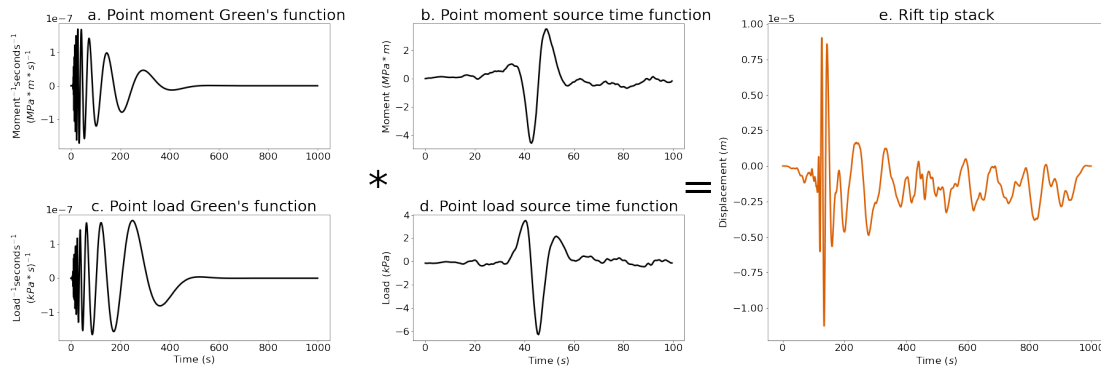


Figure 2.4: Green's functions and source time functions for rift tip events. (a) Theoretical Green's function for a point moment source located at a distance of 25 km, which is approximately the distance from PIG seismic array to the rift tip. (b) Source time function retrieved by deconvolving the point moment Green's function from the stack of rift tip vertical displacement waveforms. (c) Theoretical Green's function for a point load source located at a distance of 25 km. (d) Source time function retrieved by deconvolving the point load Green's function from the stack of rift tip vertical displacement waveforms. (e) Stack of rift tip vertical displacement waveforms obtained by aligning waveforms to a master event and taking the mean waveform on the frequency band 0.01-1 Hz.

durations ranging from 27.14 to 36.67 s and amplitudes ranging from 5.60 to 14.89 MPa·m (point moment) and from 8.04 to 12.97 kPa (point load).

2.5 DISCUSSION OF ICEQUAKE SOURCE PHYSICS

How large were the cracks that generated the recorded flexural gravity waves? We estimate the amount of vertical crack opening for each spatial group using the point load source amplitudes for ice thickness varying between 300 and 500 m. Rift tip point load amplitudes correspond to 4.3 to 9.8 m of vertical crevasse opening. Rift/margin point load amplitudes correspond to 5.7 to 15.9 m of vertical crevasse opening. Shear-margin point load amplitudes correspond to 9.1 to 14.7 m of vertical crevasse opening. This suggests that the large-scale fracture opening and rift propagation observed in imagery (Figure 2.1) was the result of many discrete crack opening events that each spanned only about 1 % of the ice thickness, not the result of full-thickness crack opening.⁴⁵ and ⁴⁶ observed episodic rift seismicity on the Amery Ice Shelf and proposed that rifts might propagate due

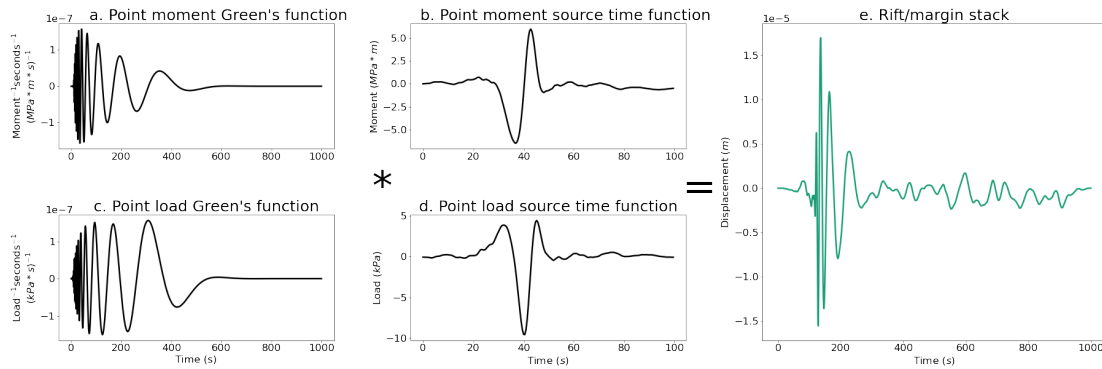


Figure 2.5: Green's functions and source time functions for rift/margin events. (a) Theoretical Green's function for a bending moment source located at a distance of 30 km, which is approximately the distance from PIG seismic array to the rift/margin area. (b) Source time function retrieved by deconvolving the moment Green's function from the stack of rift/margin vertical displacement waveforms. (c) Theoretical Green's function for a point load source located at a distance of 30 km, which is approximately the distance from PIG seismic array to the rift/margin area. (d) Source time function retrieved by deconvolving the point load Green's function from the stack of rift/margin vertical displacement waveforms. (e) Stack of rift/margin vertical displacement waveforms obtained by aligning waveforms to a master event and taking the mean waveform on the frequency band 0.01-1 Hz.

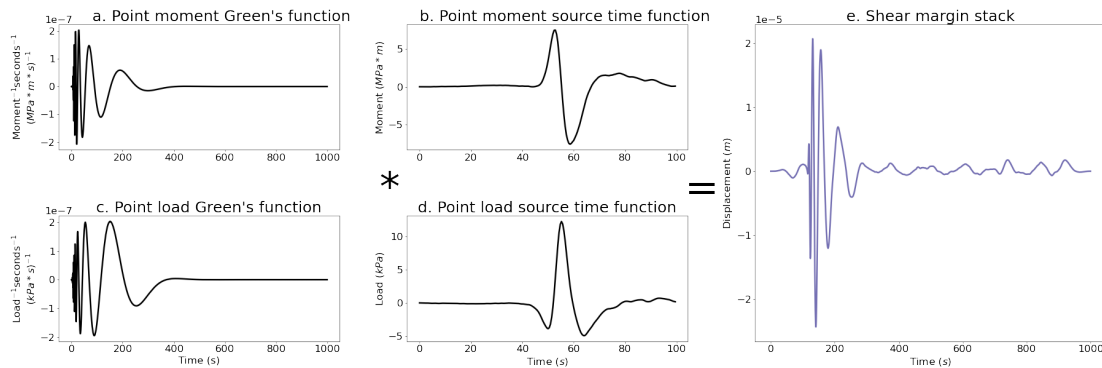


Figure 2.6: Green's functions and source time functions for shear margin events. (a) Theoretical Green's function for a bending moment source located at a distance of 17.5 km, which is approximately the distance from PIG seismic array to the northeast shear margin near Evans Knoll. (b) Source time function retrieved by deconvolving the moment Green's function from the stack of shear margin vertical displacement waveforms. (c) Theoretical Green's function for a point load source located at a distance of 17.5 km, which is approximately the distance from PIG seismic array to the shear margin. (d) Source time function retrieved by deconvolving the point load Green's function from the stack of shear margin vertical displacement waveforms. (e) Stack of shear margin vertical displacement waveforms obtained by aligning waveforms to a master event and taking the mean waveform on the frequency band 0.01-1 Hz.

to the coalescence of smaller cracks. Our findings support the hypothesis that crack coalescence can act as a mechanism of rifting.

Estimated source time series for moment and point load exhibit one or several pulses of activity followed by a return to zero (Figure 2.4). Source time functions derived from body waves in an elastic medium result in estimates of moment rate¹⁰⁹ Equation 4.32. Here, however, our deconvolution is sensitive not to the rate of change of point load or moment, but instead to a point load and moment. This complicates the interpretation of the estimated source time series because it suggests that the icequakes represent the application and subsequent removal of some point load or moment. This physically counterintuitive situation motivates an examination of the sensitivity of our deconvolution to static offsets. We therefore calculate synthetic seismograms forced by a step in moment or point load (Figures A.4-A.6). We find that in some cases the step function provides an acceptable fit to the observations. We therefore are unable to infer whether the observed flexural gravity waves were generated by a pulse-like or step-like source.

The timescale of the source process, however, is constrained independent of the exact force distribution assumed in the deconvolution. Our source analysis implies that the recorded flexural gravity waves were generated by fracturing process with approximately 20-50 s duration. At this timescale, the observed waves must have been generated by brittle fracture, not by viscous deformation. This 20-50 s timescale is extremely slow compared, for example, to tectonic earthquakes, where earthquake duration scales like $10^{M/2}$ with earthquake moment M and 20 s duration is associated with a $M = 7$ earthquake¹¹⁰.

What process sets the duration of the observed icequakes? The above scaling for tectonic earthquakes is based on the reasoning that the duration is set by the time required for a shear crack to propagate across a fault of length L at a rate that tends towards inertial velocities (either the shear or dilatational wave speed v_s or v_p)¹¹¹. In our system, however, we expect that water plays a limiting role in the speed of fracture propagation that may not be present in tectonic earthquakes. The prop-

agation of fluid filled basal crevasses is expected to occur at the crack wave speed¹¹². The crack wave speed is much slower than the inertial velocities and could plausibly be in the range of 1-100 m/s for basal crevasses in ice shelves. These velocities would suggest source length scales on the order of meters to hundreds of meters. A second plausible explanation is that long durations may be explained by the coalescence of many smaller individual fractures that open successively. And yet another explanation is that there could be significant horizontal propagation which is not captured in our model. We expect that more detailed near-source observations would be able to distinguish between these possible scenarios.

2.6 CONCLUSIONS

We detect and locate icequakes that propagate as flexural gravity waves on the Pine Island Glacier ice shelf from 2012 to 2014. When compared to satellite imagery, the back-azimuthal distribution of the detected events suggests that the icequakes were generated by fractures at the tip of a large rift and in two distinct portions of the northern shear margin. Most of the events were generated at the shear margin near Evans Knoll, in agreement with imagery that suggests significant fracture initiation. Increased fracturing at the rift tip is associated with increased ice speed and elevated basal melting in 2013⁸⁷. We attribute this relationship to changes in the stress state of the ice shelf or to melt-driven thinning that elevated rift tip stress concentrations. We use a simple model of flexural gravity waves to constrain the source of the recorded waves. We find that the observed waves have a source duration between 20-50 s. This timescale implies that a brittle fracture process generated the waves. Our analysis therefore confirms the role of brittle processes in the long-term evolution of marine ice sheets.

Here's a crown I found of laurel leaves

Queen of all the things in sunbeams

Anoint me

Baths

3

Ocean coupling controls the fastest observed ice shelf rift propagation event

This work is currently in review at *Science Advances*:

Olinger, S. D., Lipovsky, B. P., & Denolle, M. A. (2023). Ocean coupling controls the fastest observed ice shelf rift propagation event. Submitted to *Science Advances*.

THE POSSIBILITY OF RAPID ICE MASS LOSS from the West Antarctic ice sheet has remained contentious for over thirty years¹⁵. The seminal collapse of the Larsen B ice shelf provided incontrovertible evidence linking ice shelf fracturing to rapid ice mass loss^{8,9}, with more recent work emphasizing spatial variability in ice shelf vulnerability^{113,114,115} and pervasive damage^{116,117}. In contrast to such progress in understanding large-scale dynamics, the detailed nature of the fracturing processes that may (or may not) contribute to rapid ice mass loss has remained controversial. Significant research foci include hydrofracture, a process which is clearly conducive to ice shelf collapse^{78,22,115}, and the marine ice-cliff instability¹¹⁸, a process by which rapid ice mass loss is hypothesized to occur¹¹⁹ and whose validity has been critically examined on observational¹²⁰ and theoretical⁷⁹ grounds. Yet among all ice shelf fracture processes, rift propagation is the mechanism by which the largest calved icebergs are created, i.e., icebergs with areal extent $O\{1 - 10 \times 10^3\}$ sq km²⁰. Although calving due to rift propagation is generally thought of as a natural cyclic process on decadal timescales²⁰, recent studies have examined the deterioration of this natural cycle²⁶ and associated increases in ice mass loss²⁷. Given the enormous scale of tabular iceberg calving, it is therefore important to better understand the rift propagation process in order to understand whether deviations from the natural rifting-calving cycle are a harbinger of Antarctic ice shelf dynamics in a warming climate. Here, we overcome the perennial limitation of studies of calving processes –namely, a lack of *in situ* observations²⁵– and present the first-known near-field seismic observations of a large ice shelf rift propagation event.

3.1 NEAR-RIFT OBSERVATIONS

Our observations come from the Pine Island Glacier Ice Shelf (PIG), a fast-flowing ice shelf in West Antarctica that was the single largest Antarctic contributor to sea level rise in the period 1979–2017³. Since 1992, tabular icebergs have calved from PIG every 2–6 years along rifts that propa-

gated from the northern and southern shear margins, maintaining a relatively consistent ice front position and orientation²⁶. In 2015, calving occurred along a rift that initiated in the ice shelf's center for the first time, resulting in substantial ice front retreat and reorientation¹⁰⁵ that has continued to the present. Before this change in ice front geometry, the last calving event occurred in 2013 along a rift that propagated from the northern shear margin across the ice shelf, hereinafter referred to as R2011 for the year of its initiation. We use synthetic aperture radar data collected by the TerraSAR-X (TSX) satellite to identify an episode of rapid propagation during the rifting that preceded the 2013 calving event. We identify the rift seismic signal within data recorded by three Nanometrics Trillium 120 seismometers deployed on PIG ice shelf and three Nanometrics Trillium 240 seismometers deployed across West Antarctica⁹⁹. We then use the characteristics of the signal to analyze the mechanical response of the ice shelf to rift propagation and estimate the speed of rift extension.

TSX data from May 8, 2012 04:04 UTC show the PIG ice shelf before the episode of rift extension (Figure 3.2A). The rift R2011 spanned 33.8 km across the ice shelf from the northern shear margin and a band of ~ 20 shorter parallel fractures spanned ~ 5 km from the northern shear margin. The data show no major rifts besides R2011. TSX data from May 11, 2012 03:13 show PIG ice shelf after the episode of rift extension (Figure 3.2B), providing a three-day time window around the episode of rift extension. One of the northern shear margin fractures, hereinafter referred to as R2012, propagated 10.5 km, terminating at -74.955°N , -101.16°E , where it connected with R2011. A high-resolution digital elevation model of PIG¹⁰⁷ shows that the tip of R2012 was located in a basal trough before propagation, consistent with previous observations that suggest basal channels strongly influence rift propagation on PIG and other ice shelves^{121,122}.

We employ a semi-automated scheme to identify the extent of R2012 before and after the extension. We use TSX data from May 5, 2012 03:22:11 and May 11, 2012 03:13:39 since these two data were captured from similar incidence angles and span the same spatial extent. To align the images,

we first transform both to EPSG:3245. To remove the effect of advection of ice between the two images, we identify a small window of the data surrounding the tip of R2011, which remains stationary in a reference frame fixed to ice flow. We then cross-correlate the windows containing the rift tip from each TSX data to compute the optimal shift between the two data. We then use the computed shift to align the two data.

To measure the increase in length of R2012, we first multiply the data by -1 and rescale it so that all pixel values fall between 0 and 1, resulting in an image where pixels with values close to 1 correspond to dark features like rifts. We then set all pixels with values above a manually-determined threshold to 1 and all pixels below that threshold to 0. This results in a binary image where dark features like rifts have values of 1 and the background has a value of 0. We then dilate the binary images to remove jagged edges and smooth 1-valued regions before subtracting the pre-extension image from the post-extension image. This removes all features that stayed constant between May 5 and May 11, including shear margin fractures and R2011. We then extract the largest 1-valued region from the subtracted image, which corresponds to the area that R2012 increased by between May 5 and May 11. We then remove all the rift area behind the manually-identified position of the rift tip before extension to overcome the difficulty in detecting hairline fractures using binary thresholding. Finally, we skeletonize the binary rift image, measure the length of the skeleton's main branch in pixels, and multiply by the TSX data's pixel size to extract the length that R2012 increased between May 5 and May 11. We estimate an increase in length of 10473.26 meters.

To measure the initial length and width of R2012, we first clip the data to include only the initially-open portion of R2012. We rescale and threshold the data as described above to yield a binary image where the rift has a value of 1 and the background has a value of 0. We then skeletonize the binary rift image, measure the length of the skeleton's main branch in pixels, and multiply by the TSX data's pixel size to extract the initial length of R2012. Finally, we sum the binary rift image to obtain the area of the rift in pixels, multiply by the TSX data's pixel size to obtain the rift area

in meters, then divide by the initial length to obtain an estimate of the average rift width. We estimate an initial length of 3889.94 meters and an initial width of 91.25 meters. We follow the same procedure to measure the length of R2011, which we estimate to be 33793.7 meters.

Seismic data recorded in the time window established by TSX data contains a single notable signal, recorded on May 9, 2012 at 18:03 (Figure 3.2C). We hypothesize that this signal, the largest amplitude signal within the three-day window, was generated by the extension of R2012 observed in TSX data. We use the cumulative amplitude distribution of the signal to estimate a duration of 2.09 hours, longer in duration than all other signals in the time window by an order of magnitude. The May 9 event has a peak vertical ground velocity of 0.234 mm/s and peak vertical ground displacement of 0.195 mm at a distance of 12 km and uniquely contains significant energy at periods up to 1000 s. The sensitivity of the Trillium 120 seismometer is reduced below its natural period of 120 s, suggesting that the amplitudes recorded between periods of 120 s and 1000 s may underestimate actual ice shelf velocities at those periods. Between 1000 s and 1 s periods, the signal exhibits high-frequency-first dispersion characteristic of flexural gravity (FG) waves (Figure 3.2D), a wave type that propagates as a coupled beam flexural and ocean surface wave^{54,123,91,124}. At frequencies above 1 Hz, the signal consists of body and surface waves that gradually increase in amplitude before abruptly decaying after 302 s (Figure 3.2E). These higher-frequency phases are also recorded by regional POLENET stations DNTW, THUR, and UPTW, respectively located 250, 294, and 360 km from PIG.

A previous study of fracture at PIG identified FG waves generated by gradual propagation of R2011¹²⁵, suggesting the extension of R2012 is a reasonable source for the May 9 event. In addition to rift propagation, FG waves on ice shelves are generated by incoming ocean waves¹²⁶. However, ocean wave sources cannot account for seismic phases recorded by regional stations hundreds of kilometers away, and we therefore conclude that incoming ocean waves must not have generated the rift signal. Additionally, the spectrum of the May 9 event is markedly different than teleseis-

mic earthquake spectra recorded by the same instrument. The May 9 event had a dominant period of 600.0 s, while the M_w 7.7 Scotia Sea earthquake that occurred on November 17, 2013, had a dominant period of 17.14 s (Figure 3.1). We thus conclude that teleseismic waves must not have generated the May 9 event signal.

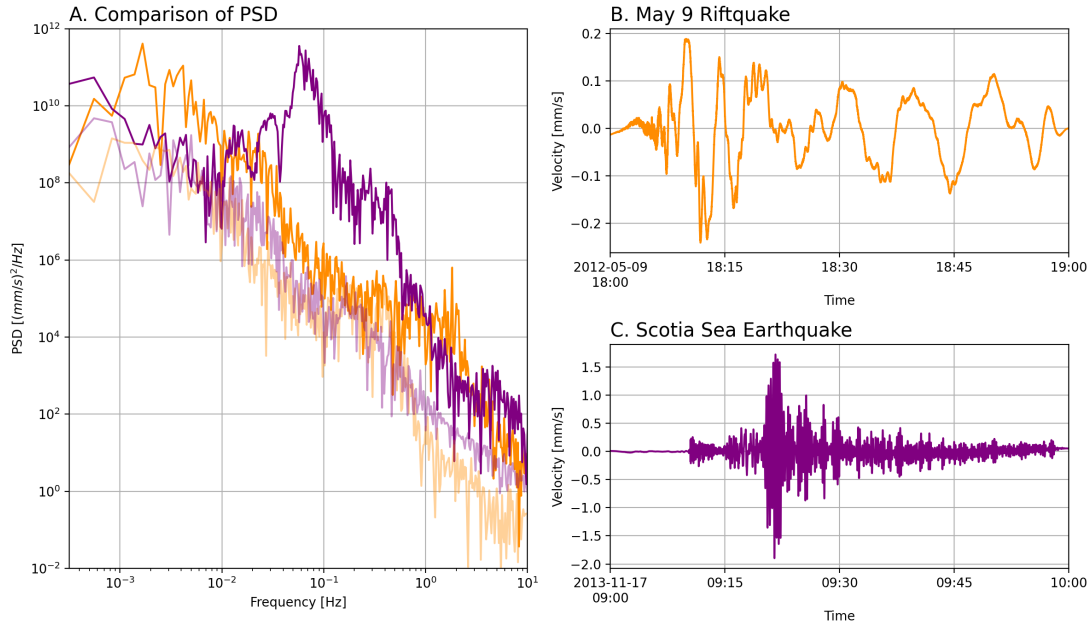


Figure 3.1: Comparison of May 9, 2012 rift event and November 17, 2013 M_w 7.7 Scotia Sea earthquake. All displayed data are vertical velocity seismograms recorded by station PIG2, and all displayed spectra were computed using these data. (a) Comparison of power spectral density (PSD) of May 9 rift event, Scotia Sea earthquake, and noise. PSD of May 9 rift event is shown in orange, and PSD of one hour of noise prior to the May 9 rift event is shown in light orange. PSD of Scotia Sea earthquake is shown in purple, and PSD of one hour of noise prior to the Scotia Sea event is shown in light purple. The May 9 event had a dominant period of 600.0 s, while the Scotia Sea earthquake had a dominant period of 17.1 s. (b) Seismic recording of May 9 rift event. The rift signal is clearly dispersive, and characteristic 600.0 s period waves are clearly visible after T18:30. (c) Seismic recording of Scotia Sea earthquake. Scotia Sea signal is not clearly dispersive, and does not contain significant power at periods below 100 s.

To locate the candidate rift event, we employ a grid search algorithm using arrival times at locally and regionally-deployed stations. First, we obtain the arrival time of high-frequency waves (1.5-5 Hz) at each station by cross-correlating the filtered event waveform recorded at PIG2, the

closest station to R2012, with the filtered waveform recorded at each other station. The resulting cross-correlation functions allow us to obtain the shifts required to align the waveform recorded at PIG2 with the waveform at each other station. Using the known sampling rate, we use these shifts to compute relative arrival times. Next, we calculate the velocity of the waves recorded at each station by dividing the known distance between PIG2 and each station by the difference between the arrival time at PIG2 and each station. We carry out this procedure using vertical, north-south, and east-west component data recorded at stations PIG2, PIG4, PIG5, THUR, BEAR, DNTW, and UPTW.

We then carry out the grid search by iterating through possible origin times and spatial locations and computing the expected arrival time at each station using the previously-estimated phase velocity. We calculate the root mean square error (RMSE) between the observed and expected arrival times for all components and stations, giving a single estimate of the misfit in arrival times across the array. We then calculate RMSE for each possible origin time and for every spatial point in a regular grid to obtain a map of error. The event location is finally determined by identifying the spatial point and origin time that correspond to the lowest RMSE.

To further constrain the source location, we use the polarization direction of recorded horizontal waves to compute the epicentral back-azimuths. First, we identify which station recorded the first arrival by cross-correlating the respective component waveforms between each station. The first-arrival station is the one that records the trace requiring the largest shift forward in time to align with the other traces. We then determine the polarization direction of the recorded waves using principal component analysis (PCA). By performing PCA on the east-west and north-south seismograms, we obtain the PCA first component, a vector corresponding to the direction along which the majority of the variation in the data occurs. We infer the polarization direction from the PCA first component, which corresponds to one of two possible propagation directions separated by 180 degrees. To resolve this 180-degree ambiguity, we determine the predicted station of the first arrival by

computing the stations farthest from the array centroid in both possible directions of propagation, which are expected to record the first arrivals for an incoming plane wave. We then adjust the sign of the PCA first component to match the propagation direction whose predicted first arrival agrees with the observed first arrival. We repeat this procedure using data recorded at each station and sum the PCA first component vectors from each station to obtain an average propagation direction. Finally, we retrieve a back-azimuth by taking the arctangent of the quotient of the two elements of the PCA component vector. We repeat the entire procedure for each 50 s time window in the event, resulting in a distribution of back-azimuths calculated for each time window within the event. We obtain a single event back-azimuth by taking the circular mean of the back-azimuths calculated from each time window, with the back-azimuth from each time window weighted by the norm of the summed PCA components across the array for that window. The weighted circular mean for the back-azimuth distribution $\theta_1, \dots, \theta_n$ with PCA norms w_1, \dots, w_n of a single event with n time windows is:

$$\bar{\theta} = \text{atan2} \left(\frac{1}{n} \sum_{j=1}^n w_j \sin(\theta_j), \frac{1}{n} \sum_{j=1}^n w_j \cos(\theta_j) \right)$$

Our grid-search inversion of arrival times at locally and regionally-deployed seismic stations finds its lowest-error region where R2012 connects to R2011 (Figure 3.2B), further supporting the hypothesis that the extension of R2012 generated the May 9 event. The polarization of waves recorded at locally-deployed stations corresponds to a backazimuth of 308.1 ± 6.2 degrees (Figure 3.2B), in agreement with the backazimuth of R2012, confirming that the recorded waves propagated to the local seismic stations from the direction of R2012. Because the best-fit event location coincides with R2012 and because both teleseismic and ocean wave sources are inconsistent with the seismic observations, we conclude that the May 9, 18:03 event was the seismic signal generated by the extension of R2012.

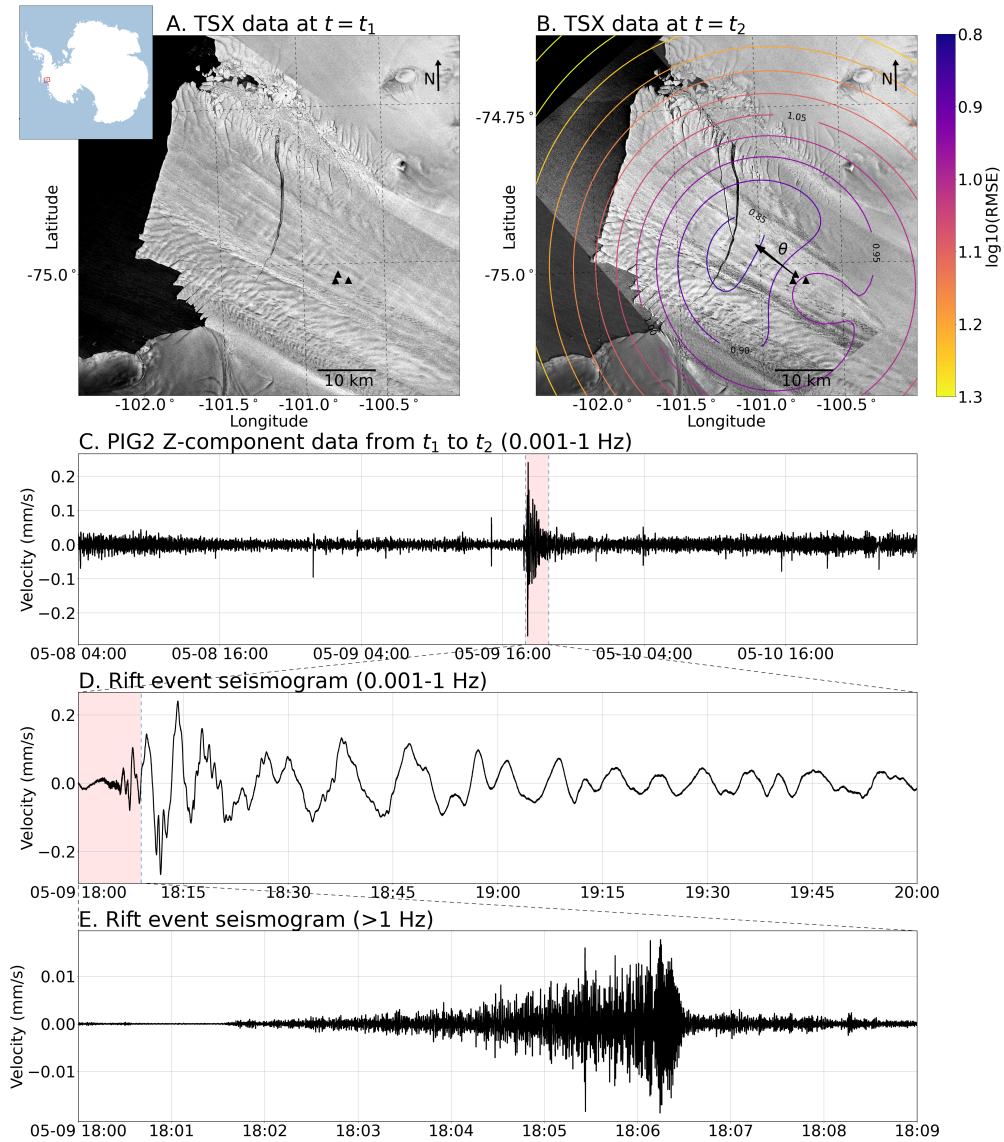


Figure 3.2: TSX and seismic data surrounding 10.5 km of rift propagation. All seismic data are vertical velocity seismograms recorded by station PIG2. **(a)** TSX data from May 8, 2012 04:04 (t_1) before propagation of R2012. Black triangles show on-ice seismic stations. Inset shows location of PIG within Antarctica. **(b)** TSX data from May 11, 2012 03:13 (t_2) after propagation of R2012. Contours show the logarithm of root mean squared error (RMSE) in arrival time residuals from a gridsearch of possible locations of the May 9 signal computed using on-ice seismic stations and regionally-deployed seismic stations (not shown). Arrow denoted by θ shows backazimuth computed using the polarization of seismic waves recorded by on-ice seismic stations. **(c)** Seismogram spanning the time window between TSX data. Rift event signal is highlighted in pink. **(d)** Seismogram of rift event filtered between 0.001 Hz and 1 Hz. In this frequency band, signal is dominated by flexural gravity (FG) waves. Resonance of ice shelf modes results in an event duration on the order of hours. **(e)** Seismogram of rift event filtered above 1 Hz. In this frequency band, signal is dominated by P waves and surface waves. The abrupt decay of the rift event signal 302 s after the onset of the event indicates the conclusion of rift propagation.

To understand the dynamics of the observed rift propagation, we estimate the rate of extension using the duration of radiated body and surface waves and the increase in length estimated from TSX data. Radiated body and surface waves gradually increase in amplitude after event onset until stopping abruptly after 302 s (Figure 3.2E), indicating the conclusion of propagation, when R2012 collided with R2011. We thus infer that the observed 10.5 km of rift extension occurred over 302 s, corresponding to an average rupture velocity of 34.8 m/s. To the best of our knowledge, this is the fastest rift propagation speed ever observed. R2012 extended over a duration of time two orders of magnitude below the Maxwell time of ice, which is around 11 hours²⁸, supporting the hypothesis that the observed rift extension occurred through dynamic brittle fracturing. However, elastodynamic theory predicts opening mode fracture propagation at rates approaching the Rayleigh wave speed of the fracturing material¹²⁷, which is between 1500 and 2000 m/s in the ice¹²⁸. Why, then, did R2012 propagate two orders of magnitude below the Rayleigh wave speed?

3.2 MODEL OF FLEXURAL GRAVITY WAVES ON A VISCOELASTIC ICE SHELF

We analyze the response of PIG to rift propagation using a simple model of an infinite viscoelastic beam. First, we write the governing equation for a purely elastic homogeneous dynamic beam:

$$\rho_i H_i \frac{\partial^2 w}{\partial t^2} + D \frac{\partial^4 w}{\partial x^4} + \rho_w g w + \rho_w \frac{\partial \varphi}{\partial t} = 0$$

where $D \equiv EI = EH_i^3/[12(1 - \nu^2)]$ is the flexural rigidity with second moment of area $I = \int_{-H_i/2}^{H_i/2} z^2 dz$, E is the Young's modulus of ice, ν is the Poisson's ratio of ice, t is time, x is horizontal position, g is gravitational acceleration constant, H_i is the ice thickness, ρ_i is the density of ice, ρ_w is the density of water, w is the vertical displacement of the beam, and φ is the ocean surface velocity potential.

We first take the Fourier transform in space of the governing equation to obtain:

$$\rho_i H_i \frac{\partial^2 \bar{w}}{\partial t^2} + D \xi^4 \bar{w} + \rho_w g \bar{w} + \rho_w \frac{\partial \bar{\varphi}}{\partial t} = 0$$

where ξ is the wavenumber, \bar{w} is the Fourier-transformed displacement, and $\bar{\varphi}$ is the Fourier-transformed ocean surface velocity potential.

To obtain an expression for $\partial \bar{\varphi} / \partial t$, we solve the the ocean surface wave equation for a body of water with infinite length and finite depth:

$$\frac{\partial^2 \varphi}{\partial x^2} + \frac{\partial^2 \varphi}{\partial y^2} = 0 \quad -\infty < x < \infty, \quad -b_w < y < 0$$

Taking the Fourier transform and applying the boundary conditions yields the following expression for $\bar{\varphi}$ at the ocean surface:

$$\bar{\varphi} = \frac{\partial \bar{w}}{\partial t} \left(\frac{\coth(\xi b_w)}{\xi} \right)$$

We differentiate with respect to time to obtain $\partial \bar{\varphi} / \partial t$:

$$\frac{\partial \bar{\varphi}}{\partial t} = \frac{\partial^2 \bar{w}}{\partial t^2} \gamma$$

where $\gamma = \frac{\coth(b_w \xi)}{\xi}$

Substituting into the Fourier-transformed governing equation:

$$\rho_i H_i \frac{\partial^2 \bar{w}}{\partial t^2} + D \xi^4 \bar{w} + \rho_w g \bar{w} + \rho_w \gamma \frac{\partial^2 \bar{w}}{\partial t^2} = 0$$

We take the Laplace transform in time to obtain:

$$\rho_i H_i s^2 \bar{w}^* + D \xi^4 \bar{w}^* + \rho_w g \bar{w}^* + \rho_w \gamma s^2 \bar{w}^* = 0$$

where s is the frequency. Dividing by \bar{w}^* and factoring:

$$(\rho_i H_i + \rho_w \gamma) s^2 + \rho_w g = -D \xi^4$$

We non-dimensionalize by $\rho_w g$:

$$\left(\frac{1}{N^2} + \frac{\gamma}{g} \right) s^2 + 1 = \frac{-D \xi^4}{\rho_w g} \quad (3.1)$$

$$\text{where } N = \sqrt{\frac{\rho_w g}{\rho_i H_i}}.$$

The above equation applies to a purely elastic beam. To extend the analysis to a viscoelastic beam, we employ the viscoelastic correspondence principle. For a Maxwell viscoelastic material, the shear modulus μ and Lamé's first parameter λ may be rewritten in the Laplace transform domain as:

$$\bar{\mu} = \frac{s\mu}{s + t_m^{-1}} \quad \bar{\lambda} = \frac{s\lambda + K t_m^{-1}}{s + t_m^{-1}}$$

where K is the bulk modulus, $t_m^{-1} = \frac{\eta}{\mu}$ is the Maxwell time, and η is the dynamic viscosity of ice.

By employing the variety of identities that relate elastic parameters and substituting, we obtain a viscoelastic flexural rigidity \bar{D} :

$$\bar{D} = \frac{\frac{1}{3} H_i^3 \mu \left(\frac{3}{2(1+\nu)} + (s t_m)^{-1} \right)}{\left(\frac{3(1-\nu)}{1+\nu} + (s t_m)^{-1} \right) (1 + (s t_m)^{-1})}$$

For convenience, we define $\nu_1 \equiv \frac{3(1-\nu)}{1+\nu}$ and $\nu_2 \equiv \frac{3}{2(1+\nu)}$:

$$\bar{D} = \frac{\frac{1}{3} H_i^3 \mu \left(\nu_2 + (s t_m)^{-1} \right)}{\left(\nu_1 + (s t_m)^{-1} \right) (1 + (s t_m)^{-1})}$$

We substitute \bar{D} into Equation 3.1, and after much tedious algebra, obtain the dispersion relation for a dynamic viscoelastic beam:

$$(I + W)\nu_1 s^4 + (I + W)(\nu_1 + 1)t_m^{-1} s^3 + [(I + W)t_m^{-2} + \nu_1 + F\nu_2] s^2 +$$

$$[\nu_1 + 1 + F] t_m^{-1} s + t_m^{-2} = 0 \quad (3.2)$$

where $I = \frac{1}{N^2}$, $W = \frac{\gamma}{g}$, and $F = \frac{\frac{1}{3}E_i^3 \mu \xi^4}{\rho_w g}$.

In the subsequent sections, we use the dispersion relation defined by Equation 3.2 to analyze ice shelf behavior. We obtain the solutions to Equation 3.2 by calculating the coefficients of each term containing the frequency s and employing a numerical polynomial root finding algorithm.

3.2.1 RESONANCE PERIODS

To calculate the resonance periods of PIG, we first identify the characteristic wavenumbers of the ice shelf using the expression:

$$\xi = \frac{\pi}{d}(N + 1)$$

where ξ is the wavenumber, d is the relevant ice shelf dimension, and N is the resonance mode, with the fundamental mode corresponding to $N = 0$.

We compute the characteristic wavenumbers associated with the first three modes of the length and width of PIG. We then solve the dynamic viscoelastic beam dispersion relation (Equation 3.2) for each characteristic wavenumber to obtain the angular frequency corresponding to each mode. We then finally compute resonant periods from the angular frequency of each mode.

3.2.2 E-FOLDING TIME

To estimate the theoretical e-folding time for waves at the observed 600 s dominant period, we first estimate the reflection coefficient for the ice-ocean interface. At long periods, the reflection coefficient for flexural gravity waves incident on an ice front is approximately equal to the reflection coefficient for shallow-water waves incident on a step change in water depth¹²⁴:

$$R = \frac{\sqrt{H_w} - \sqrt{H_c}}{\sqrt{H_w} + \sqrt{H_c}}$$

Because we seek to explain the e-folding time for 600 s period waves, which are sufficiently long period to propagate as shallow water waves with negligible flexure, we use the relation above to compute a reflection coefficient of 0.257. Next, we compute the number of reflections n necessary for the amplitude to decay by a factor of $\frac{1}{e}$. We solve the following equation for n using the computed reflection coefficient:

$$R^n = \frac{1}{e}$$

We then obtain the velocity c for 600 s period waves by solving the dynamic beam dispersion relation. Finally, we calculate e-folding time using the following relation, where L is 70 km length of FIG:

$$t_{fold} = \frac{2Ln}{c}$$

3.2.3 VISCOUS DAMPING

To analyze the influence of viscous damping on FG wave decay time, we compute the value of the quality factor Q , which describes the decay of a damped oscillating system:

$$Q = \left| \frac{Im(s)}{2Re(s)} \right|$$

We compute Q using the numerically-determined roots s of the wavelike solution of Equation 3.2 and an asymptotic solution obtained by taking the Taylor series approximation of Equation 3.2 at low frequency:

$$s \approx \sqrt{\frac{-1}{w}} - \frac{7}{24}F$$

For the dominant 600 s period waves of the rift event signal, we compute a Q value of 8.5e5 using the numerically-computed roots and a Q value of 4.96e5 using the asymptotic solution.

Q is also defined by:

$$Q = \pi n$$

where n is the number of cycles required for signal amplitudes to decay by a factor of e . We employ this relation to estimate the Q value of the observed rift signal to evaluate whether the Q value associated with the ice shelf viscosity can explain the observed decay time. To estimate the observed Q , we compute the time required for the signal to decay from its max amplitude A_{max} to an amplitude of $\frac{1}{e}A_{max}$ and use the dominant period of the signal to convert the decay time to number of cycles. This procedure is repeated at a variety of periods to obtain an estimate of observed Q as a function of frequency. We determine that Q for the observed 600 s period waves is 6.21. This value is much lower than the computed theoretical Q values, meaning that the observed waves decayed much more quickly than predicted for an infinite viscoelastic beam. We therefore infer that the observed decay time cannot be explained by viscous damping of the ice shelf. A physical interpretation of this finding follows. At very low frequencies, FG waves propagate almost entirely as ocean sur-

face waves, which cause the ice shelf to float up and down rather than flex. Because ice shelf flexure is so minimal at these frequencies, the vast majority of FG wave energy is associated with ocean wave propagation, which is insensitive to the viscosity of the floating ice shelf. Viscous damping is therefore unable to effectively damp such low frequency FG waves and cannot account for the observed decay time.

3.3 MODEL OF OCEAN COUPLED RIFT PROPOGATION

We model the coupled ocean-rift system using simple linear elastic fracture mechanics and fluid dynamics. We utilize a coordinate system where the ice shelf base has a vertical position of 0, the ice front has a position of 0 in the y -direction, and the back of the rift has a position of 0 in the x -direction. Our modeling employs the following equations, which are derived or discussed in more detail in the following sections.

$$\text{Conservation of water mass in the rift: } u = \frac{1}{LH_c} \left[wL \frac{d\eta}{dt} + w\eta \frac{dL}{dt} + L\eta \frac{dw}{dt} \right] \quad (3.3)$$

where η is the water level within the rift, w is the width of the rift, and u is the flow rate into the cavity through a cross section of height H_c and length L , equal to the length of the rift.

$$\text{Conservation of fluid momentum: } L_c \frac{du}{dt} + (H_w - H_c) \frac{d\eta^2}{dt^2} = g(H_w - H_c - \eta) \quad (3.4)$$

where L_c is the horizontal position of the rift and H_w is the height from the ice shelf base to the hydrostatic water line.

$$\text{Rift stresses: } \sigma = R_{xx} + \frac{\rho_w g \eta^2}{2H_i} - \frac{\rho_i g H_i}{2}$$

Rift width: $w = w_0 + \frac{\pi\sigma}{4\mu^*}L$

where $\mu^* = \mu / (1 - \nu)$, μ is the shear modulus, and ν is Poisson's ratio.

Rift tip equation of motion: $\frac{dL}{dt} \approx c_r \left(1 - \frac{K_c^2}{K_I^2}\right)$ (3.5)

where K_I is the stress intensity factor experienced by the rift and K_c is the fracture toughness of ice.

We seek to solve this system of ordinary differential equations for L and η . To take advantage of widely-available solvers for systems of ordinary differential equations. An important class of such solvers handles systems of equations with the form:

$$x' = f(x, x')$$

i.e. systems that only have dependence on the first derivatives x' of the state vector x . Through algebraic manipulation, we write Equation 3.3, Equation 3.4, and Equation 3.5 in this form. This requires introducing a dummy variable $\chi = \eta'$ so the 2nd derivative η'' can be written as a first derivative. This also requires us to obtain an equation for χ' . We accomplish this by rearranging Equation 3.4, analytically computing all the necessary derivative terms, and substituting. This process yields a set of equations written in a convenient way for numerical solutions. However, the equations in the previous sections are more physically interpretable, so the forms used for numerical solution are not reproduced here. In our simulations, we first compute the ice shelf extensional stress R_{xx} necessary for a fracture of the prescribed initial geometry to experience a stress intensity factor that barely exceeds the fracture toughness of ice. We then use compute the stress and stress intensity factors corresponding to R_{xx} assuming an initial steady-state water surface height of $\eta = H_i \rho_w / \rho_i$. This initiates fracture propagation at a rate determined by Equation 3.5. R_{xx} is held

fixed through the simulation, and the stress applied to the rift evolves through time as η changes.

3.3.1 CONSERVATION OF FLUID MASS

Water entering the subshelf cavity has a mass flow rate $\rho u L H_c$, where u is the flow rate into the cavity through a cross section of height H_c and length L , equal to the length of the rift. The mass flow rate of water entering the cavity must equal the rate of change of the total mass of water within the rift:

$$\rho u L H_c = \frac{d}{dt} \int \rho dV$$

We rewrite the volume integral on the right as integration across the width of the rift, along the length of the rift, and up the height of the water column in the rift:

$$\rho u L H_c = \rho \frac{d}{dt} \int_{L_c}^{L_c+w} \int_0^L \int_0^\eta dz dx dy$$

where L_c is the distance from the ice front to the frontward side of the rift and w is the width of the rift. We apply the Leibniz rule to the outermost integral:

$$\rho u L H_c = \rho \int_{L_c}^{L_c+w} \frac{d}{dt} \int_0^L \int_0^\eta dz dx dy + \rho \int_0^L \int_0^\eta dz dx \frac{d}{dt} (L_c + w) - \rho \int_0^L \int_0^\eta dz dx \frac{dL_c}{dt}$$

We assume L_c remains constant:

$$\rho u L H_c = \rho \int_{L_c}^{L_c+w} \frac{d}{dt} \int_0^L \int_0^\eta dz dx dy + \rho \int_0^L \int_0^\eta dz dx \frac{dw}{dt}$$

Evaluating integrals, we obtain:

$$\rho u L H_c = \rho w \frac{d}{dt} \int_0^L \int_0^\eta dz dx + \rho L \eta \frac{dw}{dt}$$

In similar fashion, we apply the Leibniz rule to the remaining integrals:

$$\rho u LH_c = \rho \left[wL \frac{d\eta}{dt} + w\eta \frac{dL}{dt} + L\eta \frac{dw}{dt} \right]$$

Finally, dividing by ρLH_c yields an equation for u :

$$u = \frac{1}{LH_c} \left[wL \frac{d\eta}{dt} + w\eta \frac{dL}{dt} + L\eta \frac{dw}{dt} \right] \quad (3.3)$$

3.3.2 CONSERVATION OF FLUID MOMENTUM

We model water flow from the open ocean through the subshelf cavity into the rift from below using the unsteady Bernoulli equation. A brief derivation follows. From Newton's second law of motion, the rate of change of linear momentum must equal the force per volume F applied on a parcel of fluid:

$$\frac{D}{Dt}(\rho v) = F$$

We rewrite the total derivative term on the left and assume the fluid is incompressible:

$$\rho \left(\frac{\partial v}{\partial t} + v \nabla v \right) = F$$

We recall from vector calculus identities:

$$v \nabla v = (v \cdot \nabla)v = \frac{1}{2} \nabla v^2 + v \times (\nabla \times v)$$

We assume the flow of water is irrotational, meaning the curl of the velocity field $\nabla \times v$ must

equal to:

$$v \nabla v = (v \cdot \nabla)v = \frac{1}{2} \nabla v^2$$

Substituting, we obtain:

$$\rho \left(\frac{\partial v}{\partial t} + \frac{1}{2} \nabla v^2 \right) = F$$

We assume that friction on the fluid is negligible. The only forces acting on the fluid are gravitational force, equal to the gradient of gravitational potential energy U , and pressure gradient force, equal to the gradient of pressure P :

$$F = -\nabla U - \nabla P = -\nabla \rho g z - \nabla P$$

Substituting:

$$\rho \left(\frac{\partial v}{\partial t} + \frac{1}{2} \nabla v^2 \right) = -\nabla \rho g z - \nabla P$$

Rearranging:

$$\rho \frac{\partial v}{\partial t} + \nabla P + \rho \frac{1}{2} \nabla v^2 + \nabla \rho g z = 0$$

Finally, we integrate over a stream line between two locations denoted 1 and 2 to obtain the equation of unsteady Bernoulli flow:

$$\int_1^2 \left[\rho \frac{\partial v}{\partial t} + \nabla P + \rho \frac{1}{2} \nabla v^2 + \nabla \rho g z \right] dS = \int_1^2 0 dS$$
$$\rho \int_1^2 \frac{\partial v}{\partial t} dS + \left[P + \frac{1}{2} \rho v^2 + \rho g z \right]_2 - \left[P + \frac{1}{2} \rho v^2 + \rho g z \right]_1 = 0$$

We now apply this result to the stream line connecting the cavity-ocean interface and the rift water surface. At the base of the ice shelf where the subshelf cavity meets the ocean, $z = 0$, $v = u$, and $P = \rho g(H_w - H_c)$, where H_w is the depth of the ocean, H_c is the height of the subshelf cavity, and u is the flow rate from the ocean into the subshelf cavity. Therefore, we write:

$$[P + \frac{1}{2}\rho v^2 + \rho g z]_1 = \rho g(H_w - H_c) + \frac{1}{2}\rho u^2$$

At the water surface in the rift, $z = \eta$, $v = \frac{d\eta}{dt}$, and $P = 0$, where η is the height of the water surface in the rift, and $\frac{d\eta}{dt}$ is the rate that the height of the water surface changes. Therefore, we write:

$$[P + \frac{1}{2}\rho v^2 + \rho g z]_2 = \frac{1}{2}\rho \frac{d\eta^2}{dt} + \rho g \eta$$

We split the stream line integral into two terms. The first term represents water flow from the ice front to a rift with horizontal position L_c . The second term represents water flow from the bottom of the rift to the water surface within the rift:

$$\rho \int_1^2 \frac{\partial v}{\partial t} dS = \rho \int_0^{L_c} \frac{\partial v}{\partial t} dy + \rho \int_0^\eta \frac{\partial v}{\partial t} dz$$

We assume that flow velocity is spatially constant from the ice front to the horizontal position of the rift and from the bottom of the rift to the water surface in the rift. Flow velocity along each segment is therefore only a function of time, allowing partial derivatives to be replaced with ordinary derivatives. Because $v = u$ at the ice front and $v = \frac{d\eta}{dt}$ at the water surface in the rift, we write:

$$\rho \int_1^2 \frac{\partial v}{\partial t} dS = \rho \int_0^{L_c} \frac{du}{dt} dy + \rho \int_0^\eta \frac{d^2\eta}{dt^2} dz$$

Evaluating integrals yields:

$$\rho \int_1^2 \frac{\partial v}{\partial t} dS = \rho \left[L_c \frac{du}{dt} + \eta \frac{d^2 \eta}{dt^2} \right]$$

Substituting the back into the Bernoulli flow equation:

$$\rho \left[L_c \frac{du}{dt} + \eta \frac{d^2 \eta}{dt^2} \right] + \left[\frac{1}{2} \rho \frac{d\eta^2}{dt} + \rho g \eta \right] - \left[\rho g (H_w - H_c) + \frac{1}{2} \rho u^2 \right] = 0$$

We divide by ρ and group terms:

$$L_c \frac{du}{dt} + \eta \frac{d^2 \eta}{dt^2} + \frac{1}{2} \left(\frac{d\eta^2}{dt} - u^2 \right) + g(\eta - (H_w - H_c)) = 0$$

We move the terms with g to the right side:

$$L_c \frac{du}{dt} + \eta \frac{d^2 \eta}{dt^2} + \frac{1}{2} \left(\frac{d\eta^2}{dt} - u^2 \right) = g(H_w - H_c - \eta) \quad (3.6)$$

3.3.3 LINEARIZED CONSERVATION OF FLUID MOMENTUM

We linearize Equation 3.6 by considering perturbations from the system at rest. In this reference state, all time derivatives are 0. We eliminate terms with time derivatives and replace η and u with the reference state water level η_0 and flow rate u_0 :

$$-\frac{1}{2} u_0^2 = g(H_w - H_c - \eta_0)$$

From Equation 3.3, u must be 0 at rest, so the reference flow velocity u_0 equals 0. We substitute u_0 into the above expression, divide by g , and rearrange to obtain an expression for the reference water level η_0 :

$$\eta_0 = H_w - H_c$$

We write the water level and flow velocity as the sum of the reference state and perturbations to the reference state:

$$\eta = \eta_0 + \delta\eta = H_w - H_c + \delta\eta$$

$$u = u_0 + \delta u$$

We rewrite Equation 3.6 for perturbations from the rest state:

$$L_c \frac{d}{dt}(u_0 + \delta u) + (\eta_0 + \delta\eta) \frac{d^2}{dt^2}(\eta_0 + \delta\eta) + \frac{1}{2} \left[\left(\frac{d}{dt}(\eta_0 + \delta\eta) \right)^2 - (u_0 + \delta u)^2 \right] = g(H_w - H_c - (\eta_0 + \delta\eta))$$

We substitute the reference water level and flow rate:

$$L_c \frac{d}{dt} \delta u + (H_w - H_c + \delta\eta) \frac{d^2}{dt^2} (H_w - H_c + \delta\eta) + \frac{1}{2} \left[\left(\frac{d}{dt} (H_w - H_c + \delta\eta) \right)^2 - \delta u^2 \right] = -g \delta\eta$$

We assume that products of perturbations or their derivatives are small and eliminate terms:

$$L_c \frac{d}{dt} \delta u + (H_w - H_c) \frac{d^2}{dt^2} \delta\eta = -g \delta\eta$$

Having linearized the system, we rewrite for the total water surface height. Recalling that $\delta\eta = \eta - \eta_0$ and $\delta u = u - u_0$:

$$L_c \frac{d}{dt} (u - u_0) + (H_w - H_c) \frac{d^2}{dt^2} (\eta - \eta_0) = -g (\eta - \eta_0)$$

Finally, we substitute the reference state variables and eliminate time derivatives of constants:

$$L_c \frac{du}{dt} + (H_w - H_c) \frac{d\eta^2}{dt^2} = g(H_w - H_c - \eta) \quad (3.4)$$

3.3.4 RIFT STRESSES

The stress experienced by the rift is the sum of the ice shelf extensional stress R_{xx} , the depth-averaged ice overburden stress acting along the walls of the rift σ_i , and the depth-averaged water pressure applied by the water within the rift σ_w :

$$\sigma = R_{xx} + \sigma_w - \sigma_i$$

where positive signs denote tension and negative signs denote compression. We write the depth-averaged water pressure within the rift σ_w and the depth-averaged ice overburden σ_i for an ice shelf with thickness H_i :

$$\sigma_w = \frac{1}{H_i} \int_0^\eta \rho_w g (\eta - z) dz$$

$$\sigma_i = \frac{1}{H_i} \int_0^{H_i} \rho_i g (H_i - z) dz$$

Evaluating integrals yields:

$$\sigma_w = \frac{\rho_w g \eta^2}{2H_i}$$

$$\sigma_i = \frac{\rho_i g H_i}{2}$$

Substituting:

$$\sigma = R_{xx} + \frac{\rho_w g \eta^2}{2H_i} - \frac{\rho_i g H_i}{2}$$

3.3.5 RIFT WIDTH

While real fractures vary in width along the fracture axis, we represent the rift using an spatially-constant average width that varies through time. We obtain an expression for the average width by integrating the standard parabolic crack profile along the fracture length¹²⁹. The average width can then be written the sum of the initial width w_0 and a function of the fracture length L and applied stress σ :

$$w = w_0 + \frac{\pi\sigma}{4\mu^*}L$$

where $\mu^* = \mu/(1 - \nu)$, μ is the shear modulus, and ν is Poisson's ratio.

3.3.6 RIFT TIP EQUATION OF MOTION

We assume that an ice shelf rift can be approximated as finite fracture of length L in an infinite plate subjected to uniform in-plane tension with magnitude σ . The opening mode stress intensity factor K_I for this geometry¹²⁷ is:

$$K_I = \sigma\sqrt{\pi L}$$

When the stress intensity factor K_I is less than the fracture toughness of ice K_c , fracture length does not increase. If K_I exceeds K_c , then fracture length increases at a rate dL/dt , which is approximately related to stress intensity factor K_I and Rayleigh wave speed c_r ¹²⁷ by:

$$\frac{G_c E}{(1 - \nu^2)K_I^2} \approx 1 - \frac{dL/dt}{c_r}$$

where ν is Poisson's ratio and G_c is the critical energy release rate, a material property which describes the rate at which potential strain energy must be released for fracture to occur. For plane strain conditions, the critical energy release rate is related to the fracture toughness K_c ¹²⁷ by:

$$G_c = \frac{1 - \nu^2}{E} K_c^2$$

Substituting:

$$\frac{K_c^2}{K_I^2} \approx 1 - \frac{dL/dt}{c_r}$$

Rearranging, we obtain a convenient equation for the approximate motion of the rift tip:

$$\frac{dL}{dt} \approx c_r \left(1 - \frac{K_c^2}{K_I^2} \right) \quad (3.5)$$

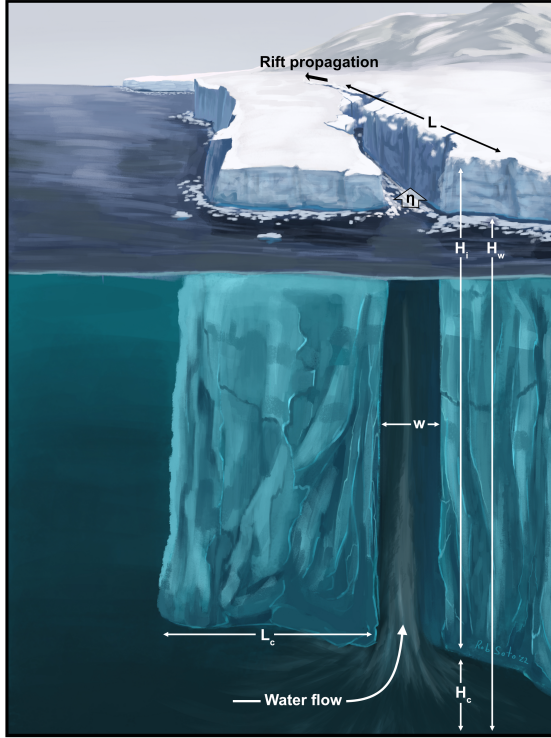
3.4 RESULTS OF MECHANICAL MODELING

We hypothesize that coupling between rift propagation and water flow within the rift explains rupture at a small fraction of the Rayleigh wave speed. To test the hypothesis, we develop a simple model of rift propagation that couples brittle fracture and water flow. The rift is represented by a linear elastic fracture in an infinite plate subject to uniform uniaxial tension. Fluid flow through the subshelf cavity into the rift is represented using the unsteady Bernoulli flow approximation. To initiate rift extension, we apply the stress required for a fracture of a chosen initial geometry to experience a stress intensity factor that just exceeds the fracture toughness of ice. As the rift propagates, the total volume within the rift increases, and water rushes in to fill the rift. However, the rift's volume increases more quickly than the rate of water inflow, reducing the average water height within the rift and decreasing the depth-integrated water pressure that acts to open the rift. The lower water pressure reduces the total resolved stress that drives rift opening, and in turn, limits the rate of

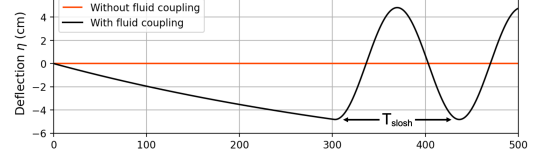
propagation. This effect results in a far lower rupture velocity than predicted for a rift with a static water height. If propagation stops abruptly, fluid inflow continues due to inertia and overshoots the steady-state water line, resulting in simple harmonic oscillations about the steady-state water line (e.g., Figure 3.2B after $t = 300$ s). These simple harmonic oscillations occur at the sloshing period, $T_{slosh} = 2\pi\sqrt{M/g}$, where $M = L_c w / H_c + H_w - H_c$ is a measure of the effective cross-sectional area of water being transported, L_c is the distance from the rift to the ice front, w is the width of the rift, H_c is the distance from the seafloor to the base of the ice shelf, and H_w is the distance from the seafloor to the water surface.

We model R2012 using an initial length of 3.9 km and an initial width of 90 m that were measured from TSX data. We assume that the ice shelf has a uniform ice thickness of 400 m, estimated from a high-resolution digital elevation model of PIG from 2012¹⁰⁷, and a uniform water depth of 840 m, estimated from a gravity-derived model of Pine Island Bay bathymetry¹³⁰. The rift is subjected to a spatially-uniform extensional stress R_{xx} . The magnitude of R_{xx} is obtained by computing the stress required for a rift with the measured initial geometry to begin unstable propagation and identifying the additional stress needed for the rift to grow 10.5 km in 302 s. We find that an applied stress of approximately 161 kPa results in 10.5 km of propagation over a duration of 302 s at an average rate of 34.8 m/s. The predicted rupture velocity of 34.8 m/s agrees with the observed rupture velocity, strongly supporting the hypothesis that coupling between rift propagation and water flow limited the observed rupture velocity to a small fraction of the Rayleigh wave speed. Without fluid coupling, a fracture of the same initial geometry subjected to the same magnitude of stress reaches 99% the Rayleigh wave speed in 302 s, highlighting how significantly the mechanism we propose influences the dynamics of rift propagation.

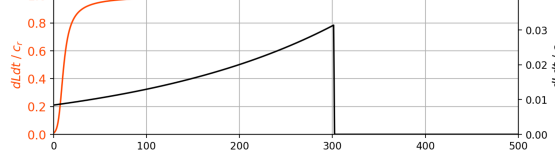
A. Schematic of rift propagation and hydrodynamics



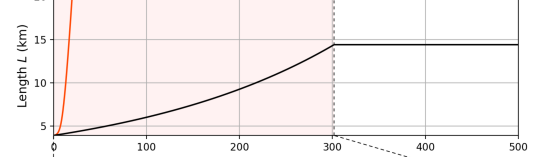
B. Deflection η from hydrostatic water level through time



C. Propagation rate dL/dt through time



D. Fracture length L through time



E. Fracture length L through time over 302 s

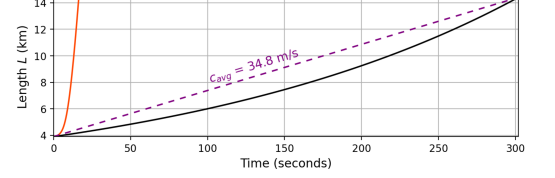


Figure 3.3: Model of fluid-coupled fracture. In all panels, the black curves show model results for a rift coupled to hydrodynamics, and the orange curves show model results for a rift uncoupled to hydrodynamics. (a) Illustration of the proposed mechanism for rift propagation at a small fraction of the Rayleigh wave speed (c_r). As the rift propagates, the increase in total volume within the rift drives the fluid to flow into the rift from below. (b) Modeled perturbation from hydrostatic water level induced by rift propagation. In the coupled case, the water level initially decreases because fluid cannot flow into the rift fast enough to maintain the hydrostatic water level. Once the rift propagation concludes, fluid flow overshoots the hydrostatic water level and oscillates at the sloshing period T_{slosh} . In the uncoupled case, the water level in the rift does not change. (c) Modeled rift propagation rate through time. In the coupled case, propagation occurs at a small fraction of c_r , because the decreasing water line reduces the water pressure acting to open the rift. In the uncoupled case, propagation approaches c_r rapidly and remains constant once c_r is reached. (d) Modeled rift length through time for 500 s of rift propagation. (e) Modeled rift length through time for 302 s of rift propagation. In the coupled case, the rift length increases by 10.5 km at an average rate of 34.8 m/s, corresponding closely to the observed propagation rate of R2012. In the uncoupled case, the rift length increases by over 500 km at a rate far exceeding the observed propagation rate of R2012.

3.5 DISCUSSION

Our observations suggest that ice shelf rift propagation occurs more rapidly than previously known. An immediate conclusion from this observation is that the timescale of fracture at R2012 is well within the regime of brittle fracture. Yet our observations and modeling show that the rift propagation of R2012 was not purely governed by the laws of linear elastic fracture mechanics (LEFM) because rift propagation was slowed down by interaction with the ocean. Several aspects of R2012 warrant further discussion.

Rapid rift propagation represents a possible mechanism of sudden ice front retreat or ice shelf collapse. While previous observations of rift propagation have overwhelmingly captured gradual or episodic propagation^{49,38,45,105}, we show that $O\{10\}$ km of rift propagation can occur in a matter of minutes. It is unknown whether this represents a rare class of rift behavior or a relatively common class of rift behavior that has remained undetected until now due to the temporal aliasing of remotely-sensed observations and a scarcity of ice shelf seismic deployments. As PIG continues to accelerate, elevated stresses and shear margin weakening are expected to enhance rift propagation^{117,74}, which can, in turn, lead to ice front retreat, buttressing loss, and further acceleration²⁷. Our observations suggest that such feedbacks at PIG and other unstable ice shelves across Antarctica may progress more rapidly than anticipated.

Flexural gravity (FG) waves generated by rift propagation can carry significant stresses. We use the wave impedance tensor⁴⁸ to compute the maximum flexural stresses carried by FG waves recorded at each local station and estimate a mean flexural stress of 3.26 kPa, consistent with typical ocean wave-induced flexural stresses on Ross Ice Shelf^{48,85} and potentially large enough to trigger additional fracturing within the ice shelf. However, PIG typically experiences a lower degree of ocean wave excitation than Ross Ice Shelf¹²⁶, so FG waves generated by rift propagation may exert a greater influence than ocean waves on the stability of fractures on PIG. The 600 s dominant period of the

recorded FG waves is between the gravest ice shelf resonance period (~ 1600 s) and the sloshing period ($T_{slosh} \sim 100$ s), suggesting that both of these processes are involved in generating the observed FG wave field. Accounting for radiative losses at the ice front using the relevant reflection coefficient¹²⁴ results in an underestimate of the e-folding duration (i.e., time to achieve decay by a factor of $1/e$) of the wave field as 16.7 minutes. However, it takes 38.2 minutes for recorded FG waves to decay by a factor of $1/e$. The e-folding duration is therefore plausibly attributed to wave generation by water sloshing within the rift that continues after rift propagation ceases (see, for example, Figure 3.3B).

We infer that large rift propagation events induce mixing in the subshelf cavity. Our model predicts that ocean water enters the rift at an average volumetric flow rate of 1.1 Sv during the 302 s duration of rift propagation. Although the total flux is small due to the 302 s duration, we expect it to induce significant mixing because the vertical flow induced by rift propagation acts perpendicular to roughly horizontal isothermal surfaces^{131,132}. Furthermore, despite significant thermocline variability, sub-shelf waters in the vicinity of the rift R2012 are deep enough to consistently reach the depth of warm circumpolar deep waters⁸⁷. Rift propagation in this setting is therefore inferred to elevate isothermal contours and cause warming of the ice–ocean interface. Localized, repeated rift propagation in areas like the northern shear margin of PIG (Figure 3.2A) may then initiate a feedback wherein rift propagation induces mixing and localized melting that contributes to marginal weakening⁷⁴ and formation of basal melt channels^{121,122}, promoting further rift propagation.

We conclude that the ocean exerts a profound influence on rift propagation. Whereas the largest fracturing events on land, i.e., tectonic earthquakes, are ultimately inertially limited¹³³, our observations and models imply that the largest fracturing events in ice, e.g., ice shelf rift propagation events, are ultimately hydrodynamically limited. We therefore add to the body of literature documenting diverse ice–ocean interactions and demonstrate that extreme ice shelf sensitivity to ocean conditions extends to the fine-scale dynamics of rift propagation.

Who cares if we're obscure

Homecoming serf

I know this quiet life, it used to hurt

But now we're dancing round and laughing in the dirt

Sidney Gish

4

New frontiers in glacier borehole distributed acoustic sensing

MOST OBSERVATIONS OF ICE SHEET DYNAMICS rely on measurements of the ice sheet surface, whether they are geodetic, seismic, or remotely sensed. While the spatial coverage and resolution of information about surficial glacier structure and motion is high due to the prevalence of satellite and airborne remote sensing, the pointwise nature of most ground-based measurements limits their spatial coverage, particularly below the glacier surface. Our understanding of glacier dynamics at depth therefore remains limited by the relatively small number of direct measurements that can be made within and below glaciers. The motion of many glaciers is highly coupled to frictional, deformational, and hydrological processes near the glacier bed, but basal properties are often inferred from models of ice flow because of the challenges inherent to directly observing the bed directly. Because most ice dynamical models are therefore solely constrained using surface measurements, our capabilities to forecast glacier behavior in a changing climate hinges on the accuracy of our representations of the glacier processes acting at depth.

Ice mass loss from the Greenland ice sheet (GIS) currently makes the largest contribution to global mean sea level rise, necessitating an understanding of the processes that control ice flow dynamics and melt in Greenland. At its margins, the GIS flows into the ocean, discharging ice that contributes to rising sea level¹³⁴. At its surface, the Greenland ice sheet melts where seasonal snow cover and glacier ice contact the atmosphere. Surface melting is strongly seasonal, with melt concentrated in the summer months when the air temperature at the surface often exceeds 0°C¹³⁵. Melting generates water flow across the surface of the ice sheet that eventually enters the ocean as runoff. A portion of the flowing across the surface of Greenlandic glaciers flows to the base of the ice sheet through fractures and channels. The accumulation of water at the glacier bed increases the basal water pressure, resulting in a decrease in the contact area between the glacier and its bed, reducing basal friction and allowing faster glacier flow¹³⁶. As a result, the flow of Greenlandic glaciers, ice dynamical loss, and surface melting are, in fact, coupled processes that cannot be accurately modeled in isolation. Understanding the ice dynamics of the GIS and predicting its behavior in a warming

climate thus requires an understanding of sliding and hydrological processes that act at the base of the ice sheet.

Boreholes remain one of the only ways to directly measure depth-varying processes and structure. Extracting ice cores provides a 1-D structure of the ice fabric and material properties from within the borehole. Geophysical sensors can be deployed along the borehole, commonly used to measure seismic activity and pore pressure. Typical ice borehole experiments involve several sensors at most, given the logistical challenges of remote field operations and deploying instruments at depth. Recent experiments have involved the deployment of optical fiber that can be turned into dense arrays of geophysical sensors using new distributed optical sensing technology. This technique involves shooting laser light pulses into a fiber optic cable and interpreting the phase or frequency of backscattered light as related to strain (Distributed Strain Sensing - DSS), strain rate (Distributed Acoustic Sensing - DAS), and/or temperature (Distributed Temperature Sensing - DTS). Several recent experiments involved either measurements in Greenland^{137,138,139}, Antarctica^{140,141,142}, and mountain glaciers^{143,144}.

This study explores the 3-day continuous DAS recording from July 6, 2019 to July 9, 2019 at Store Glacier in West Greenland. The field experiment involved several boreholes with bottom pressure sensors, one borehole with DAS and DTS, and the acquisition of several hammer shots for geophysical imaging^{137,138,139}. Figure 4.1 displays the field areas, geophysical sensing configurations, and a schematic representation of the fiber and interrogator sensing geometry.

This study focuses on the continuous recordings made by the borehole DAS system. We first discuss and interpret the direct observations made from amplitude measurements in light of the fluctuations in bottom pore pressure and surface velocity revealed by previous studies. Second, we present the first observations that reveal the properties of S waves traveling at the bottom of the ice sheet. Third, we find persistent sources of seismic waves at the bottom of the ice sheet, which we interpret as hydrological and sliding noise.

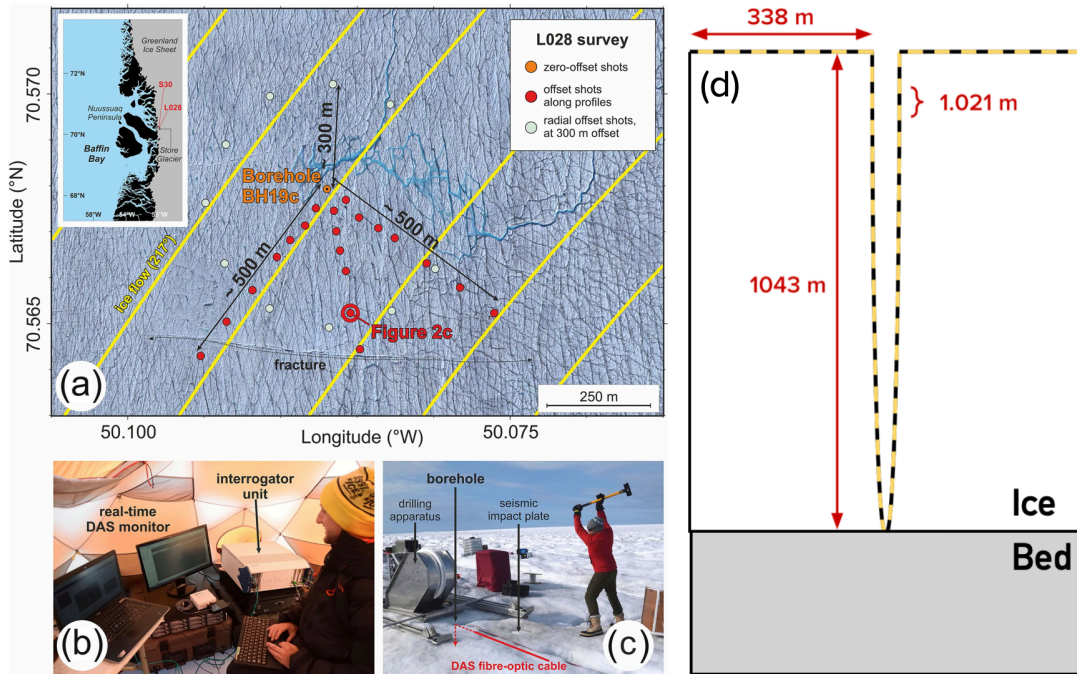


Figure 4.1: Study site and distributed acoustic sensing (DAS) deployment. (a) Surface of Store Glacier and the location of the borehole used to deploy fiber optic cable for DAS. Note the surface water flow that drains through a moulin near the borehole. Red dots show active source shot locations in a previous study¹³⁹. The inset shows the location of Store Glacier within West Greenland. (b) On-site interrogator and data analysis station. (c) Machinery used to drill borehole BH19c and carry out active source seismic analysis in Booth et al., 2020¹³⁹. (d) Geometry of fiber optic cable, including lateral distance on the surface, vertical extent, and channel spacing. Figure used with permission

4.1 OBSERVATIONS

The DAS data is recorded with a Silixa iDASTM interrogator, with a gauge length of 10 m, a channel spacing of 1.021. The geometry of the array is interpreted and shown in Figure 4.1. The sampling rate changed a day after the start of the experiment from 1000 Hz to 4000 Hz. To analyze the recorded DAS data and infer the source of recorded signals, we analyze the spatiotemporal distribution of the ambient seismic field. For a signal with n samples, we define the Root-Mean-Square (RMS) amplitude as:

$$x_{RMS} = \sqrt{\frac{1}{n}(x_1^2 + x_2^2 + \dots + x_n^2)}$$

First, we filter the data between 1 and 100 Hz. Then, we compute the RMS of each 30 s time window and at each channel. This procedure yields a representation of the average signal strength as a function of space and time. The result of our RMS calculation is shown in Figure 4.2. At the beginning of the signals, the upper few hundred meters of the borehole are seismically loud. This near-surface noise is likely generated by human activity, electrical noise, and mechanical noise in the nearby field camp. These signals appear extremely well bounded in depth and in time. Such signals are unlikely to be generated by natural phenomena, and we therefore do not seek to interpret the physical mechanisms that generated such noise. However, a few significant features are readily identified in the spatiotemporal distribution of noise, which we discuss in the sections below.

4.1.1 THE SOUNDS OF FREEZING ICE

At the start of the deployment on July 6, the signal strength is elevated at around 600 m depth, indicating a region where the cable is experiencing an elevated strain rate. Over the next three days, this noise source migrates from 600 m in both directions of the cable (orange line in Figure 4.2).

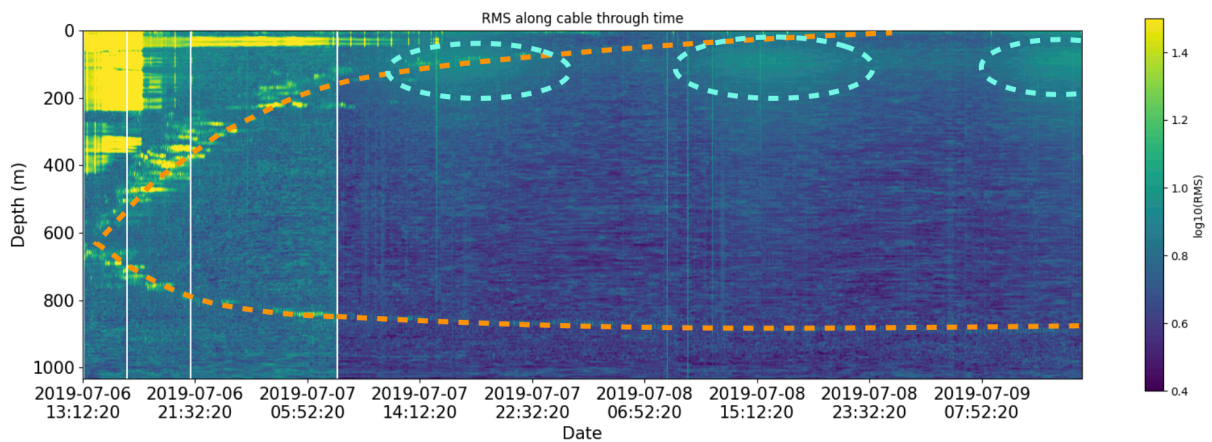


Figure 4.2: RMS of noise recorded by DAS deployment as a function of channel depth. The RMS was computed for each 30 s time window in the dataset at each channel along the cable on the frequency band 1-100 Hz. The orange dotted line shows the inferred location of the borehole freezing front. The blue dotted circles show periods of elevated near-surface noise generated by surface water flow and percolation due to diurnal surface melt.

While the upward-migrating noise source reaches the surface by the end of the deployment, the downward-migrating noise source stabilizes at around 850 m depth. Distributed temperature sensing (DTS) data collected at BH19c over the same period of time records that the location of the phase transition closely tracks the position through time of the migrating signal we observe in the DAS data¹³⁷. From this observation, we infer that the fiber optic cable experiences an elevated strain rate at the location of the phase change from liquid water to solid ice within the borehole.

Two mechanisms may account for straining at the freezing front. First, because ice has a lower density than water, freezing increases the volume of material within the confined borehole. As the water in the borehole freezes, the cable is therefore subjected to radially uniform compression that generates axial strain according to the Poisson's ratio of the optical fiber. This strain is applied on a timescale related to the duration of the phase change and remains constant in magnitude once freezing is complete, resulting in a strain rate signal that moves through space synchronously with the phase change front as the borehole refreezes. Second, any sloshing within the water-filled regions of the borehole will generate pressure fluctuations at the edges of the frozen region of the borehole.

Because the boundary between frozen ice and liquid water filling the borehole coincides spatially with the freezing front, strains generated by sloshing are expected to migrate with the freezing front. Presently, we cannot rule out either mechanism, and both effects may contribute to the observed strain rate signal.

4.1.2 ENGLACIER HYDROLOGY

We observe noise in the upper 200 m of the cable that fluctuates in signal strength diurnally. Throughout each day, the amplitude of the signal gradually increases, reaching maximum strength at local hours 16:00 before decaying. Figure 4.2 shows the spatiotemporal signal of the near-surface diurnal signal (indicated by the light blue ovals). Spatially, the signal achieves maximum strength at about 100 m depth and subsequently decays with increasing depth. We hypothesize that this near-surface signal is generated by the downward flow of surface meltwater through the glacier. In general, Greenlandic glaciers experience peak surface melt in the afternoon, consistent with the timing of the noise recorded in the DAS data. As the glacier surface experiences melting, meltwater flows downslope across the glacier surface, eventually reaching moulines and fractures that allow downward flow into the glacier. Previous borehole measurements indicate that crevasse penetration to depths of a few hundred meters is pervasive on Store Glacier¹⁴⁵, providing a route for surface meltwater to flow to depths consistent with the location of maximum diurnal signal strength. Furthermore, the borehole study site is nearby active surface channels, two moulines, and a fracture system implicated in the drainage of a supraglacial lake, indicating that vertical water transport readily occurs in this area of Store Glacier^{137,146}.

To further explore the hypothesis that the recorded near-surface noise is hydrological in origin, we explore the relationship between surface noise, basal water pressure, and surface velocity. However, a previous study found that borehole BH19c, in which the DAS cable was deployed, terminates in a hydrologically-isolated cavity with basal water pressure that is out-of-phase with ice flow velocity

and water pressure within the effective subglacial hydrological system¹³⁸. We therefore compare the phase of the diurnal RMS signal to basal water pressure recorded at nearby borehole BH19e and GNSS-derived surface velocity data from a previous study of the same study site at roughly the same time period¹³⁸. Another limitation is that surface velocity and water pressure at BH19e were not recorded until after the three-day DAS deployment had concluded. We account for this by comparing the RMS signal to pressure and velocity data recorded 24 days later and aligned based on the time of day, assuming that our observed RMS is diurnal outside of the recording window. Figure 4.3 displays the mean RMS through time as a function of depth with basal water pressure recorded at BH19e and GNSS-derived surface velocity.

Because the RMS data are from a different time period than the pressure and velocity data, we interpret only the relationships between the phase of the signals rather than the precise relationship between signal amplitudes or any fine-scale features of the data. First, basal water pressure is aligned in phase with ice flow velocity, consistent with the standard theory that elevated bed pressure allows faster glacier sliding¹³⁶ and with previous work at Store Glacier¹³⁸. Second, both basal water pressure and flow velocity are aligned with the diurnal RMS signal with a lag of about four hours. Because basal water pressure is expected to reach a maximum once surface meltwater has fully percolated downward through the glacier, we hypothesize that the four-hour lag between basal pressure and the diurnal RMS signal is related to the timescale of vertical water transport. Because the crevasses that cover Store Glacier penetrate a few hundred meters¹⁴⁵ before closure, water can quickly flow to the base of crevasse networks, consistent with elevated RMS at a depth of around 100 m a few hours before peak basal water pressure. However, once pooled at the bottom of these networks of crevasses, water must flow through the remaining 900 m of the glacier's thickness, likely through a more distributed network of far narrower conduits. This results in a slower flow through the majority of the glacier's thickness, explaining the observed lag between the diurnal RMS signal and basal water pressure and the reduced signal amplitude at depths below a few hundred meters.

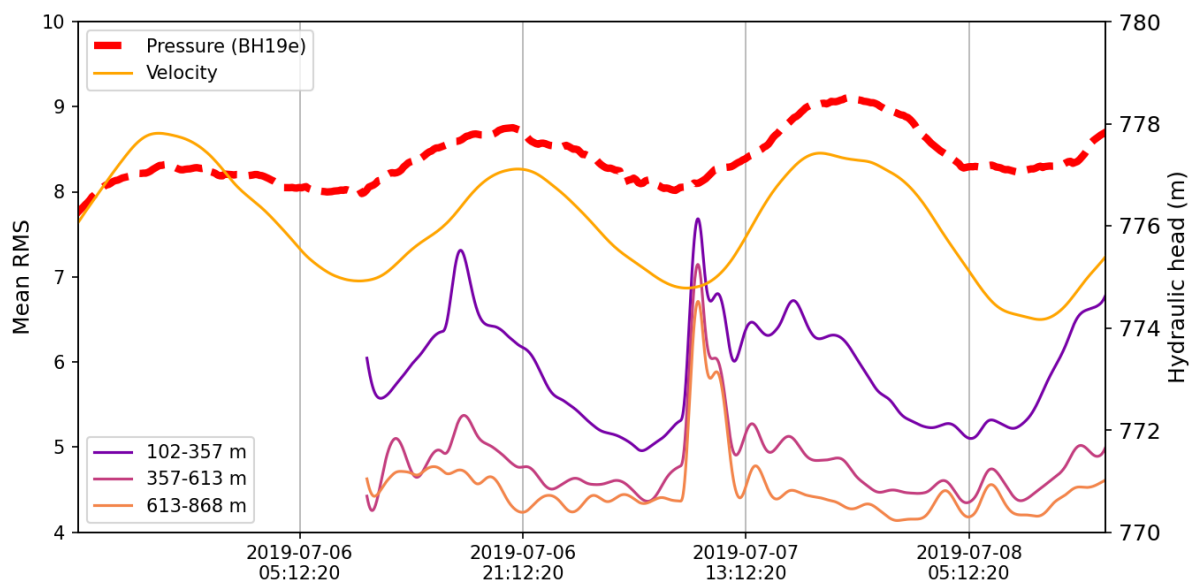


Figure 4.3: Correlation of surface noise, basal water pressure, and surface ice flow velocity. Red dotted line shows basal water pressure recorded at a nearby borehole (BH19e). The gold line shows diurnal fluctuation in ice flow velocity. Note the correspondence in phase between basal water pressure and ice flow velocity. Absolute flow velocities are not shown for simplicity. Purple, crimson, and orange lines show the average noise RMS recorded by channels in the depth bins in the legend. Peak amplitudes in seismic noise are recorded each day in the mid-afternoon when the diurnal surface melt is highest. Maximum basal water pressure and fastest flow velocities are recorded about 4 hours after each maximum in seismic noise. Note that surface flow velocity and basal pressure at BH19e were not recorded during the DAS deployment. The data displayed here, recorded 24 days later, are properly aligned in reference to time-of-day and are emblematic of typical diurnal patterns in basal water pressure and flow velocity.

We therefore infer that the infiltration of surface meltwater to the base of Store Glacier occurs on timescales of roughly four hours, consistent with previous studies that observe englacial water transport over timescales on the order of hours^{147,148,149}.

4.1.3 BASAL SOUNDSCAPE

To further interrogate the recorded DAS data and its relationship to glacier basal dynamics, we construct a spectrogram using the average trace of ten channels near the glacier bed. We find two main

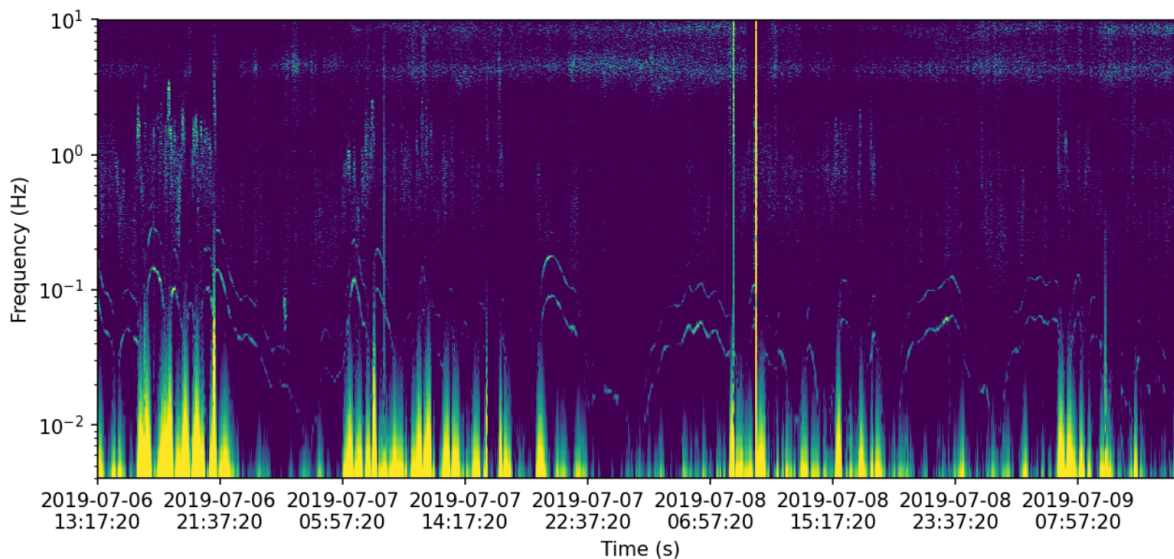


Figure 4.4: Spectrogram of data recorded by basal DAS channels. The spectrogram was computed using the average trace of data recorded between 1025 m and 1035 m depth. Note the presence of gliding lines between 0.01 and 0.5 Hz and elevated signal power below 0.01 Hz.

characteristics of the acoustic signals at the base of the glaciers. Figure 4.4 shows that the basal channels record gliding tremor lines between 0.01 Hz and 0.5 Hz and low-frequency noise with peak power below about 0.01 Hz. The power and frequency of both signals vary through time, with no clear connection to each other or the diurnally-periodic surface noise, basal water pressure, and ice flow velocity signals. While gliding lines are often indicative of tremor generated by stick-slip basal sliding^{150,151}, the lack of clear repeating icequakes supports an alternative source. Until more comprehensive analysis can be carried out, the exact mechanisms of basal noise generation and the source of gliding lines remain elusive.

4.2 ICE STRUCTURE AND DYNAMICS USING AMBIENT NOISE CROSS CORRELATION

The cross-correlation of the ambient seismic field can reveal the elastic properties of the material between channels^{152,153} (i.e., the ice column in this case) and about the sources that excited the co-

herence wavefield¹⁵⁴. No investigation has yet had the opportunity to image the full ice thickness with such dense measurements. To analyze the propagation of seismic waves through the thickness of Store Glacier, we carry out cross correlation of the DAS dataset. The DAS data contains 2688 channels and over 8.5 TB of raw data. We developed a fast workflow that we describe below. In seismology, the cross-correlation of ambient noise is used to interrogate the material properties and structure of the medium between two seismic stations. We compute the cross-correlation between data recorded by each channel of the cable using the algorithm described below.

4.2.1 CROSS CORRELATION ALGORITHM

We develop a new workflow that is highly scalable and fast using the computing language Julia and preliminary work on ambient noise cross-correlations^{155,156}. The efficiency of workflow is ensured by executing the majority of processing and computation on graphical processing units (GPU). We adapt the core functionality of this software to the specific array configuration of the DAS borehole array (Fig. 4.1). The data is organized in 30 s long SEG-Y files.

We first perform data pre-processing. During the first day of the deployment, each file was recorded at a sampling rate of $f_s = 1000$ Hz. During the second two days of the deployment, each file was recorded at a sampling rate of $f_s = 4000$ Hz. To improve the speed of the process, we downsample all data to the sampling rate $f_s = 400$ Hz before filtering between 1 Hz and 200 Hz. We first detrend, demean, bandpass filter between 1 and 200 Hz, and taper the data to avoid artifacts in the Fourier transform.

DAS seismic data tends to have a coherent, instantaneous noise that all channels sense, which is an artifact typical to DAS interrogators. We filter this coherent noise of infinite apparent wavespeed using an F-K filter to only select waves that travel between 1000 /s and 4000 m/s, which are the expected range between surface waves and body waves. We FK filter the data by first taking the Fourier transform in time and in space (i.e., along the axis defined by each time sample and the axis defined

by each spatial channel) for each leg of the borehole separately. Then, regions of the transformed data matrix that correspond to phase velocities outside the desired range (1000-4000 m/s) are set to zero. Gaussian filtering is then applied to smooth the transition between nonzero and zero-valued regions of the data matrix and thereby avoid producing artifacts associated with taking the inverse Fourier transform of a discontinuous function. Finally, we take the inverse Fourier transform along both axes to return the FK-filtered data to the time and space domain.

Then, we use the typical noise pre-processing. There are two types of normalization to improve the amplitude of the coherent waves. First, the frequency-domain normalization method seeks to whiten the spectra of data (i.e. make the amplitude spectra of recorded noise flat with respect to frequency). It has been shown to improve the quality of ambient noise cross-correlation functions by reducing the dominance of the frequencies associated with the ocean-generated microseism¹⁵³. Second, the time-domain normalization has been shown to improve the quality of ambient noise cross-correlation functions by reducing or removing entirely the contribution of high amplitude signals in the input data like local seismic events or teleseismic wave arrivals¹⁵³. We use the one-bit normalization, which preserves only the sign of the data. In this case, the emergence of coherent signals in the cross-correlation function is dominated by constructive interference of recorded waves and any influence of strong amplitude events is removed.

After the preprocessing, we finally compute the cross-correlation functions for every pair of channels in the dataset. Before correlation, we trim the data into 10-second long windows in order to compute three cross-correlations per file. Short windows and further stacking has been shown to improve the signal-to-noise ratio of the cross-correlations. To efficiently compute correlation functions, we take the Fourier transform of the entire data matrix along the time axis. Then, we multiply the complex conjugate of the transformed data from a single channel (c_i) by the transformed data from every other channel ($c_{i+1} \dots c_n$) and take the inverse Fourier transform of their products to yield the correlation functions corresponding to the channel pairs $[c_i, c_{i+1}]$, $[c_i, c_{i+2}]$, $\dots [c_i, c_n]$.

This procedure is repeated for the transformed data from each channel to yield a matrix containing the correlation functions for each channel pair along the cable. We then linearly stack all of the cross-correlations over time to form a 3-day average correlation. Finally, we spatially stack cross-correlations using a novel stacking algorithm described below.

4.2.2 SPATIAL STACKING ALGORITHM

To improve the signal emergence and coherence of the resulting correlation functions, we stack the correlation functions spatially using the correspondence between channel pairs on the downgoing and upgoing portions of the cable. Because the cable is deployed in a U-shaped geometry, any given channel on the downgoing cable is aligned spatially with a particular channel on the upgoing cable. For a U-shaped cable with n channels in the borehole, channels c_1 through $c_{n/2}$ represent the downgoing portion of cable and channels $c_{n/2+1}$ through channels c_n represent the upgoing portion of the cable. Therefore, channels $c_1, c_2, c_3, \dots, c_{n/2}$ are each respectively aligned in depth with channels $c_n, c_{n-1}, c_{n-2}, \dots, c_{n/2+1}$. In addition, cross-correlation functions computed using channel pairs on the downgoing cable are directly analogous to cross-correlation functions computed using the corresponding pairs on the upgoing cable. For instance, the correlation function computed using channel pair $[c_1, c_2]$ represents the same wave propagation path as the correlation function computed using channel pair $[c_n, c_{n-1}]$. These channel pairs are depicted in Figure 4.5 as "Leg 1" and "Leg 2" respectively. Correlation functions computed using pairs of channels that include one channel from each portion of the cable are similarly analogous. For instance, the correlation function computed using channel pair $[c_1, c_{n-1}]$ represents the same wave propagation path as the correlation function computed using channel pair $[c_2, c_n]$. These channel pairs are depicted in Figure 4.5 as "Leg 3" and "Leg 4" respectively. To exploit this feature of the deployment, we stack the correlation functions computed using analogous channel pairs as shown in the schematic Figure 4.5 by extracting and summing the correlation functions corresponding to each leg from the overall matrix of correlation

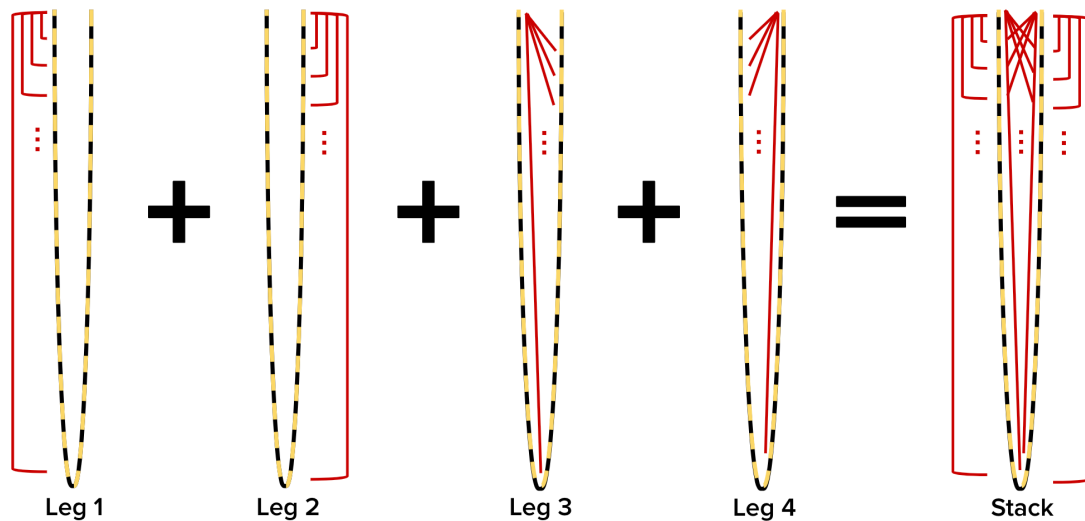


Figure 4.5: Schematic of cross-correlation function stacking algorithm. To improve the signal-to-noise ratio, correlation functions computed using corresponding pairs of stations from each portion of the cable were summed. Leg 1 correlation functions were computed using each pair of stations on the downgoing portion of the cable. Leg 2 correlation functions were computed using each pair of stations on the upgoing portion of the cable. Leg 3 and leg 4 correlation functions were computed using pairs of stations from the downgoing and upgoing portions of the cable. The overall stack is retrieved by summing the corresponding correlation functions from each leg.

functions.

4.2.3 CROSS-CORRELATION WAVEFIELD

We now briefly describe the cross-correlation wavefield. Given its complexity and richness, further analysis will help discriminate and interpret all the features of the recovered wavefield. We show the correlation wavefield from a channel near the top of the borehole in Figure 4.6 and from channels at a variety of depths in Figure 4.7. We note that correlation functions computed in reference to basal channel exhibit conjugate symmetry with correlation functions computed in reference to surface channel (Figure 4.6 and Figure 4.7d).

The first transformative result of our analysis is the ability to detect variations in P and S wave speed throughout the ice column without the need for an active source. We find that wave speed

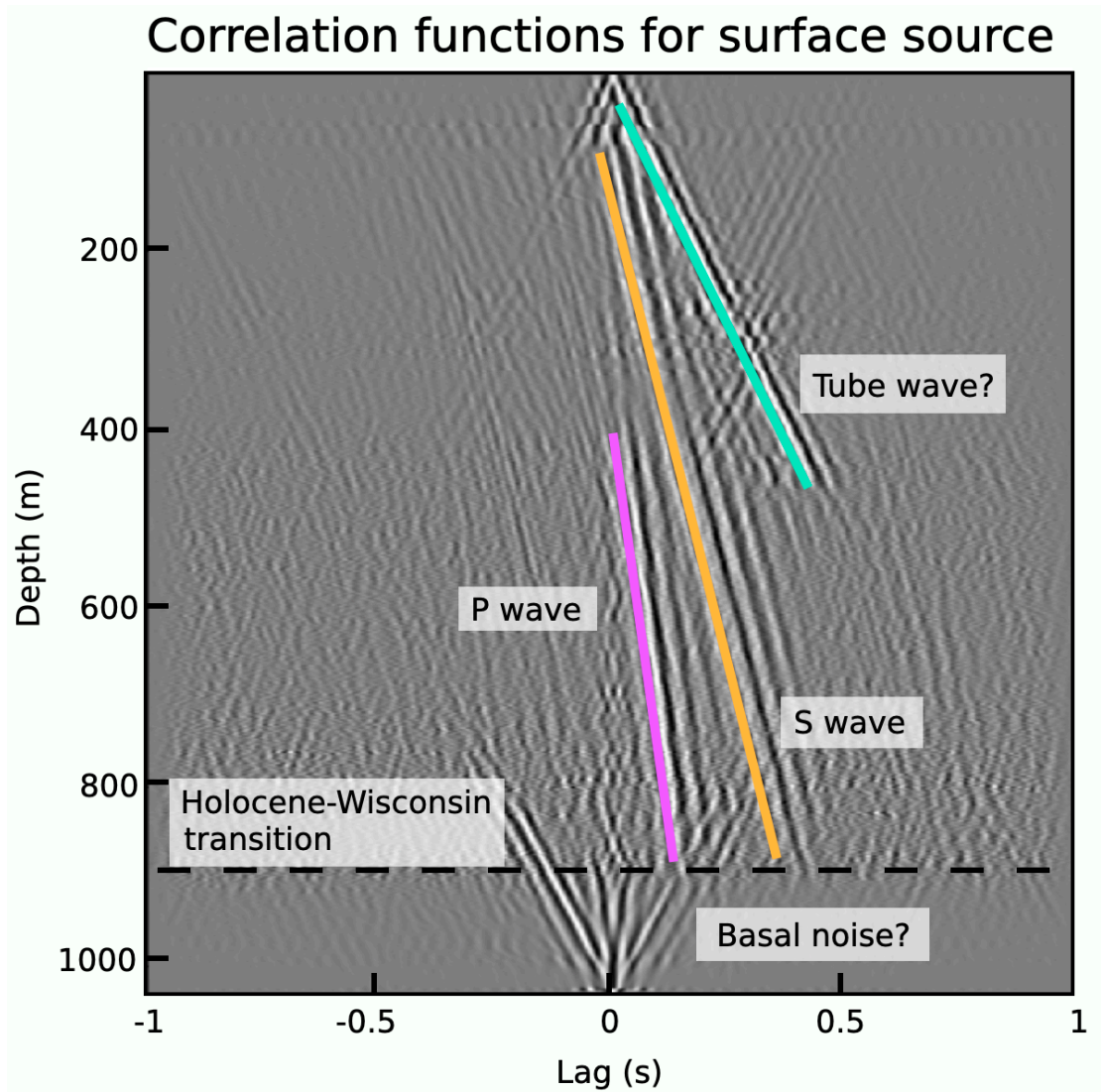


Figure 4.6: Stacked correlation functions for a virtual source near the glacier surface. Displayed correlation functions computed in reference to a channel at the top of the borehole and filtered between 1 and 50 Hz. P and S wave are shown by the purple and orange lines respectively. Anomalous slow phase, inferred to be a borehole tube wave, is shown in blue. The dotted line shows the depth of the transition between Holocene and Wisconsin ice.

are relatively uniform, consistent with wave speeds determined by the active survey¹³⁹. We find a P-wave speed of just below 4000 m/s and S-wave speed 1860 m/s approximately from visual inspection of the moveout. We also observe a slower phase propagating at 1000 m/s, which we interpret as an interference wave traveling along the borehole wall¹⁵⁷, colloquially referred to as a "tube wave".

Second, the correlation wavefield reveals information about the structure of the glacier with depth. We observe wave reflections at depths ranging from 300 m to 450 m, indicating structures that reflect and scatter incoming waves. This set of structures coincide in depth with the decay in hydrological noise, which we believe is related to the closure of crevasses at depths of a few hundred meters¹⁴⁵. We therefore propose that the observed seismic wave reflections at $\sim 300\text{-}450$ m depth are generated when seismic waves are incident on the tips of vertical glacier crevasses. A second well-localized reflector is visible at 900 m depth. Below this depth, noise propagating from the surface is significantly reduced in amplitude due to the reduction in transmitted seismic energy associated with reflections. Previous work in the region localized the transition between Holocene age ice to older, Wisconsin age ice to about 85% of the ice thickness, or a depth of about 890 m^{139,158,159}. We therefore interpret the reflector at 900 m as the Holocene-Wisconsin transition, and conclude that ambient noise correlation of DAS data is capable of clearly resolving ice structure.

Third, correlation functions near the base of the glacier achieve high values around a lag of zero seconds, indicating that noise is propagating upward from the glacier bed. While much of the apparent basally-generated wave energy propagates at the same velocity as the interference phases generated at the borehole surface, we observe basally-generated signals that propagate at the P-wave speed, indicating a source of elastic wave radiation at the base. Possible mechanisms include glacier sliding or subglacial water flow. The basal noise source may also be related to the elevated low frequency noise and gliding spectral lines near the borehole base seen in Figure 4.4. Further work will seek to precisely localize the source of the basal noise in space and time and to determine the mechanism generating noise at the glacier bed.

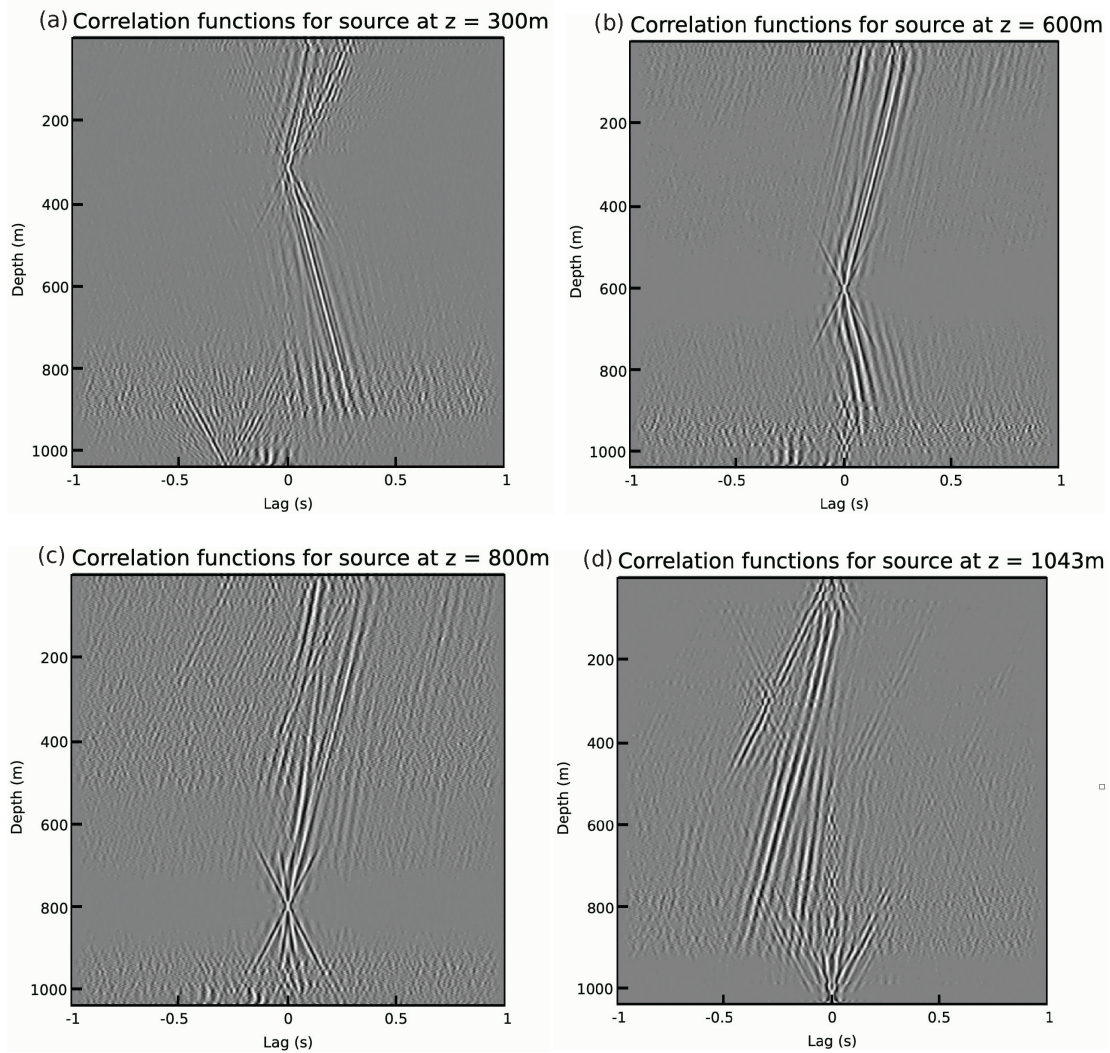


Figure 4.7: Stacked correlation functions for virtual sources at depth. (a) Same as Figure 4.6 but displayed correlation functions were computed in reference to channel at 300 m depth. (b) Correlation functions computed in reference to channel at 600 m depth. (c) Correlation functions computed in reference to a channel at 800 m depth. (d) Correlation functions computed in reference to channel at glacier base (1043 m depth). Note the conjugate symmetry between correlation functions computed in reference to surface and basal channels.

4.3 CONCLUSIONS

By exploring the diverse range of signals and processes recorded at Store Glacier, we demonstrate the incredible potential of borehole DAS to study glacier dynamics. No other existing methods are capable of recording data at such high resolution in both space and time. As shown here, DAS data can be used in a variety of analyses ranging from simple analysis of the spatiotemporal distribution of noise to more complex methods like cross-correlation of ambient noise. From only three days of data, we constrain ice structure, hydrological processes, borehole freezing dynamics, and potentially basal sliding dynamics. Furthermore, additional information likely remains encoded in this rich dataset to be uncovered in further investigation. We conclude by noting that the preliminary work presented here serves merely as the beginnings of a more thorough investigation that will continue to explore the frontiers of glacier borehole DAS.

5

Conclusion

I CONCLUDE BY REVISITING THE QUESTIONS POSED AT THE BEGINNING OF THE WORK. Are rifts sensitive to environmental stresses, or are they controlled solely by the background ice flow dynamics that drive ice shelf extension? Our analysis of icequakes generated at a stagnant rift in the Ross ice shelf shows that fracture at rifts is sensitive to stresses that arise from extremely cold air temperatures and from tidal displacements of the ice shelf. Our analysis of flexural gravity waves generated by rift propagation in Pine Island Glacier ice shelf shows that the large-scale rift propagation responds to changes in ice flow dynamics that are driven by elevated ocean melt. While environmental stresses may not be the dominant mechanism driving rift propagation in all cases, we conclude that environmental stresses certainly can play an important role in controlling the timing and rate of rifting.

How do the ice shelves move and flex in response to rifting? At Pine Island Glacier, gradual rift propagation generates flexural gravity waves that propagate tens of kilometers across the ice shelf. Our work shows that rapid rifting on lengthscales of tens of kilometers can excite ice shelf resonance that lasts for hours after fracture quiescence, causing bobbing and flexure of the entire ice shelf. We conclude based on our observations that flexural gravity wave generation is the dominant elastic response of ice shelves to rifting.

How quickly can rifts propagate? Do rifts propagate through brittle fracture? Do rifts present a mechanism of rapid ice shelf collapse and loss of buttressing? We observe 10.5 km of rift propagation at a rate of 3.5 m/s, the fastest known episode of rift propagation. Despite being two orders of magnitude slower than the theoretical speed limit of opening-mode linear elastic fractures, such a rate can only be explained by brittle deformation. This indicates that rifting certainly cannot be modeled as a viscous or plastic deformational process in all cases. While faster propagation rates may be possible in the presence of extreme tensional stress, our observations and modeling suggest that the maximum speed of rift propagation is limited by hydrodynamic processes. Nonetheless, we conclude that tens of kilometers of rift propagation can occur in a matter of minutes. This suggests

that rifting cannot be thought of simply as a steady-state process that maintains the position of the calving front. Instead, rifting must be evaluated a dynamic process that is capable of rapidly causing iceberg calving, ice front retreat, and loss of ice shelf buttressing.

It is my hope that future studies of ice shelves continue to delve further into the nature of rifts to better assess their impact as the Antarctic Ice Sheet continues to evolve under increasingly severe climate forcing. Indeed, the propagation dynamics of rifts may prove to play a significant role in determining the rate of future ice loss and sea level rise. In this thesis, I have done my best to provide knowledge that will help humanity prepare, adapt, and overcome the global challenge of anthropogenic climate change.



Sensitivity of Icequake Deconvolution

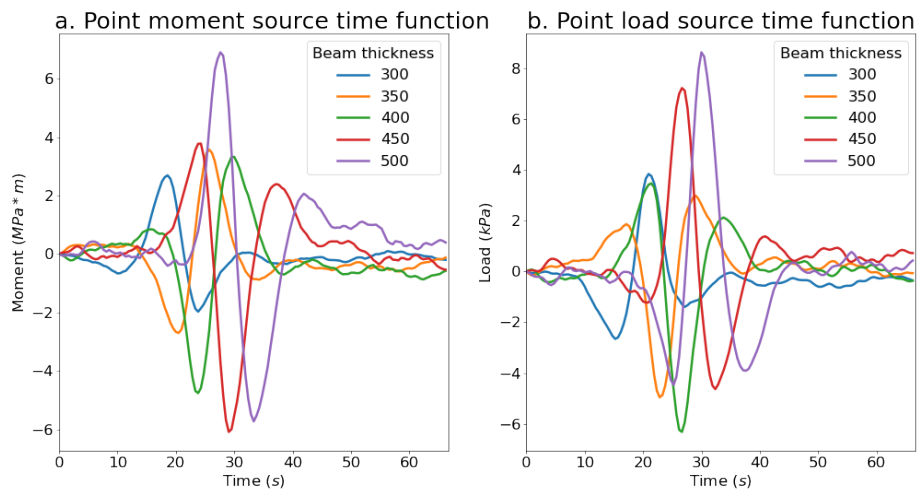


Figure A.1: Sensitivity of rift tip source time function deconvolution to modeled ice thickness. (a) Sensitivity of point moment source time functions. **(b)** Sensitivity of point load source time functions. Modeled beam thicknesses are shown in the legend. Source time functions generally have larger amplitude and longer duration for thicker beams, because larger forcing is required to induce a given displacement for a more rigid beam. Flexural rigidity, the parameter that governs flexure, is a function of thickness.

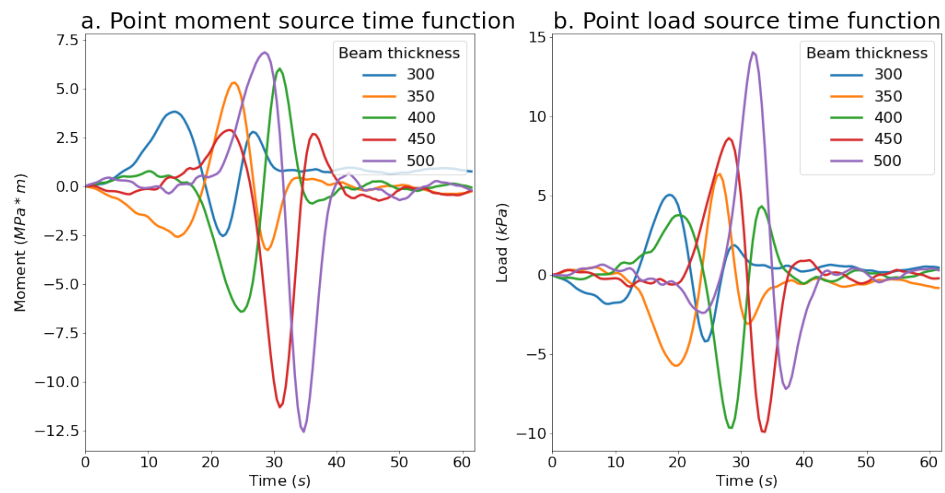


Figure A.2: Sensitivity of rift/margin source time function deconvolution to modeled ice thickness. (a) Sensitivity of point moment source time functions. **(b)** Sensitivity of point load source time functions. Modeled beam thicknesses are shown in the legend. Source time functions generally have larger amplitude and longer duration for thicker beams, because larger forcing is required to induce a given displacement for a more rigid beam. Flexural rigidity, the parameter that governs flexure, is a function of thickness.

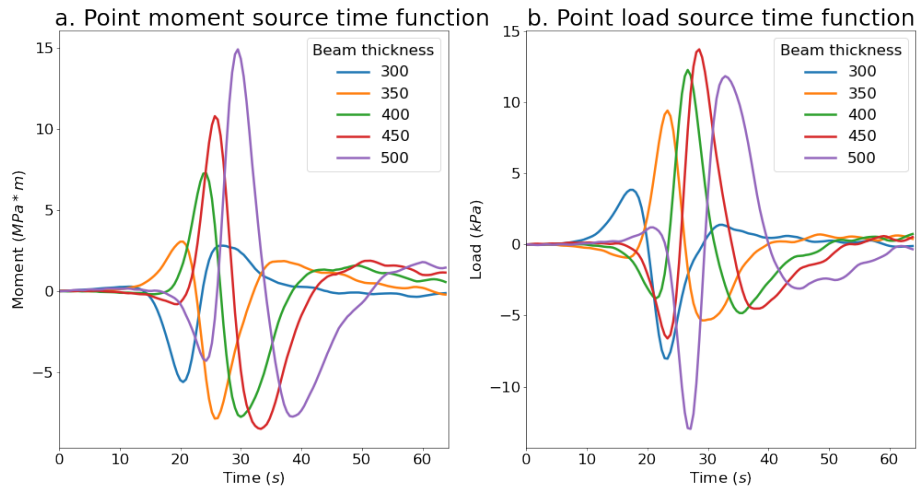


Figure A.3: Sensitivity of margin source time function deconvolution to modeled ice thickness. (a) Sensitivity of point moment source time functions. **(b)** Sensitivity of point load source time functions. Modeled beam thicknesses are shown in the legend. Source time functions generally have larger amplitude and longer duration for thicker beams, because larger forcing is required to induce a given displacement for a more rigid beam. Flexural rigidity, the parameter that governs flexure, is a function of thickness.

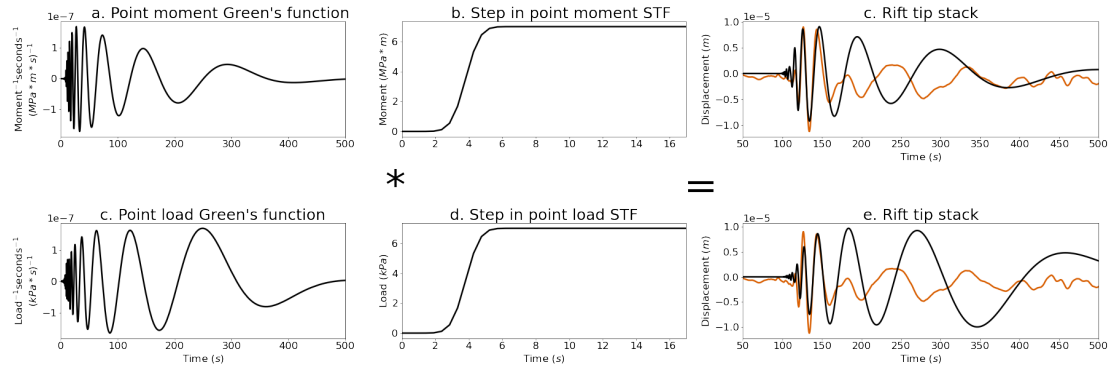


Figure A.4: Modeled rift tip Green's function convolved with step source time function. The resulting modeled displacements, shown in black, have a longer decay and larger amplitude low-frequency displacements than the rift tip stack, shown in orange, for both bending moment and point load sources.

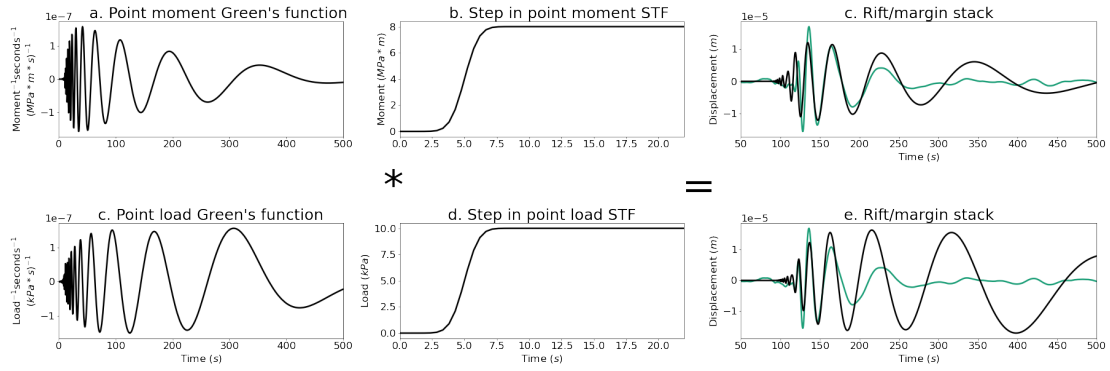


Figure A.5: Modeled rift/margin Green's function convolved with step source time function. The resulting modeled displacements, shown in black, have a longer decay and larger amplitude low-frequency displacements than the rift/margin stack, shown in green, for both bending moment and point load sources.

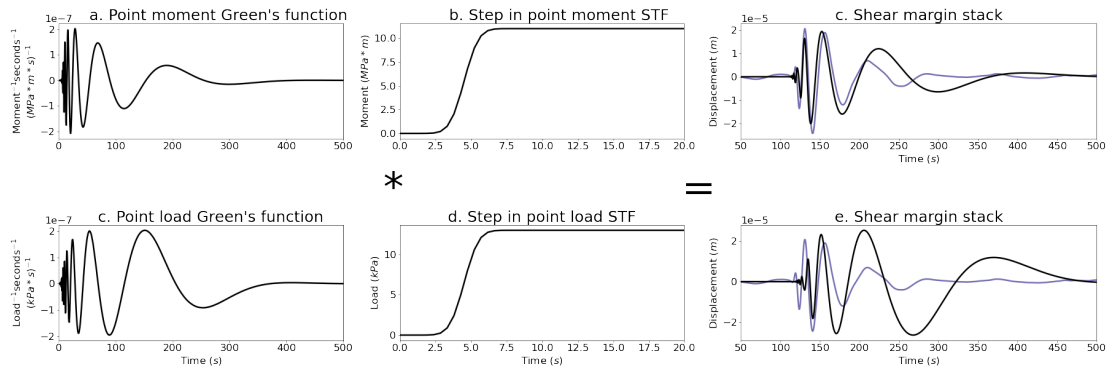


Figure A.6: Modeled shear margin Green's function convolved with step source time function. The resulting modeled displacements, shown in black, have a longer decay and larger amplitude low-frequency displacements than the shear margin stack, shown in purple, for both bending moment and point load sources. The modeled displacements arising from an applied bending moment are relatively similar to the shear margin stack, but the results of deconvolution do not support the hypothesis that the observations were generated by a step forcing in bending moment.

B

Sensitivity of Ocean Coupled Fracture

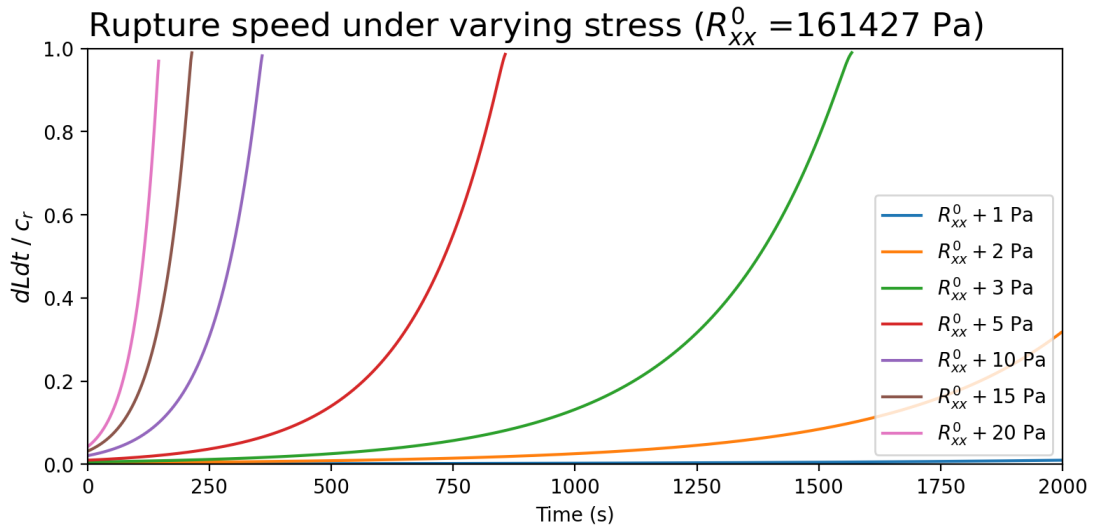


Figure B.1: Sensitivity of ocean-coupled fracture model to magnitude of stress. Increasing the magnitude of applied stress strongly increases the average propagation rate and causes propagation to reach the Rayleigh wave speed c_r more quickly. Baseline stress R_{xx}^0 is computed by finding the magnitude of stress required to initiate rift propagation for the observed initial rift geometry. In each simulation, the R_{xx}^0 is perturbed by the additional stress shown in the legend. All other parameters are held fixed across simulations.

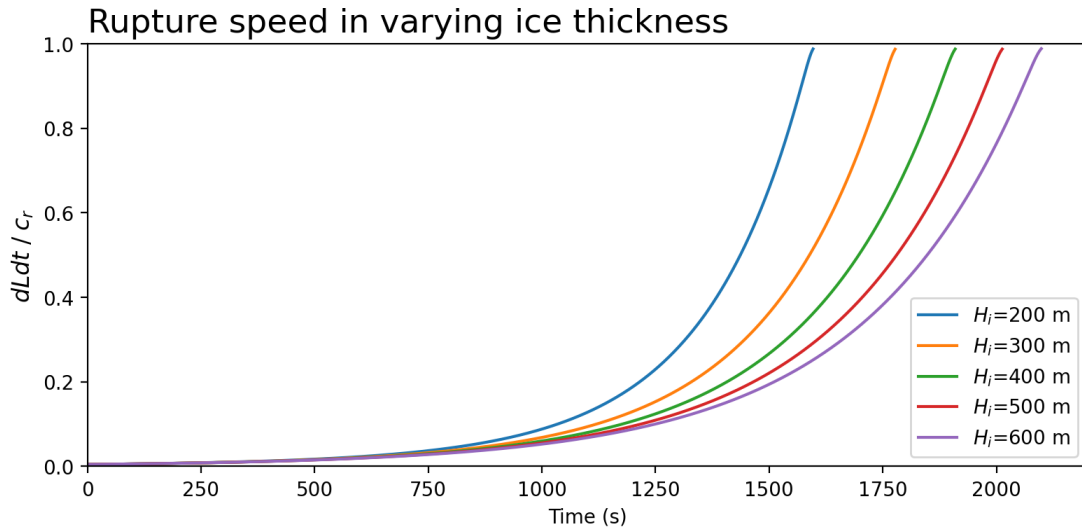


Figure B.2: Sensitivity of ocean-coupled fracture model to ice thickness. Increasing the ice thickness decreases the average propagation rate and causes propagation to reach the Rayleigh wave speed c_r more slowly. All other parameters are held fixed across simulations.

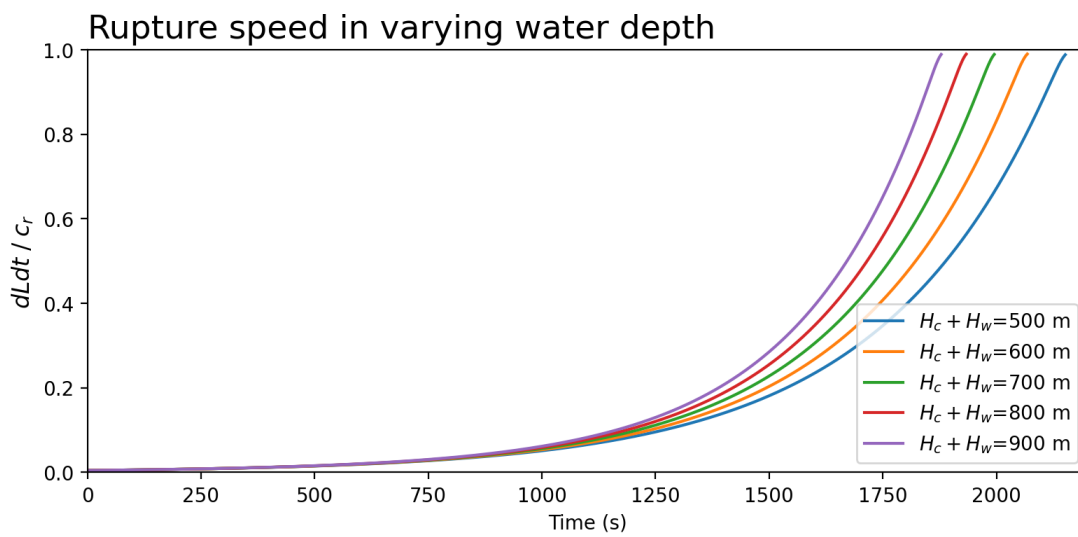


Figure B.3: Sensitivity of ocean-coupled fracture model to water depth. Increasing the total water depth $H_c + H_w$ increases the average propagation rate and causes propagation to reach the Rayleigh wave speed c_r more quickly. All other parameters are held fixed across simulations.

References

- [1] Bulthuis, K., Arnst, M., Sun, S., & Pattyn, F. (2019). Uncertainty quantification of the multi-centennial response of the Antarctic ice sheet to climate change. *The Cryosphere*, 13(4), 1349–1380.
- [2] Bakker, A. M. R., Wong, T. E., Ruckert, K. L., & Keller, K. (2017). Sea-level projections representing the deeply uncertain contribution of the West Antarctic ice sheet. *Scientific Reports*, 7(1), 3880.
- [3] Rignot, E., Mouginot, J., Scheuchl, B., van den Broeke, M., van Wessem, M. J., & Morlighem, M. (2019). Four decades of antarctic ice sheet mass balance from 1979 to 2017. *Proceedings of the National Academy of Sciences*, 116(4), 1095–1103.
- [4] Noerdlinger, P. D. & Brower, K. R. (2007). The melting of floating ice raises the ocean level. *Geophysical Journal International*, 170(1), 145–150.
- [5] Budd, W. (1966). The dynamics of the amery ice shelf. *Journal of glaciology*, 6(45), 335–358.
- [6] Thomas, R. H. (1979). The dynamics of marine ice sheets. *Journal of Glaciology*, 24(90), 167–177.
- [7] Thomas, R. H. & MacAyeal, D. R. (1982). Derived characteristics of the ross ice shelf, antarctica. *Journal of Glaciology*, 28(100), 397–412.
- [8] Scambos, T. A., Bohlander, J. A., Shuman, C. A., & Skvarca, P. (2004). Glacier acceleration and thinning after ice shelf collapse in the larsen b embayment, antarctica. *Geophysical Research Letters*, 31(18).
- [9] Rignot, E., Casassa, G., Gogineni, P., Krabill, W., Rivera, A., & Thomas, R. (2004). Accelerated ice discharge from the antarctic peninsula following the collapse of larsen b ice shelf. *Geophysical research letters*, 31(18).
- [10] Pan, L., Powell, E. M., Latychev, K., Mitrovica, J. X., Creveling, J. R., Gomez, N., Hoggard, M. J., & Clark, P. U. (2021). Rapid postglacial rebound amplifies global sea level rise following west antarctic ice sheet collapse. *Science Advances*, 7(18), eabf7787.

- [11] Bamber, J. L., Riva, R. E. M., Vermeersen, B. L. A., & LeBrocq, A. M. (2009). Reassessment of the Potential Sea-Level Rise from a Collapse of the West Antarctic Ice Sheet. *Science*, 324(5929), 901–903. _eprint: <https://www.science.org/doi/pdf/10.1126/science.1169335>.
- [12] Mouginot, J., Rignot, E., & Scheuchl, B. (2014). Sustained increase in ice discharge from the amundsen sea embayment, west antarctica, from 1973 to 2013. *Geophysical Research Letters*, 41(5), 1576–1584.
- [13] Weertman, J. (1974). Stability of the junction of an ice sheet and an ice shelf. *Journal of Glaciology*, 13(67), 3–11.
- [14] Hughes, T. (1973). Is the west antarctic ice sheet disintegrating? *Journal of Geophysical Research (1896-1977)*, 78(33), 7884–7910.
- [15] Hughes, T. J. (1981). The weak underbelly of the west antarctic ice sheet. *Journal of Glaciology*, 27(97), 518–525.
- [16] Gudmundsson, G. H. (2013). Ice-shelf buttressing and the stability of marine ice sheets. *The Cryosphere*, 7(2), 647–655.
- [17] Reese, R., Winkelmann, R., & Gudmundsson, G. H. (2018). Grounding-line flux formula applied as a flux condition in numerical simulations fails for buttressed antarctic ice streams. *The Cryosphere*, 12(10), 3229–3242.
- [18] Santoso, A., England, M. H., & Hirst, A. C. (2006). Circumpolar deep water circulation and variability in a coupled climate model. *Journal of Physical Oceanography*, 36(8), 1523 – 1552.
- [19] Orsi, A. H., Whitworth, T., & Nowlin, W. D. (1995). On the meridional extent and fronts of the antarctic circumpolar current. *Deep Sea Research Part I: Oceanographic Research Papers*, 42(5), 641–673.
- [20] Greene, C. A., Gardner, A. S., Schlegel, N.-J., & Fraser, A. D. (2022). Antarctic calving loss rivals ice-shelf thinning. *Nature*, 609(7929), 948–953.
- [21] Scambos, T. A., Hulbe, C., Fahnestock, M., & Bohlander, J. (2000). The link between climate warming and break-up of ice shelves in the antarctic peninsula. *Journal of Glaciology*, 46(154), 516–530.
- [22] Robel, A. A. & Banwell, A. F. (2019). A speed limit on ice shelf collapse through hydrofracture. *Geophysical Research Letters*, 46(21), 12092–12100.
- [23] Pritchard, H. D. & Vaughan, D. G. (2007). Widespread acceleration of tidewater glaciers on the antarctic peninsula. *Journal of Geophysical Research: Earth Surface*, 112(F3).
- [24] Joughin, I. & MacAyeal, D. R. (2005). Calving of large tabular icebergs from ice shelf rift systems. *Geophysical Research Letters*, 32(2).

- [25] Benn, D. I., Warren, C. R., & Mottram, R. H. (2007). Calving processes and the dynamics of calving glaciers. *Earth-Science Reviews*, 82(3-4), 143–179.
- [26] Arndt, J. E., Larter, R. D., Friedl, P., Gohl, K., Høppner, K., et al. (2018). Bathymetric controls on calving processes at pine island glacier. *The Cryosphere*, 12(6), 2039–2050.
- [27] Joughin, I., Shapero, D., Smith, B., Dutrieux, P., & Barham, M. (2021). Ice-shelf retreat drives recent pine island glacier speedup. *Science Advances*, 7(24), eabg3080.
- [28] Ultee, L., Meyer, C., & Minchew, B. (2020). Tensile strength of glacial ice deduced from observations of the 2015 eastern skaftá cauldron collapse, vatnajökull ice cap, iceland. *Journal of Glaciology*, 66(260), 1024–1033.
- [29] Holdsworth, G. & Glynn, J. (1978). Iceberg calving from floating glaciers by a vibrating mechanism. *Nature*, 274, 464–466.
- [30] MacAyeal, D. R., Okal, E. A., Aster, R. C., & Bassis, J. N. (2008). Seismic and hydroacoustic tremor generated by colliding icebergs. *Journal of Geophysical Research: Earth Surface*, 113(F3).
- [31] Cathles, L. M., Okal, E. A., & MacAyeal, D. R. (2009). Seismic observations of sea swell on the floating ross ice shelf, antarctica. *Journal of Geophysical Research: Earth Surface*, 114(F2).
- [32] Brunt, K. M., Okal, E. A., & MacAyeal, D. R. (2011). Antarctic ice-shelf calving triggered by the honshu (japan) earthquake and tsunami, march 2011. *Journal of Glaciology*, 57(205), 785–788.
- [33] Bromirski, P. D., Sergienko, O. V., & MacAyeal, D. R. (2010). Transoceanic infragravity waves impacting antarctic ice shelves. *Geophysical Research Letters*, 37(2).
- [34] Bromirski, P. D. & Stephen, R. A. (2012). Response of the ross ice shelf, antarctica, to ocean gravity-wave forcing. *Annals of Glaciology*, 53(60), 163–172.
- [35] Bromirski, P. D., Diez, A., Gerstoft, P., Stephen, R. A., Bolmer, T., Wiens, D. A., Aster, R. C., & Nyblade, A. (2015). Ross ice shelf vibrations. *Geophysical Research Letters*, 42(18), 7589–7597.
- [36] Banwell, A. (2017). Ice-shelf stability questioned. *Nature*, 544, 306 EP –.
- [37] Massom, R. A., Scambos, T. A., Bennetts, L. G., Reid, P., Squire, V. A., & Stammerjohn, S. E. (2018). Antarctic ice shelf disintegration triggered by sea ice loss and ocean swell. *Nature*, 558(7710), 383–389.
- [38] Bassis, J. N., Coleman, R., Fricker, H. A., & Minster, J. B. (2005). Episodic propagation of a rift on the amery ice shelf, east antarctica. *Geophysical Research Letters*, 32(6).

- [39] Hulbe, C. L., LeDoux, C., & Cruikshank, K. (2010). Propagation of long fractures in the ronne ice shelf, antarctica, investigated using a numerical model of fracture propagation. *Journal of Glaciology*, 56(197), 459–472.
- [40] LeDoux, C. M., Hulbe, C. L., Forbes, M. P., Scambos, T. A., & Alley, K. (2017). Structural provinces of the ross ice shelf, antarctica. *Annals of Glaciology*, 58(75pt1), 88–98.
- [41] Fricker, H. A., Young, N. W., Coleman, R., Bassis, J. N., & Minster, J. B. (2005). Multi-year monitoring of rift propagation on the amery ice shelf, east antarctica. *Geophysical Research Letters*, 32(2).
- [42] Larour, E., Rignot, E., & Aubry, D. (2004). Modelling of rift propagation on ronne ice shelf, antarctica, and sensitivity to climate change. *Geophysical research letters*, 31(16).
- [43] Rignot, E. & MacAyeal, D. R. (1998). Ice-shelf dynamics near the front of the filchner—ronne ice shelf, antarctica, revealed by sar interferometry. *Journal of Glaciology*, 44(147), 405–418.
- [44] MacAyeal, D. R., Rignot, E., & Hulbe, C. L. (1998). Ice-shelf dynamics near the front of the filchner-ronne ice shelf, antarctica, revealed by sar interferometry: model/interferogram comparison. *Journal of Glaciology*, 44(147), 419–428.
- [45] Bassis, J. N., Fricker, H. A., Coleman, R., Bock, Y., Behrens, J., Darnell, D., Okal, M., & Minster, J.-B. (2007). Seismicity and deformation associated with ice-shelf rift propagation. *Journal of Glaciology*, 53(183), 523–536.
- [46] Heeszel, D. S., Fricker, H. A., Bassis, J. N., O’Neel, S., & Walter, F. (2014). Seismicity within a propagating ice shelf rift: The relationship between icequake locations and ice shelf structure. *Journal of Geophysical Research: Earth Surface*, 119(4), 731–744.
- [47] Hulbe, C. L., Klinger, M., Masterson, M., Catania, G., Cruikshank, K., & Bugni, A. (2016). Tidal bending and strand cracks at the kamb ice stream grounding line, west antarctica. *Journal of Glaciology*, 62(235), 816–824.
- [48] Lipovsky, B. P. (2018). Ice shelf rift propagation and the mechanics of wave-induced fracture. *Journal of Geophysical Research: Oceans*, 123(6), 4014–4033.
- [49] Walker, C. C., Bassis, J. N., Fricker, H. A., & Czerwinski, R. J. (2013). Structural and environmental controls on antarctic ice shelf rift propagation inferred from satellite monitoring. *Journal of Geophysical Research: Earth Surface*, 118(4), 2354–2364.
- [50] Lazzara, M. A., Weidner, G. A., Keller, L. M., Thom, J. E., & Cassano, J. J. (2012). Antarctic automatic weather station program: 30 years of polar observation. *Bulletin of the American Meteorological Society*, 93(10), 1519–1537.

- [51] Padman, L., Fricker, H. A., Coleman, R., Howard, S., & Erofeeva, L. (2002). A new tide model for the antarctic ice shelves and seas. *Annals of Glaciology*, 34, 247–254.
- [52] Bromirski, P. D., Chen, Z., Stephen, R. A., Gerstoft, P., Arcas, D., Diez, A., Aster, R. C., Wiens, D. A., & Nyblade, A. (2017). Tsunami and infragravity waves impacting antarctic ice shelves. *Journal of Geophysical Research: Oceans*, 122(7), 5786–5801.
- [53] Toffoli, A. & Bitner-Gregersen, E. M. (2017). *Types of Ocean Surface Waves, Wave Classification*, (pp. 1–8). American Cancer Society.
- [54] Press, F. & Ewing, M. (1951). Propagation of elastic waves in a floating ice sheet. *Eos, Transactions American Geophysical Union*, 32(5), 673–678.
- [55] Aki, K. (1967). Scaling law of seismic spectrum. *Journal of Geophysical Research (1896-1977)*, 72(4), 1217–1231.
- [56] Lough, A. C., Barcheck, C. G., Wiens, D. A., Nyblade, A., & Anandakrishnan, S. (2015). A previously unreported type of seismic source in the firn layer of the east antarctic ice sheet. *Journal of Geophysical Research: Earth Surface*, 120(11), 2237–2252.
- [57] Bassis, J. N., Fricker, H. A., Coleman, R., & Minster, J.-B. (2008). An investigation into the forces that drive ice-shelf rift propagation on the amery ice shelf, east antarctica. *Journal of Glaciology*, 54(184), 17–27.
- [58] McGrath, D., Steffen, K., Holland, P. R., Scambos, T., Rajaram, H., Abdalati, W., & Rignot, E. (2014). The structure and effect of suture zones in the Larsen C Ice Shelf, Antarctica. *Journal of Geophysical Research: Earth Surface*, 119(3), 588–602.
- [59] Kulesa, B., Jansen, D., Luckman, A. J., King, E. C., & Sammonds, P. R. (2014). Marine ice regulates the future stability of a large Antarctic ice shelf. *Nature communications*, 5, 3707.
- [60] Borstad, C., McGrath, D., & Pope, A. (2017). rifting. *Geophysical Research Letters*, 44(9), 4186–4194.
- [61] Barruol, G., Cordier, E., Bascou, J., Fontaine, F. R., Legrésy, B., & Lescarmontier, L. (2013). Tide-induced microseismicity in the mertz glacier grounding area, east antarctica. *Geophysical Research Letters*, 40(20), 5412–5416.
- [62] Podolskiy, E. A., Sugiyama, S., Funk, M., Walter, F., Genco, R., Tsutaki, S., Minowa, M., & Ripepe, M. (2016). Tide-modulated ice flow variations drive seismicity near the calving front of bowdoin glacier, greenland. *Geophysical Research Letters*, 43(5), 2036–2044.
- [63] Brunt, K., King, M., Fricker, H., & Macayeal, D. (2010). Flow of the ross ice shelf, antarctica, is modulated by the ocean tide. *Journal of Glaciology*, 56, 157–161.

- [64] Makinson, K., King, M. A., Nicholls, K. W., & Gudmundsson, G. H. (2012). Diurnal and semidiurnal tide-induced lateral movement of ronne ice shelf, antarctica. *Geophysical Research Letters*, 39(10).
- [65] Petrovic, J. (2003). Review mechanical properties of ice and snow. *Journal of Materials Science*, 38, 1–6.
- [66] Evans, R. J. & Untersteiner, N. (1971). Thermal cracks in floating ice sheets. *Journal of Geophysical Research (1896-1977)*, 76(3), 694–703.
- [67] Richter-Menge, J. A. & Elder, B. C. (1998). Characteristics of pack ice stress in the alaskan beaufort sea. *Journal of Geophysical Research: Oceans*, 103(C10), 21817–21829.
- [68] Dempsey, J. P., Cole, D. M., & Wang, S. (2018). Tensile fracture of a single crack in first-year sea ice. *Phil. Trans. R. Soc. A*, 376(2129), 20170346. Exported from <https://app.dimensions.ai> on 2019/03/14.
- [69] Podolskiy, E. A., Fujita, K., Sunako, S., Tsushima, A., & Kayastha, R. B. (2018). Nocturnal thermal fracturing of a himalayan debris-covered glacier revealed by ambient seismic noise. *Geophysical Research Letters*, 45(18), 9699–9709.
- [70] Zhang, T., Chen, Y., Ding, M., Shen, Z., Yang, Y., & Guan, Q. (2019). Air-temperature control on diurnal variations in microseismicity at laohugou glacier no. 12, qilian mountains. *Annals of Glaciology*, (pp. 1–12).
- [71] Giese, A. L. & Hawley, R. L. (2015). Reconstructing thermal properties of firn at summit, greenland, from a temperature profile time series. *Journal of Glaciology*, 61(227), 503–510.
- [72] Seroussi, H., Nowicki, S., Payne, A. J., Goelzer, H., Lipscomb, W. H., Abe-Ouchi, A., Agosta, C., Albrecht, T., Asay-Davis, X., Barthel, A., et al. (2020). Ismip6 antarctica: a multi-model ensemble of the antarctic ice sheet evolution over the 21st century. *The Cryosphere*, 14(9), 3033–3070.
- [73] Scambos, T. A., Bell, R. E., Alley, R. B., Anandakrishnan, S., Bromwich, D., Brunt, K., Christianson, K., Creyts, T., Das, S., DeConto, R., et al. (2017). How much, how fast?: A science review and outlook for research on the instability of antarctica’s thwaites glacier in the 21st century. *Global and Planetary Change*, 153, 16–34.
- [74] Lipovsky, B. P. (2020). Ice shelf rift propagation: stability, three-dimensional effects, and the role of marginal weakening. *The Cryosphere*, 14(5), 1673–1683.
- [75] Rist, M., Sammonds, P., Oerter, H., & Doake, C. (2002). Fracture of antarctic shelf ice. *Journal of Geophysical Research: Solid Earth*, 107(B1), ECV–2.

- [76] McGrath, D., Steffen, K., Scambos, T., Rajaram, H., Casassa, G., & Lajos, J. L. R. (2012). Basal crevasses and associated surface crevassing on the larsen c ice shelf, antarctica, and their role in ice-shelf instability. *Annals of glaciology*, 53(60), 10–18.
- [77] Weertman, J. (1973). Can a water-filled crevasse reach the bottom surface of a glacier. *IASH publ*, 95, 139–145.
- [78] Banwell, A. F., MacAyeal, D. R., & Sergienko, O. V. (2013). Breakup of the larsen b ice shelf triggered by chain reaction drainage of supraglacial lakes. *Geophysical Research Letters*, 40(22), 5872–5876.
- [79] Clerc, F., Minchew, B. M., & Behn, M. D. (2019). Marine ice cliff instability mitigated by slow removal of ice shelves. *Geophysical Research Letters*, 46(21), 12108–12116.
- [80] Von der Osten-Woldenburg, H. (1990). Icequakes on ekstrøm ice shelf near atka bay, antarctica. *Journal of Glaciology*, 36(122), 31–36.
- [81] Hammer, C., Ohrnberger, M., & Schlindwein, V. (2015). Pattern of cryospheric seismic events observed at ekstrøm ice shelf, antarctica. *Geophysical Research Letters*, 42(10), 3936–3943.
- [82] Chen, Z., Bromirski, P., Gerstoft, P., Stephen, R., Lee, W. S., Yun, S., Olinger, S., Aster, R., Wiens, D., & Nyblade, A. (2019). Ross ice shelf icequakes associated with ocean gravity wave activity. *Geophysical Research Letters*, 46(15), 8893–8902.
- [83] Winberry, J. P., Huerta, A. D., Anandakrishnan, S., Aster, R. C., Nyblade, A. A., & Wiens, D. A. (2020). Glacial earthquakes and precursory seismicity associated with thwaites glacier calving. *Geophysical Research Letters*, 47(3), e2019GL086178. e2019GL086178 2019GL086178.
- [84] Olinger, S. D., Lipovsky, B. P., Wiens, D. A., Aster, R. C., Bromirski, P. D., Chen, Z., Gerstoft, P., Nyblade, A. A., & Stephen, R. A. (2019). Tidal and thermal stresses drive seismicity along a major ross ice shelf rift. *Geophysical Research Letters*, 46(12), 6644–6652.
- [85] Aster, R. C., Lipovsky, B. P., Cole, H. M., Bromirski, P. D., Gerstoft, P., Nyblade, A., Wiens, D. A., & Stephen, R. (2021). Swell-Triggered Seismicity at the Near-Front Damage Zone of the Ross Ice Shelf. *Seismological Research Letters*, 92(5), 2768–2792.
- [86] Shepherd, A., Ivins, E., Rignot, E., Smith, B., Van Den Broeke, M., Velicogna, I., Whitehouse, P., Briggs, K., Joughin, I., Krinner, G., et al. (2018). Mass balance of the antarctic ice sheet from 1992 to 2017. *Nature*, 558, 219–222.
- [87] Christianson, K., Bushuk, M., Dutrieux, P., Parizek, B. R., Joughin, I. R., Alley, R. B., Shean, D. E., Abrahamsen, E. P., Anandakrishnan, S., Heywood, K. J., Kim, T.-W., Lee,

- S. H., Nicholls, K., Stanton, T., Truffer, M., Webber, B. G. M., Jenkins, A., Jacobs, S., Bindschadler, R., & Holland, D. M. (2016). Sensitivity of pine island glacier to observed ocean forcing. *Geophysical Research Letters*, 43(20), 10,817–10,825.
- [88] Joughin, I., Shapero, D., Dutrieux, P., & Smith, B. (2021). Ocean-induced melt volume directly paces ice loss from pine island glacier. *Science advances*, 7(43), eabi5738.
- [89] MacGregor, J. A., Catania, G. A., Markowski, M. S., & Andrews, A. G. (2012). Widespread rifting and retreat of ice-shelf margins in the eastern amundsen sea embayment between 1972 and 2011. *Journal of Glaciology*, 58(209), 458–466.
- [90] Ewing, M. & Crary, A. (1934). Propagation of elastic waves in ice. part ii. *Physics*, 5(7), 181–184.
- [91] Sergienko, O. (2017). Behavior of flexural gravity waves on ice shelves: Application to the ross ice shelf. *Journal of Geophysical Research: Oceans*, 122(8), 6147–6164.
- [92] Mattsson, K., Dunham, E. M., & Werpers, J. (2018). Simulation of acoustic and flexural-gravity waves in ice-covered oceans. *Journal of Computational Physics*, 373, 230–252.
- [93] Zhan, Z., Tsai, V. C., Jackson, J. M., & Helmberger, D. (2014). Ambient noise correlation on the amery ice shelf, east antarctica. *Geophysical Journal International*, 196(3), 1796–1802.
- [94] Williams, R. & Robinson, E. (1981). Flexural waves in the ross ice shelf. *Journal of Geophysical Research: Oceans*, 86(C7), 6643–6648.
- [95] MacAyeal, D. R., Okal, E. A., Aster, R. C., & Bassis, J. N. (2009). Seismic observations of glaciogenic ocean waves (micro-tsunamis) on icebergs and ice shelves. *Journal of Glaciology*, 55(190), 193–206.
- [96] Pitz, W. & Miller, D. (2010). The terrasars-x satellite. *IEEE Transactions on Geoscience and Remote Sensing*, 48(2), 615–622.
- [97] Renshaw, C. E. & Schulson, E. M. (2001). Universal behaviour in compressive failure of brittle materials. *Nature*, 412(6850), 897–900.
- [98] Stanton, T. P., Shaw, W., Truffer, M., Corr, H., Peters, L., Riverman, K., Bindschadler, R., Holland, D., & Anandakrishnan, S. (2013). Channelized ice melting in the ocean boundary layer beneath pine island glacier, antarctica. *Science*, 341(6151), 1236–1239.
- [99] David Holland & Robert Bindschadler (2012). Observing pine island glacier (pig) ice shelf deformation and fracture using a gps and seismic network.
- [100] Allen, R. V. (1978). Automatic earthquake recognition and timing from single traces. *Bulletin of the Seismological Society of America*, 68(5), 1521–1532.

- [101] Gibbons, S. J. & Ringdal, F. (2006). The detection of low magnitude seismic events using array-based waveform correlation. *Geophysical Journal International*, 165(1), 149–166.
- [102] Paparrizos, J. & Gravano, L. (2016). K-shape: Efficient and accurate clustering of time series. *SIGMOD Rec.*, 45(1), 69–76.
- [103] Bindschadler, R., Choi, H., Wichlacz, A., Bingham, R., Bohlander, J., Brunt, K., Corr, H., Drews, R., Fricker, H., Hall, M., Hindmarsh, R., Kohler, J., Padman, L., Rack, W., Rotschky, G., Urbini, S., Vornberger, P., & Young, N. (2011). Getting around antarctica: new high-resolution mappings of the grounded and freely-floating boundaries of the antarctic ice sheet created for the international polar year. *The Cryosphere*, 5(3), 569–588.
- [104] Walker, C. & Gardner, A. (2019). Evolution of ice shelf rifts: Implications for formation mechanics and morphological controls. *Earth and Planetary Science Letters*, 526, 115764.
- [105] Jeong, S., Howat, I. M., & Bassis, J. N. (2016). Accelerated ice shelf rifting and retreat at pine island glacier, west antarctica. *Geophysical Research Letters*, 43(22), 11,720–11,725.
- [106] Squire, V. A. & Allan, A. (1977). *Propagation of flexural gravity waves in sea ice*. Centre for Cold Ocean Resources Engineering, Memorial University of Newfoundland.
- [107] Shean, D. E., Joughin, I. R., Dutrieux, P., Smith, B. E., & Berthier, E. (2019). Ice shelf basal melt rates from a high-resolution digital elevation model (dem) record for pine island glacier, antarctica. *The Cryosphere*, 13(10), 2633–2656.
- [108] Fretwell, P., Pritchard, H. D., Vaughan, D. G., Bamber, J. L., Barrand, N. E., Bell, R., Bianchi, C., Bingham, R. G., Blankenship, D. D., Casassa, G., Catania, G., Callens, D., Conway, H., Cook, A. J., Corr, H. F. J., Damaske, D., Damm, V., Ferraccioli, F., Forsberg, R., Fujita, S., Gim, Y., Gogineni, P., Griggs, J. A., Hindmarsh, R. C. A., Holmlund, P., Holt, J. W., Jacobel, R. W., Jenkins, A., Jokat, W., Jordan, T., King, E. C., Kohler, J., Krabill, W., Riger-Kusk, M., Langley, K. A., Leitchenkov, G., Leuschen, C., Luyendyk, B. P., Matsuoka, K., Mouginot, J., Nitsche, F. O., Nogi, Y., Nost, O. A., Popov, S. V., Rignot, E., Ripplin, D. M., Rivera, A., Roberts, J., Ross, N., Siegert, M. J., Smith, A. M., Steinhage, D., Studinger, M., Sun, B., Tinto, B. K., Welch, B. C., Wilson, D., Young, D. A., Xiangbin, C., & Zirizzotti, A. (2013). Bedmap2: improved ice bed, surface and thickness datasets for antarctica. *The Cryosphere*, 7(1), 375–393.
- [109] Aki, K. & Richards, P. G. (2002). *Quantitative seismology*. University science books.
- [110] Ekström, G., Nettles, M., & Abers, G. A. (2003). Glacial earthquakes. *Science*, 302(5645), 622–624.
- [111] Freund, L. B. (1998). *Dynamic fracture mechanics*. Cambridge university press.

- [112] Lipovsky, B. P. & Dunham, E. M. (2015). Vibrational modes of hydraulic fractures: Inference of fracture geometry from resonant frequencies and attenuation. *Journal of Geophysical Research: Solid Earth*, 120(2), 1080–1107.
- [113] Fürst, J. J., Durand, G., Gillet-Chaulet, F., Tavard, L., Rankl, M., Braun, M., & Gagliardini, O. (2016). The safety band of antarctic ice shelves. *Nature Climate Change*, 6(5), 479–482.
- [114] Reese, R., Gudmundsson, G. H., Levermann, A., & Winkelmann, R. (2018). The far reach of ice-shelf thinning in antarctica. *Nature Climate Change*, 8(1), 53–57.
- [115] Lai, C.-Y., Kingslake, J., Wearing, M. G., Chen, P.-H. C., Gentine, P., Li, H., Spergel, J. J., & van Wessem, J. M. (2020). Vulnerability of antarctica’s ice shelves to meltwater-driven fracture. *Nature*, 584(7822), 574–578.
- [116] Borstad, C., Khazendar, A., Larour, E., Morlighem, M., Rignot, E., Schodlok, M., & Seroussi, H. (2012). A damage mechanics assessment of the larsen b ice shelf prior to collapse: Toward a physically-based calving law. *Geophysical Research Letters*, 39(18).
- [117] Lhermitte, S., Sun, S., Shuman, C., Wouters, B., Pattyn, F., Wuite, J., Berthier, E., & Nagler, T. (2020). Damage accelerates ice shelf instability and mass loss in amundsen sea embayment. *Proceedings of the National Academy of Sciences*, 117(40), 24735–24741.
- [118] Bassis, J., Berg, B., Crawford, A., & Benn, D. (2021). Transition to marine ice cliff instability controlled by ice thickness gradients and velocity. *Science*, 372(6548), 1342–1344.
- [119] DeConto, R. M. & Pollard, D. (2016). Contribution of antarctica to past and future sea-level rise. *Nature*, 531(7596), 591–597.
- [120] Pattyn, F., Ritz, C., Hanna, E., Asay-Davis, X., DeConto, R., Durand, G., Favier, L., Fettweis, X., Goelzer, H., Golledge, N. R., et al. (2018). The greenland and antarctic ice sheets under 1.5 c global warming. *Nature climate change*, 8(12), 1053–1061.
- [121] Dow, C. F., Lee, W. S., Greenbaum, J. S., Greene, C. A., Blankenship, D. D., Poinar, K., Forrest, A. L., Young, D. A., & Zappa, C. J. (2018). Basal channels drive active surface hydrology and transverse ice shelf fracture. *Science Advances*, 4(6), ea07212.
- [122] Alley, K. E., Scambos, T. A., Alley, R. B., & Holschuh, N. (2019). Troughs developed in ice-stream shear margins precondition ice shelves for ocean-driven breakup. *Science Advances*, 5(10), eaax2215.
- [123] Squire, V. A. (2007). Of ocean waves and sea-ice revisited. *Cold Regions Science and Technology*, 49(2), 110–133.
- [124] Abrahams, L. S., Mierzejewski, J. E., & Dunham, E. M. (2022). Ocean surface gravity wave excitation of flexural gravity and extensional lamb waves in ice shelves. *EarthArXiv*. Preprint at <https://eartharxiv.org/repository/view/3548/>.

- [125] Olinger, S. D., Lipovsky, B. P., Denolle, M. A., & Crowell, B. W. (2022). Tracking the cracking: A holistic analysis of rapid ice shelf fracture using seismology, geodesy, and satellite imagery on the pine island glacier ice shelf, west antarctica. *Geophysical Research Letters*, 49(10), e2021GL097604.
- [126] Chen, Z., Bromirski, P. D., Gerstoft, P., Stephen, R. A., Wiens, D. A., Aster, R. C., & Nyblade, A. A. (2018). Ocean-excited plate waves in the ross and pine island glacier ice shelves. *Journal of Glaciology*, 64(247), 730–744.
- [127] Freund, L. B. (1990). *Dynamic Fracture Mechanics*. Cambridge Monographs on Mechanics. Cambridge University Press.
- [128] Kim, K., Lee, J., Hong, M., Hong, J., Jin, Y., & Shon, H. (2010). Seismic and radar investigations of fourcade glacier on king george island, antarctica. *Polar Research*, 29, 298 – 310.
- [129] Segall, P. (2010). *Earthquake and Volcano Deformation*. Princeton University Press.
- [130] Muto, A., Peters, L. E., Gohl, K., Sasgen, I., Alley, R. B., Anandakrishnan, S., & Riverman, K. L. (2016). Subglacial bathymetry and sediment distribution beneath pine island glacier ice shelf modeled using aerogravity and in situ geophysical data: New results. *Earth and Planetary Science Letters*, 433, 63–75.
- [131] Jacobs, S. S., Jenkins, A., Giulivi, C. F., & Dutrieux, P. (2011). Stronger ocean circulation and increased melting under pine island glacier ice shelf. *Nature Geoscience*, 4(8), 519–523.
- [132] Holland, P. R., Bracegirdle, T. J., Dutrieux, P., Jenkins, A., & Steig, E. J. (2019). West antarctic ice loss influenced by internal climate variability and anthropogenic forcing. *Nature Geoscience*, 12(9), 718–724.
- [133] Dunham, E. M. (2007). Conditions governing the occurrence of supershear ruptures under slip-weakening friction. *Journal of Geophysical Research: Solid Earth*, 112(B7).
- [134] King, M. D., Howat, I. M., Candela, S. G., Noh, M. J., Jeong, S., Noël, B. P. Y., van den Broeke, M. R., Wouters, B., & Negrete, A. (2020). Dynamic ice loss from the Greenland Ice Sheet driven by sustained glacier retreat. *Communications Earth & Environment*, 1(1), 1.
- [135] Slater, T., Shepherd, A., McMillan, M., Leeson, A., Gilbert, L., Muir, A., Munneke, P. K., Noël, B., Fettweis, X., van den Broeke, M., & Briggs, K. (2021). Increased variability in Greenland Ice Sheet runoff from satellite observations. *Nature Communications*, 12(1), 6069.
- [136] Weertman, J. & Birchfield, G. E. (1983). Basal water film, basal water pressure, and velocity of traveling waves on glaciers. *Journal of Glaciology*, 29(101), 20–27.

- [137] Law, R., Christoffersen, P., Hubbard, B., Doyle, S. H., Chudley, T. R., Schoonman, C. M., Bougamont, M., des Tombe, B., Schilperoort, B., Kechavarzi, C., Booth, A., & Young, T. J. (2021). Thermodynamics of a fast-moving greenlandic outlet glacier revealed by fiber-optic distributed temperature sensing. *Science Advances*, 7(20), eabe7136.
- [138] Doyle, S. H., Hubbard, B., Christoffersen, P., Law, R., Hewitt, D. R., Neufeld, J. A., Schoonman, C. M., Chudley, T. R., & Bougamont, M. (2022). Water flow through sediments and at the ice-sediment interface beneath sermeq kujalleq (store glacier), greenland. *Journal of Glaciology*, 68(270), 665–684.
- [139] Booth, A. D., Christoffersen, P., Schoonman, C., Clarke, A., Hubbard, B., Law, R., Doyle, S. H., Chudley, T. R., & Chalari, A. (2020). Distributed Acoustic Sensing of Seismic Properties in a Borehole Drilled on a Fast-Flowing Greenlandic Outlet Glacier. *Geophysical Research Letters*, 47(13), e2020GL088148. _eprint: <https://agupubs.onlinelibrary.wiley.com/doi/pdf/10.1029/2020GL088148>.
- [140] Brisbourne, A. M., Kendall, M., Kufner, S.-K., Hudson, T. S., & Smith, A. M. (2021). Downhole distributed acoustic seismic profiling at skytrain ice rise, west antarctica. *The Cryosphere*, 15(7), 3443–3458.
- [141] Zhou, W., Butcher, A., Brisbourne, A. M., Kufner, S.-K., Kendall, J.-M., & Stork, A. L. (2022). Seismic noise interferometry and distributed acoustic sensing (das): Inverting for the firn layer s-velocity structure on rutford ice stream, antarctica. *Journal of Geophysical Research: Earth Surface*, 127(12), e2022JF006917. e2022JF006917 2022JF006917.
- [142] Hudson, T. S., Baird, A. F., Kendall, J. M., Kufner, S. K., Brisbourne, A. M., Smith, A. M., Butcher, A., Chalari, A., & Clarke, A. (2021). Distributed acoustic sensing (das) for natural microseismicity studies: A case study from antarctica. *Journal of Geophysical Research: Solid Earth*, 126(7), e2020JB021493. e2020JB021493 2020JB021493.
- [143] Walter, F., Gräff, D., Lindner, F., Paitz, P., Köpfl, M., Chmiel, M., & Fichtner, A. (2020). Distributed acoustic sensing of microseismic sources and wave propagation in glaciated terrain. *Nature Communications*, 11(1), 2436.
- [144] Klaasen, S., Paitz, P., Lindner, N., Dettmer, J., & Fichtner, A. (2021). Distributed acoustic sensing in volcano-glacial environments—mount meager, british columbia. *Journal of Geophysical Research: Solid Earth*, 126(11), e2021JB022358. e2021JB022358 2021JB022358.
- [145] Hubbard, B., Christoffersen, P., Doyle, S. H., Chudley, T. R., Schoonman, C. M., Law, R., & Bougamont, M. (2021). Borehole-based characterization of deep mixed-mode crevasses at a greenlandic outlet glacier. *AGU Advances*, 2(2), e2020AV000291. e2020AV000291 2020AV000291.

- [146] Chudley, T. R., Christoffersen, P., Doyle, S. H., Bougamont, M., Schoonman, C. M., Hubbard, B., & James, M. R. (2019). Supraglacial lake drainage at a fast-flowing greenlandic outlet glacier. *Proceedings of the National Academy of Sciences*, 116(51), 25468–25477.
- [147] Hock, R. & Hooke, R. (1993). Evolution of the internal drainage system in the lower part of the ablation area of storglaci?ären, sweden. *Geological Society of America Bulletin - GEOL SOC AMER BULL*, 105, 537–546.
- [148] Fountain, A. G. (1993). Geometry and flow conditions of subglacial water at south cascade glacier, washington state, u.s.a.; an analysis of tracer injections. *Journal of Glaciology*, 39(131), 143–156.
- [149] Fountain, A. G. & Walder, J. S. (1998). Water flow through temperate glaciers. *Reviews of Geophysics*, 36(3), 299–328.
- [150] Barcheck, C. G., Tulaczyk, S., Schwartz, S. Y., Walter, J. I., & Winberry, J. P. (2018). Implications of basal micro-earthquakes and tremor for ice stream mechanics: Stick-slip basal sliding and till erosion. *Earth and Planetary Science Letters*, 486, 54–60.
- [151] Lipovsky, B. P. & Dunham, E. M. (2016). Tremor during ice-stream stick slip. *The Cryosphere*, 10(1), 385–399.
- [152] Zeng, X., Thurber, C. H., Wang, H. F., Fratta, D., & Feigl, K. L. (2021). *High-Resolution Shallow Structure at Brady Hot Springs Using Ambient Noise Tomography (ANT) on a Trenched Distributed Acoustic Sensing (DAS) Array*, chapter 8, (pp. 101–110). American Geophysical Union (AGU).
- [153] Bensen, G. D., Ritzwoller, M. H., Barmin, M. P., Levshin, A. L., Lin, F., Moschetti, M. P., Shapiro, N. M., & Yang, Y. (2007). Processing seismic ambient noise data to obtain reliable broad-band surface wave dispersion measurements. *Geophysical Journal International*, 169(3), 1239–1260.
- [154] Ermert, L., Villaseñor, A., & Fichtner, A. (2015). Cross-correlation imaging of ambient noise sources. *Geophysical Journal International*, 204(1), 347–364. _eprint: <https://academic.oup.com/gji/article-pdf/204/1/347/17369342/ggv460.pdf>.
- [155] Clements, T. & Denolle, M. A. (2020). SeisNoise.jl: Ambient Seismic Noise Cross Correlation on the CPU and GPU in Julia. *Seismological Research Letters*, 92(1), 517–527. _eprint: <https://pubs.geoscienceworld.org/ssa/srl/article-pdf/92/1/517/5209943/srl-2020192.1.pdf>.
- [156] Jones, J. P., Okubo, K., Clements, T., & Denolle, M. A. (2020). SeisIO: A Fast, Efficient Geophysical Data Architecture for the Julia Language. *Seismological Research Letters*, 91(4), 2368–2377. _eprint: <https://pubs.geoscienceworld.org/ssa/srl/article-pdf/91/4/2368/5082313/srl-2019295.1.pdf>.

- [157] Flores-Mendez, E., Carbajal-Romero, M., Flores-Guzmán, N., Sánchez-Martínez, R., & Rodríguez-Castellanos, A. (2012). Rayleigh's, Stoneley's, and Scholte's Interface Waves in Elastic Models Using a Boundary Element Method. *Journal of Applied Mathematics*, 2012, 313207. Publisher: Hindawi Publishing Corporation.
- [158] Karlsson, N. B., Dahl-Jensen, D., Prasad Gogineni, S., & Paden, J. D. (2013). Tracing the depth of the holocene ice in north greenland from radio-echo sounding data. *Annals of Glaciology*, 54(64), 44–50.
- [159] Horgan, H. J., Anandakrishnan, S., Alley, R. B., Peters, L. E., Tsoflias, G. P., Voigt, D. E., & Winberry, J. P. (2008). Complex fabric development revealed by englacial seismic reflectivity: Jakobshavn isbræ, greenland. *Geophysical Research Letters*, 35(10).



THIS THESIS WAS TYPESET using \LaTeX , originally developed by Leslie Lamport and based on Donald Knuth's \TeX . The body text is set in 11 point Egenolff-Berner Garamond, a revival of Claude Garamont's humanist typeface. The above illustration, "Science Experiment 02", was created by Ben Schlitter and released under [CC BY-NC-ND 3.0](#). A template that can be used to format a PhD thesis with this look and feel has been released under the permissive MIT (X11) license, and can be found online at github.com/suchow/Dissertate or from its author, Jordan Suchow, at suchow@post.harvard.edu.